E.ON Energy Research Center

RWTH AACHEN UNIVERSITY

Data-Driven Distribution System State Estimation Using Synchrophasor Measurements

Behzad Zargar
Institute for Automation of Complex Power Systems

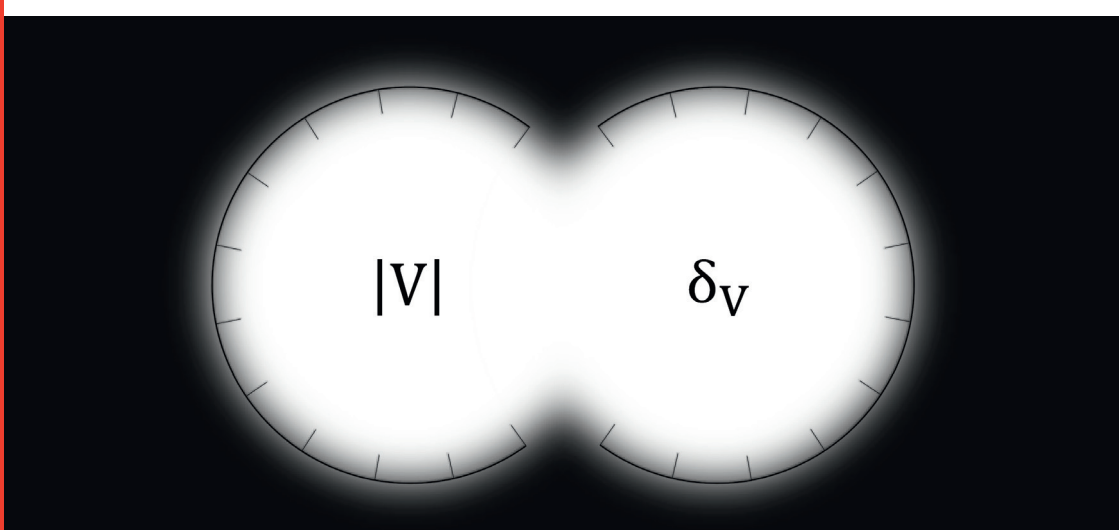

Data-Driven Distribution System State Estimation Using Synchrophasor Measurements

Von der Fakultät für Elektrotechnik und Informationstechnik der Rheinisch-Westfälischen Technischen Hochschule Aachen zur Erlangung des akademischen Grades eines Doktors der Ingenieurwissenschaften genehmigte Dissertation

vorgelegt von

Behzad Zargar, M. Sc.

aus Esfahan, Iran

Berichter:

Univ.-Prof. Ferdinanda Ponci, Ph. D.

Univ.-Prof. Dr. sc. Andreas Ulbig

Tag der mündlichen Prüfung : 22.11.2023

Bibliographische Information der Deutschen Nationalbibliothek
Die Deutsche Nationalbibliothek verzeichnet diese Publikation in der Deutschen Nationalbibliografie; detaillierte bibliografische Daten sind im Internet über http://dnb-nb.de abrufbar.

D 82 (Diss. RWTH Aachen University, 2023)

Herausgeber:
Univ.-Prof. Dr. ir. Dr. h. c. Rik W. De Doncker
Direktor E.ON Energy Research Center

Institute for Automation of Complex Power Systems (ACS)
E.ON Energy Research Center
Mathieustraße 10
52074 Aachen

E.ON Energy Research Center I 123. Ausgabe der Serie
ACS I Automation of Complex Power Systems

Printed in Germany

ISBN: 978-3-948234-37-9
1. Auflage 2023

Verlag:
E.ON Energy Research Center, RWTH Aachen University
Mathieustraße 10
52074 Aachen
Internet: www.eonerc.rwth-aachen.de
E-Mail: post_erc@eonerc.rwth-aachen.de

Herstellung:
Druckservice Zillekens
Rainweg 19
52224 Stolberg
Mail: info@druckservice-zillekens.de

Abstract

Motivation, Goal and Task of the Dissertation

To achieve greater independence from fossil fuels and address the challenges of climate change, environmentally friendly energy sources (e.g., wind, solar photovoltaic, electric vehicles, etc.) are rapidly integrating into power systems. The primary focus of this energy transition occurs within distribution grids, where end consumers and distributed energy resources connect to the grid. To efficiently operate distribution systems in a safe mode and establish synergy among active elements, distribution system operators (DSOs) should employ strategies based on ongoing operating conditions. The operating condition of the power system, in terms of its current state, must be determined timely and accurately. To this end, this dissertation introduces a distribution system state estimation (DSSE) approach based on the data-driven artificial neural network (ANN) modeling technique and synchrophasor measurements to provide a snapshot of the grid state. Compared to state-of-the-art model-based state estimation methods, mostly relying on the weighted least squares (WLS) approach, the proposed ANN-based estimator does not involve Jacobian matrix and gain matrix inverse calculations in runtime. Therefore, the proposed ANN estimator is simpler and performs faster than model-based methods. Thus, it can be considered a potential DSSE method that meets the real-time requirements of automation functions in distribution grids.

Major Scientific Contributions

In this dissertation, the voltage magnitude and the phase angle of the grid buses represent the system states. Based on this, the major contributions of the dissertation are summarized here:

1) The ANN, as one of the powerful non-linear regression methods, has been used to map the synchrophasor measurements to the system states. The applied Pearson correlation coefficient shows that there is a correlation with nonlinear dependency between

synchrophasor measurements and the system states. According to the universal approximation theorem, a feedforward multilayer perceptron network with a linear output layer and one hidden layer with a hyperbolic tangent (tanh) activation function can fulfill the requirement of this mapping. Each layer requires several nodes. The number of nodes in the input and output layers is equal to the number of synchrophasor measurements and the number of states, respectively. To improve the generalization capability of the ANN, only two neurons are considered in the hidden layer. Moreover, the Bayesian regularization learning algorithm is used for training the ANN in this work to make the estimator more robust against overfitting concern.

2) The proposed estimator estimates the system states in the polar coordinate. To obtain accurate estimation results without bias, this estimator consists of two ANNs. One estimates the voltage magnitude, and another calculates the phase angle. In addition to the synchrophasor measurements, other measurements such as power measurements can be added to the measurement inputs.

3) To consider the unbalanced nature of distribution grids, three independent ANN-based estimators, corresponding to the three phases of the network, are trained in parallel with the training data generated by a three-phase power flow (PF) solver.

4) To understand how fast the proposed ANN-based estimator is executed, the computational complexity of this technique has been compared with the model-based state estimation methods in terms of elapsed time and the floating-point operation (FLOP) number. Compared to elapsed time, FLOP is a machine-independent measure. And, as shown in this dissertation, FLOP is a more reliable indicator than elapsed time for assessing the computational effort of the DSSE problems in real-time applications.

5) To alleviate the computational burden during the training and estimation phase of the ANN-based estimators, the estimation problem has been distributed over several smaller problems in a parallel and in a multi-area architecture. In the parallel architecture, the training dataset is divided into smaller training data packages, those containing the output training data associated with smaller portions of the power grid. Compared to the integrated system, then, the smaller ANN-based estimators are trained with the smaller data packages corresponding to the smaller grid subsections. Since the training method maps all the measurements to a smaller number of states for each sub-area, it can better tune the weights and biases of the ANNs. Consequently, more accurate estimations are obtained by performing the state estimation in the parallel architecture compared to performing the state estimation on the integrated system. In the multi-area architecture, the power grid is divided into smaller sub-areas. The system is split at the points where phasor measurement units (PMUs) are installed. Since PMUs

measure both voltage magnitude and phase angle, the splitting points can be considered as the virtual slack buses. In this way, a big power flow (PF) problem is divided into smaller PF problems for the divided sub-areas. By performing the PF over a wide range of operating conditions, the training data is generated for each sub-area. Then, the ANN-based estimator is trained for each sub-area. Finally, the state estimation is performed in two steps. In the first step, upon receiving the measurements, the ANN for each sub-area calculates the local estimations. The splitting point is an overlapping node among the neighboring sub-areas. Therefore, there are multiple estimated states for the splitting point calculated by the neighboring ANN-based estimators. To choose the states of the overlapping nodes, then, the estimations from the most accurate local estimator are selected. In the second step, the measurements of the overlapping nodes are replaced with the selected states of the overlapping nodes. By doing so, the accuracy of the estimations is improved since the accuracy of the estimated states of the overlapping nodes is better than the measured values at these points.

6) Finally, an iterative linear PF method has been introduced to generate the data required to train the proposed ANN state estimator. In this PF method, the linear current injection model of P-Q and P-V nodes is integrated into the fixed-point-iteration algorithm. In the case that there are only P-Q nodes in the grid, the PF is solved in a single shot. However, some iterations are required when there are P-V nodes in the system. The model of the P-V node is relaxed by a relaxation factor. Utilizing the optimal relaxation factor enhances the convergence rate of the PF problem.

In a nutshell, a fast data-driven monitoring approach for active distribution system has been introduced in this dissertation. The training data is firstly generated by the power flow calculations. Then, per phase, two ANNs are trained to map the corresponding measurement inputs to the system states in the offline mode. And, at the final step, the ANNs give the system states upon receiving the synchrophasor measurements in the run-time.

List of Publications

The main parts of this dissertation are previously published in three journal publications, in all of which I am the first author:

- **Behzad Zargar**, Ferdinanda Ponci, Antonello Monti. "Evaluation of Computational Complexity for Distribution Systems State Estimation". In: IEEE Transactions on Instrumentation and Measurement 72 (2023).
- **Behzad Zargar**, Antonello Monti, Ferdinanda Ponci, José R. Martí. "Linear Iterative Power Flow Approach Based on the Current Injection Model of Load and Generator". In: IEEE Access 9 (2020), pp. 11543–11562.
- **Behzad Zargar**, Andrea Angioni, Ferdinanda Ponci, Antonello Monti. "Multi-area Parallel Data-Driven Three-Phase Distribution System State Estimation Using Synchrophasor Measurements". In: IEEE Transactions on Instrumentation and Measurement 69.9 (2020), pp. 6186–6202.

In addition to these publications, I contributed in the other restated journal and conference papers:

- **Behzad Zargar**, Ting Wang, Manuel Pitz, Rainer Bachmann, Moritz Maschmann, Angelina Bintoudi, Lampros Zyglakis, Ferdinanda Ponci, Antonello Monti, and Dimosthenis Ioannidis. "Power Quality Improvement in Distribution Grids via Real-Time Smart Exploitation of Electric Vehicles". In: Energies 14.12 (2021), p. 3533.
- Mohsen Ferdowsi, Andrea Benigni, Artur Löwen, **Behzad Zargar**, Antonello Monti, Ferdinanda Ponci. "A scalable data-driven monitoring approach for distribution systems". In: IEEE Transactions on Instrumentation and Measurement 64.5 (2015), pp. 1292–1305.
- Mohsen Ferdowsi, **Behzad Zargar**, Ferdinanda Ponci, Antonello Monti. "Design considerations for artificial neural networkbased estimators in monitoring of distribution systems". In: 2014 IEEE International Workshop on Applied Measurements for Power Systems Proceedings (AMPS). IEEE. 2014, pp. 1–6.

Contents

Chapter 1

Introduction

The energy transformation from the consumption of fossil fuels to cleaner, renewable forms of energy is a promising solution to combat climate change in this century. The main aim of this transformation is to limit global warming to the relatively safe 1.5°C compared to pre-industrial times, according to the Intergovernmental Panel on Climate Change [1]. To this end, the policy and regulatory frameworks need to be adjusted so that the world's share of renewable energy in the final energy supply would increase to 28% by 2030 and 66% by 2050 [2]. Energy efficiency and renewable energy technologies are the core elements of this transition. The main part of this transition takes place in distribution systems where end-consumers and distributed renewable energy resources are connected to the grid side [3]. In this paradigm, the distribution systems change into active distribution grids due to the rapid penetration of modern distributed energy resources (DERs), especially wind, solar photovoltaic (PV), and increasing prosumers like district heating systems and electromobility services. The intermittent behavior of active elements (in both consumption and generation sides), on the one hand, makes fast variations in the power system states. Consequently, the system might face abnormal grid conditions like voltage drop, voltage rise, and overloading of the asset's capacity. On the other hand, the controllability feature of their grid interfaces (inverters, switches, and so on) introduces the provision of several flexibility services like peak power shaving and spinning reserves. Therefore, the traditional top-down approach for the operation of distribution grids based on predictable power flows in the electricity network is not valid anymore in the active distribution grids where DERs lead to unpredictable network flows [4]. Thus, distribution system operators (DSOs) require extensive management and monitoring tools to deliver power to end-consumers in accordance with power quality standards like EN 50160 [5] or EN 61000 [6]. To operate active distribution networks securely and to provide high-quality service to customers, system operators should be able to monitor the behavior (states) of their systems within the appropriate time resolution. Although many monitoring approaches based on the state estimation

(SE) concept have been developed for more than four decades in the transmission networks [7], there are fewer such solutions for distribution grids. The state-of-the-art distribution system state estimation (DSSE) solutions are mostly developed based on the physical model of the power system components [7, 8]. These methods might face convergence issues in the case of applying an inappropriate initial condition, adjusting the termination threshold too low, and dealing with ill-conditioned problems [9]. Additionally, the algorithms associated with these solutions are rather complex and heavy. Thus, they may not meet the requirements of fast automation functions. To alleviate computational complexity, some data-driven modeling solutions have been developed. However, these methods require a large number of measurements to fulfill the observability requirement [10, 11]. Due to the lack of monitoring units in current distribution grids, these solutions may not be applicable in these networks. To tackle the above-mentioned challenges, this dissertation focuses on a new distribution system monitoring solution based on the state estimation concept, which uses an artificial neural network (ANN) as a data-driven modeling technique. This approach is fast, does not have convergence issues, and requires only a handful of phasor measurement units (PMUs) to fulfill the observability requirement [12].

1.1 Motivation

The economic and environmental benefits of integrating DERs, such as flexible loads and small-scale generation units, are the main reasons that drive DSOs to be more determined in utilizing green technologies in their networks [13]. From a technical standpoint, the complex interactions of the DERs and demand-side management in distribution grids lead to several problems, making the operation of active distribution grids more complex. These problems are described below and are recognized by the SE method.

- **Bidirectional Power Flow**: there is a unidirectional power flow in passive grids, from classical energy sources (e.g., coal or nuclear power plants) toward the end-consumers. However, the presence of small-scale sources of energy in active distribution grids causes bidirectional power flow that cannot occur in passive distribution systems. In this respect, the operation of active distribution systems becomes more complex than passive grids [14] since power injection from DERs may locally either increase the voltage at the buses where DERs are connected or cause overloading of the lines connected to the DER's bus. Thanks to the SE solution, nevertheless, the system operator can be aware of the current status of the system at all buses and lines. Consequently, upon recognizing the contingency condition,

they can apply the right control and protection schemes to keep the voltage below the upper limit (defined in standards like EN 50160) and avoid unintended disconnection for end-consumers or unintended energizing of disconnected parts of the grid.

- **Overloading Condition**: the presence of prosumers and electric vehicles (EVs) in active distribution grids may lead to overloading of the grid assets and voltage drop problems if multiple units request demand at the same time [14]. Through the SE solution solution, however, the system operator can identify these contingency conditions. Consequently, they can apply the correct control strategies to safely operate the system, ensuring that the voltage remains above its defined lower limit and the overloading condition is alleviated.
- **Intermittency of Renewable Energy**: the common approach, based on scheduling power generation to manage the daily operation of the electric grid, does not work in active distribution systems. This is primarily due to the intermittent behavior of DERs, prosumers, and EVs [14]. This indeterminacy leads to rapid variations in system states, caused by fast and unpredictable power exchanges between intermittent energy sources and the grid. By leveraging a state estimation solution, system operators can assess the impact of power volatility on the system state. To ensure safe operation, flexibility services, such as operating storage systems, can be employed to compensate for this volatility.

Considering the fact that most of the automation functionalities, such as forecast algorithms, the coordinated control of DERs, on-load tap changers, and SCADA systems, are updated within a range of a few seconds [15], DSOs should apply a robust and fast SE method to obtain a real-time snapshot of the operating state of the entire distribution grid. In this context, the main contribution of this dissertation is described in the next section.

1.2 Contribution

This dissertation presents the following contributions to solving the aforementioned problems:

1. Propose a data-driven, node-voltage-based state estimation method in polar coordinate for the distribution system in Chapter 3. This approach maps synchrophasor measurements into the complex node voltages (node voltage magnitudes and node voltage phase angles) of the distribution system [12]. Compared to classical SE methods, the proposed technique has the following advantages:

- **Fast**: the proposed DSSE method is a data-driven technique based on ANN. At runtime, this method does not involve the time-consuming calculations of the Jacobian matrix and the gain matrix inverse, as in normal weighted least squares (WLS) algorithms. In comparison to WLS methods, where the gain matrix is decomposed (e.g., based on the Cholesky factorization technique), and the solution is iteratively solved by forward–backward substitution [16, 17], the proposed method is linear and yields the solution in a single shot. In contrast to linear WLS approaches using synchrophasor measurements [18, 19], the proposed method involves fewer floating-point operations (FLOPs), as shown in Section 4.3. Therefore, to the best of the knowledge acquired from the literature, the proposed method is the fastest approach for monitoring distribution grids featuring a very large number of nodes.

- **Convergence Guarantee**: unlike existing convergence problems, which are mainly caused by applying inappropriate initial conditions, adjusting termination thresholds too low, and the great disparity of values in the gain matrix of classical SE problems [9, 16], the proposed DSSE approach does not involve gain matrix calculation and its inversion. Instead, the proposed method linearly calculates the system states in a single shot through basic vector operations (e.g., addition and multiplication) over weights (W) and biases (B) of the ANN; and does not exhibit convergence issues, as demonstrated in Section 3.6 [12].

- **Three-phase State Estimation**: considering the unbalanced nature of distribution systems, the states for the three phases of the power system should be taken into account in the operation of active distribution grids. The three-phase model of the power system in the classical model-based state estimation formulation makes the execution of these methods much more cumbersome. However, compared to the model-based methods, an independent ANN-based estimator is dedicated to each phase of the system in the proposed method, as explained in Section 3.7. This, in turn, makes the execution of this DSSE problem much lighter in runtime.

- **Noise Robustness**: due to the high reporting rate feature (more than one sample per second) of the PMU, this measurement unit is used in the proposed monitoring system to satisfy the requirements of fast real-time automation functionalities [15]. However, the PMU measurement noise follows a tailed distribution, which is non-Gaussian [20, 21]. As shown and explained in the results (Section 3.9) of this dissertation, the proposed ANN-based estimator provides accurate estimates under such a noise form.

2. Measure the computational complexity of the proposed ANN-based state estimation method by counting the required FLOPs number. Also, compare this complexity with that of linear and non-linear WLS-based estimators in Chapter 4.

3. Introduce two distributed computation architectures for executing the proposed SE method in Chapter 5.

   - **Parallel Architecture**: to reduce the duration of the training process in offline mode and alleviate the computational cost of the SE problem at runtime, multiple ANN three-phase estimators are executed in parallel.

   - **Multi-Area Architecture**: to augment the proposed SE method with the scalability feature in the operation of a large distribution network, a multi-area architecture has been suggested in this dissertation, which splits the system into several sub-areas. The entire training and estimation process is carried out separately in each area. In addition to scalability, the SE problem is divided into smaller sub-problems in this architecture. Consequently, the training duration and SE execution time are reduced.

4. Introduce a new linear power flow (PF) method that can be used for planning, monitoring, and operating distribution grids in Chapter 6. This method integrates the linear current injection model of P-Q and P-V buses in the fixed-point iterative solver. As voltage is volatile in the distribution system due to the lack of voltage regulators, the considered P-Q bus model is voltage-dependent, yielding more accurate PF results. Nevertheless, the main feature of this PF technique is a linearized model of a synchronous generator represented as a P-V node (voltage-controlled node) [22]. This model is crucial in the analysis of active distribution systems where many active components control the system voltage by synchronous generators or by grid-forming converters (e.g., battery storage systems). In this dissertation, however, this PF method is exploited to generate the required data for training the proposed data-driven DSSE model.

1.3 Dissertation Outline

The contents of this dissertation are organized based on the following structure:

Power system state estimation is defined in **Chapter 2**, and a literature review of various DSSE techniques has also been carried out in this part. In **Chapter 3**, the distribution system state estimation method based on the data-driven ANN-based modeling technique is introduced. After describing the required measurements and the ANN architecture, the integration of the state estimation method in the three-phase system will

be explained. The system observability check, which is an SE prerequisite, is covered based on a probabilistic approach in this part. In the next chapter, **Chapter 4**, the computational complexity of the proposed ANN-based state estimation method is quantified by counting the required FLOPs. Additionally, this complexity is compared with the required FLOPs in linear and non-linear WLS-based state estimation techniques. To alleviate the computational burden during the training and estimation phase of the ANN-based estimators and to improve the estimation accuracy, in **Chapter 5**, the estimation problem is distributed over several smaller problems in a parallel and multi-area architecture. Since the proposed state estimation solution is based on the data modeling concept, the required training data is generated by employing power flow calculation in this dissertation. In this context, a new linear power flow method based on linear models of load and generators is presented in **Chapter 6**. The peculiarity of this approach is in introducing a linear model of a synchronous generator that could emulate the behavior of voltage controllers in distribution grids. Despite providing a specific conclusion at the end of each chapter, an overall conclusion is provided in the last chapter, **Chapter 7**, which briefly represents how the proposed state estimation method in this dissertation can address the real-time requirements for the operation of active distribution grids. In this part, moreover, an outlook suggests conducting some studies to ensure that the considered training data could be fast generated and could cover all the scenarios that may put the system in contingency conditions.

Chapter 2

Distribution System State Estimation & Literature Review

In this chapter, the DSSE is presented as the fundamental core supporting all other distributed automation (DA) functions essential for the operation of active distribution networks. In this respect, a literature review of the state-of-the-art on DSEE has been also carried out in this chapter. This review takes into account both model-based and data-driven DSSE techniques.

2.1 Introduction

In traditional power distribution networks, power flows from the head (HV/MV and MV/LV substation) of each feeder towards the passive loads (consumers). Given this one-way power flow, the grid components (including cables, transformers, switchgear, and protective devices) could be designed during the planning stage to theoretically endure any anticipated peak load throughout their operational lifespan [23]. And if necessary, the measurements (usually the MV busbar voltage magnitude, the Ampere, or active and reactive powers) from only the head of each feeder were sufficient to be used to properly operate these passive systems. Thus, DSOs did not need to deploy measurement units downstream of the feeder's head to see what is going on there. In contrast, the penetration of DERs in active distribution grids causes bidirectional power flows, which may lead to the local congestion of the grid assets and even the malfunctioning of the protection systems. These complex DER interactions with the grid, along with the demand-side management schemes, make the network operation procedure complex. Similar to the energy management system (EMS) in transmission networks, there is a need for an advanced distribution management system (ADMS) for the safe operation of future power distribution networks [23–25]. This system encompasses various DA functions, with the DSSE serving as the central component. The DSSE supplies

crucial inputs for the remaining DAs, enabling them to execute real-time tasks such as outage and congestion management, as well as offline tasks like maintenance, reliability index calculations, and optimal network configuration on a seasonal basis.

2.2 Power System State Estimation

The concept of state estimation (SE) in power systems was initially proposed by Fred Schweppe in the '70s [26]. According to this reference, Schweppe defined the power system states and the power system SE as follows:

" ***The static state of an electric power system is defined as the vector of the voltage magnitudes and angles at all network buses. The static-state estimator is a data processing algorithm far converting redundant meter readings and other available information into an estimate of the static-state vector*** ".

Since that time, SE has been widely used in transmission networks. Due to the lack of a sufficient number of real-time measurements, however, this monitoring function has not been widely implemented on distribution systems [25]. In spite of this restriction, with the emergence of the need for the distribution management system (DMS) in the operation of distribution grids, primary investigations were conducted on the DSSE in the '90s [27–32]. The typical philosophies behind the classical DSSE solutions are based on the developed algorithms for transmission system state estimation (TSSE). Nevertheless, the TSSE solutions should be adapted to be suitable for DSSE since the characteristics of the transmission and distribution systems are different.

2.3 Transmission versus Distribution Systems

To adapt TSSE algorithms for use in distribution grids and to develop new DSSE algorithms, the characteristic differences between the transmission and distribution systems should be taken into account. This includes considerations regarding the network model, measurements, and communication features. [7, 8, 23, 28]:

- **Network model features:**
  - Within distribution grids, power lines exhibit higher resistance ($R \gg X$) when contrasted with transmission lines. Consequently, the separation of the system into active and reactive sub-problems [33] becomes impractical in these distribution systems.
  - The number of nodes in distribution systems is typically much higher than in the transmission networks [34].

- Compared to the transmission systems, which are usually highly meshed, most of the distribution systems are radially operated (to simplify the applied protection schemes). This, in turn, enables the DSSE solution designers to simplify the mathematical formulation of the DSSE problem. For example, one can apply forward/backward tree sweeps instead of dealing with building bus admittance or Jacobian matrices.
- In distribution grids, it is possible that short and long lines simultaneously present at the same bus. This, in turn, may lead to the ill-scaling of the rows/-columns of the involved matrices and accordingly cause the ill-conditioning problem in dealing with the DSSE equation systems.
- Compared to the balanced transmission systems, distribution systems are unbalanced. This, in turn, makes estimators based on the positive sequence model unfit in distribution grids. Thus, three-phase models of the system components should be taken into account in the DSSE mathematical formulation, which complicates the resulting code.
- Precise network models for distribution networks, encompassing details like branch impedances, current network configuration, and phase identification, are seldom accessible, and even network models are missing.

- **Measurement features:**
  - Unlike transmission systems, the scarcity of installed measurement units in distribution systems causes these networks to be unobservable. To address the observability issue (and complement the information gathered from the field), pseudo-measurements, usually the DSO's archived measurements and load flows, are used in performing the DSSE.
  - Compared to transmission networks, distribution grids usually consist of many zero-injection buses that are exploited as zero-injection measurements in DSSE methods. However, using these virtual measurements imposes the ill-conditioning problem [9, 23] since they are much more accurate.
  - Except for PMU measurements, the accuracy of measurements in distribution systems is lower than that in transmission systems. Apart from the redundancy issue, this factor also negatively impacts DSSE estimation accuracy.
  - Exploiting Ampere measurements may impose numerical issues (null or undefined Jacobian coefficients, risk of multiple solutions) in the DSSE solver.

  - Except for PMU measurements, the latency of measurements in distribution systems is higher (minutes or even hours, rather than seconds) than in transmission networks. For example, smart meters often report every 1 hour or at best every 15 minutes. This, in turn, leads to poor estimation results if the interested time frame for operating the system is in the range of seconds or a few minutes.

- **Communication features:**
  - Compared to the transmission networks, there is a lack of voltage regulators in distribution networks. As a result, frequent and rapid variations in the system states occur due to sudden and more frequent load changes. To accurately estimate the system states in this volatile environment, a high-bandwidth communication network is imperative. This network should mitigate issues like latency and time skew arising from asynchronously capturing a substantial volume of data. Presently, DSOs employ narrowband power line carrier (PLC) technology and utilize public 4G networks for data collection. While PLC can traverse the entire network via power lines, it lacks the necessary bandwidth for specific real-time applications. In comparison, 4G networks exhibit lower latency than PLC technology, but their reliability diminishes, especially in certain rural areas where reaching all points becomes a challenge.
  - To protect the distribution networks against cyber threats such as false data injection, topology attacks, and eavesdropping, it is essential to incorporate cybersecurity measures into the management and control of active distribution systems.

2.4 State Estimation Components

Although the main focus of this dissertation is on the core estimation algorithm that calculates the system states, SE consists of various functionalities responsible for preparing the SE inputs and conducting pre- and post-assessments of the system inputs and outputs. Depending on the SE method, there are different functionalities, but they most commonly include the following [34]:

- **SE Algorithm:** this is the core element of the SE system, calculating the system states. Commonly, it is implemented based on the physical model of the power system, as explained in detail in Section 2.6.

- **Bad Data Detection and Identification:** this function detects the measurement inputs that are affected by considerable errors and filters them. The common sources of error are:
  - Random errors due to the finite accuracy of the meters and the telecommunication medium.
  - Large measurement errors resulting from biases, drifts, or incorrect connections of the meters.
  - Incorrect values, such as negative voltage magnitudes or measurements with several orders of magnitude larger or smaller than expected values.
  - Incorrect topology information.

  Depending on the SE method, various bad data detection and identification techniques may be performed before or after executing the core estimation algorithm. However, for common WLS-based SE methods, this function is performed only after the estimation process by processing the measurement residuals [9].

  Topology Processor: this function uses circuit breaker status information and network connectivity data to build the topology of the grid (i.e., a system admittance matrix). The obtained topology is used as input to a network solution program, either a state estimator or a power flow [35, 36].

  Observability Analysis: considering the required estimation accuracy, this function evaluates whether there are enough real-time and pseudo-measurements for the SE algorithm to converge to a solution.

  Database: in addition to the network parameters, this unit contains historical measurements, load flow data, and meteorological information.

2.5 DSSE Measurement Inputs

According to the definition of the SE function, the inputs, including the redundant meter readings and other available information from all parts of the system, are mapped into the state of the system. These measurement inputs are categorized as follows in power distribution systems:

- **Telemetered Measurements:** these measurements may be both analog and digital (on/off status of devices) types and are collected from metering devices deployed in the system:

- **Remote Terminal Units (RTUs):** these devices collect various types of measurements, including the MV busbar voltage magnitude, along with ampere, active and reactive measurements from the primary substation. They are responsible for transmitting measurements to the control center with a sampling rate between a few seconds and a minute [9, 23].
- **Intelligent Electronic Devices (IEDs):** these devices consist of single or multiple microprocessors to send and receive data or control signals to or from an external device (e.g., transducers, relays, control units, etc.). By augmenting the standardization aspect, these units bring interoperability features to the automation of substations. These units are replacing or complementing the existing RTUs [9].
- **Advanced Metering Infrastructure (AMI):** smart meters (SMs), together with the communication network and meter data management system, constitute the AMI. As a key element, SM measures electric energy consumption and provides two-way communication between electricity suppliers and customers for customer billing and system monitoring. The measured data includes energy consumption, real power, reactive power, and voltage magnitude measurements. The measured values are not synchronized. SMs often report every 1 hour or at best every 15 minutes [37–39].
- **Synchrophasor Measurement Devices:** unlike unsynchronized RTU measurements, PMUs, as the most up-to-date metering technology for both transmission and distribution, provide high-precision time-synchronized voltage and current phasor measurements with low latency (high reporting rates in the order of some tens of measurements per second). However, the high costs of commercial PMUs currently available in the market represent an obstacle to their effective deployment [40, 41]. Nevertheless, the adoption of low-cost dedicated hardware platforms such as micro-PMU (μ PMU) or distribution-level PMU (D-PMU) is contributing to their potential massive use in distribution networks [42–44].

- **Pseudo Measurements:** these measurements are usually historical standard load profiles used to address the observability problem arising from the lack of telemetered measurements in the distribution grid [45].
- **Virtual Measurements:** these measurements contain no errors, such as zero injection buses which have neither load nor generation, zero voltage drops in closed switching devices, and zero power flows in open switching devices [7, 16].

Given the features, SE components, and measurement sources mentioned, it's crucial to carefully consider various design aspects to tailor the TSSE algorithms. Specifically, the core estimation algorithm needs consideration for use in distribution grids. This ensures not only the avoidance of observability and convergence issues but also meets the requirements for real-time applications. Besides adapting TSSE methods, these design considerations are the foundation for creating other DSSE approaches, like data-driven alternatives. In the following sections of this chapter, different state-of-the-art model-based and data-driven methods are described and elaborated.

2.6 Model-Driven DSSE

In the domain of power system SE, model-driven methods utilize explicit knowledge of the power system to derive the SE equations. As a common base, the measurement functions corresponding to the available measurements are derived in these methods:

$$z = h(x) + e \tag{2.1}$$

where z is a $(m \times 1)$ measurement vector, x is a $(n \times 1)$ state vector, $h(\cdot)$ is the function of measurements, e is a $(m \times 1)$ measurement error vector, and m and n are the numbers of measurements and states, respectively. In this respect, depending on the selected state and measured variables, type of PF, and inclusion of phase models in PF equations, the measurement function can have different forms, leading to differences between the developed SE methods for transmission and distribution networks. The model-based DSSE problem is mostly solved by applying the WLS methods [7]. Based on the choice of state variables and the techniques to integrate various types of measurements, two basic DSSE formulations have been provided in the literature:

2.6.1 Node Voltage Based DSSE Methods

In this approach, the DSSE typically calculates the system states in terms of bus voltage magnitudes and angles. Traditionally, the measurement vector $h(\cdot)$ (in Equation 2.1) includes the non-linear measurement models of the telemetered measurements (such as real and reactive power flow, bus voltage magnitudes, and line current magnitudes) along with pseudo measurements [28, 31]. Customarily, measurement error is assumed to be Gaussian with zero mean

$$E(e_i) = 0, \qquad i = 1, 2, 3, ..., m.$$

and independent,

$$E(e_i e_j) = 0,$$

Thus, the covariance matrix $Cov(e) = E[e.e^T] = R = diag(\delta_{ii}^2)$. δ_i is the standard deviation of each measurement.

To obtain the system states, then, the following WLS scalar function is minimized:

$$J(x) = \sum_{i=1}^{m} \frac{(z_i - z_i(x))^2}{R_{ii}} = [z - h(x)]^T W[z - h(x)], \qquad W = R^{-1} \tag{2.2}$$

In this way, the gradient of J(x) is set to zero to satisfy the first-order optimality conditions:

$$g(x) = \frac{\partial J(x)}{\partial x} = -H^T(x)W[z - h(x)] = 0 \tag{2.3}$$

where H is the Jacobian of $h(x)$:

$$H(x) = \frac{\partial h(x)}{\partial x}$$

The non-linear Equation 2.3 can be expanded into its Taylor series around the state vector x^k as [9]:

$$g(x) = g(x^k) + G(x^k)(x - x^k) + \cdots = 0$$

Finally, by neglecting the higher-order terms in the above series, the system states are solved in an iterative mode based on the following Gauss-Newton method which is known as the normal equations (NE):

$$x^{k+1} = x^k - G(x^k)^{-1}.g(x^k) \tag{2.4}$$

where

k is the iteration index,

x^k is the solution vector at iteration k,

$G(x^k) = \frac{\partial g(x^k)}{\partial x} = H^T(x^k)WH(x^k)$ and it is called gain or information matrix,

$g(x^k) = -H^T(x^k)W(z - h(x^k))$

The gain matrix can be subjected to ill-conditioning, which is a significant problem in converging this DSSE problem. The potential reasons for this issue could be a combination of various factors, as cited in [9, 23]:

- Simultaneous existence of short and long lines at the same bus
- Assignment of large weights to virtual measurements and low weights to pseudo-measurements

- A large proportion of injection measurements

In addition to these reasons, applying inappropriate initial conditions and setting a termination threshold too low may put the system at risk of convergence issues.

In addition to the considered polar coordinate in the described WLS approach, a new formulation based on rectangular coordinate has been proposed in [29], which converts the power measurements into their equivalent currents. On this basis, the Jacobian terms are constant and equal to the admittance matrix elements. Consequently, the gain matrix $H^T W H$ is constant, and it needs to be built and factorized only once. Thus, the computational complexity is improved in this method. To cope with a large number of zero injection measurements, moreover, a more robust alternative solution that treats these measurements as equality constraints has been proposed in [46], in which the system is formulated on the rectangular coordinate. In dealing with radial networks, [47] introduces another node voltage-based DSSE approach known as the branch-estimation-based state estimation method, which decomposes the WLS problem of the whole system into a series of WLS sub-problems. Each WLS sub-problem deals with only a single branch and can handle all kinds of measurements. Moreover, this approach uses an efficient forward/backward sweep scheme similar to conventional branch-oriented power-flow algorithms, which means that a sparse matrix/vector technique is not needed. To deal with radial or weakly-meshed large-scale medium-voltage networks, a highly computationally efficient DSSE method has been introduced in [48], which exploits a quasi-symmetric impedance matrix TRX to build the network models. However, the system formulation in this approach is complex. To overcome the high computational burden of the pointed non-linear techniques, several works have focused on linear approaches. In this context, despite the cost of introducing modeling errors, [49] has applied some approximations to derive a linear system. However, without imposing the modeling errors, some other solutions [18, 41] have exploited the PMU measurements to integrate a linear vector of measurement functions into the WLS formulation and derived the linear DSSE systems.

2.6.2 Branch Current Based DSSE Methods

In this method, the feeder branch currents are chosen as state variables instead of the customary bus voltages. This method is usually implemented in rectangular coordinate and is computationally more efficient than conventional node voltage-based DSSE methods. It can handle radial and weakly meshed feeders. Like conventional node voltage-based SE methods, the system states (i.e., branch currents) are obtained by performing the WLS approach. When only power and current magnitude measurements

are available, however, the Jacobian matrix is composed of +1, -1, and zeros. Accordingly, the gain matrix is constant and totally insensitive to the system state or line parameters [30, 50]. Consequently, not only is this method more suitable for application to unbalanced systems, but also the computational complexity of this approach is less than that of conventional node voltage-based SE methods. Given the branch current as the system state, then, by applying the forward sweep, the node voltages are found [23, 50]. In weakly meshed systems, moreover, each loop adds an equality constraint on branch currents based on Kirchhoff's voltage law (KVL). These additional constraints can be treated as virtual measurements [51] or exploited as equality constraints in the WLS problem by using Lagrange multipliers [30, 50]. In the case of using voltage magnitude measurements, however, the gain matrix is no longer constant [23, 52, 53].

The two above-mentioned types of WLS-based DSSE methods have been comprehensively compared in [54], both in polar and rectangular coordinates. All four models provide similar accuracy. However, the performance of rectangular formulations is significantly better than that of other polar ones due to exploiting linear measurement functions. From a computational complexity point of view, moreover, the rectangular branch current-based DSSE is the fastest solution.

2.7 Data-Driven Models for DSSE Components

Instead of applying the explicit knowledge of the power system to derive the SE equations in model-based approaches, artificial intelligence techniques are applied to power system data to derive mathematical equations called data-driven models for different components of DSSE. These components include generating pseudo-measurements, optimal measurement placement, observability assessment, bad-data detection, topology identification, and SE. For instance, a probabilistic neural network (PNN) is exploited in [55] to allocate load profiles to loads in distribution systems. In [56], an ANN has been used to generate pseudo-measurements from a few real measurements. Autoencoders are used in [57] to reconstruct missing data, including voltage and power values or switch status information, as a way of generating pseudo-measurements. To design a robust state estimator suitable for medium voltage distribution networks, a load estimation mechanism has been developed in [58] using the concept of parallel distributed processing networks (PDP). For short-term planning (e.g., hours/days ahead), an adaptive nonlinear auto-regressive eXogenous (NARX) model has been introduced in [59] for load estimation in medium voltage distribution networks. A game-theoretic data-driven approach has been introduced in [60] to generate pseudo-measurement samples for DSSE, enhancing the performance of pseudo-measurements and computational

efficiency by exploiting load seasonal patterns. Moreover, many deep learning models based on convolutional neural networks (CNN) [61–63], fully connected networks (FCN) [64, 65], and unshared convolutional neural networks (UCNN) [66] have been developed for load forecasting. Regarding optimal measurement selection for data-driven monitoring approaches, several data-driven methods based on extensions of partial correlation and minimal redundancy maximum relevance criteria to input variable selection (IVS) problems are analyzed in [67]. Concerning system observability, a data-driven method based on the probabilistic concept is developed in [68], which makes it possible to check if the system is observable or not. Bad data detection and identification solutions using neural networks are also proposed in [69] and [70], which identify gross or large errors that may arise from biases, wrong connections of meters, telecommunication system failures, or interference from certain devices. Using PMUs, furthermore, the data-driven denoising framework explained in [71] and [72] can detect outliers from measurement data, enhancing the quality of the measurements. To improve the performance of model-based DSSE methods, some methods use historical data and conduct supervised learning to obtain an educated initial guess [73, 74]. [75] describes a monitoring approach in which the ANN not only estimates the voltage magnitude but also is used to identify the system configuration. A two-step data-driven technique has been explained to identify the topology, estimate line parameters, and recover missing voltage angles without the measurement of voltage angles in [76]. By applying linear regression in the first step, a basic identification of possible topology, type, and initial values for line parameters is obtained. Then, a joint data-and-model-driven method based on the power flow equation and a specialized Newton-Raphson iteration is performed in the second step to calculate line parameters, recover voltage angles, and further correct the topology. In this respect, moreover, [77] proposes a deep learning (DL)-based approach for topology identification (TI) and unbalanced three-phase DSSE, which exploits sparse synchrophasor measurements. To optimally perform reconfiguration per hour, furthermore, [78] proposes a data-driven method based on measurements from μPMUs. Considering the core estimation algorithm, in a fully data-driven SE approach, system states in terms of voltage magnitude and power injections are directly estimated by the ANN in [10] using a large number of measurements, including voltage magnitude and power injections. In this direction, the rest of this dissertation focuses on a new core DSSE estimation technique that uses sparse synchrophasor measurements. This solution does not have the convergence issue as in the WLS method and can be executed tremendously fast, even faster than linear WLS techniques. To satisfy the real-time requirements in the operation of distribution grids, hence, it could be a potential method to be integrated into the ADMS.

Chapter 3

Data-Driven Distribution System State Estimation Using Synchrophasors

This chapter focuses on the first contribution (highlighted in Section 1.2) of this dissertation, which introduces a new data-driven modeling technique based on ANNs. These networks are utilized to perform three-phase distribution system state estimation upon receiving synchrophasor measurements. Based on the design considerations, including the selected architecture of the ANN as the core estimation component, the mathematical formulations correlating the measurement inputs to the system states (node voltages) are articulated. The derived state equations reveal that not only can the proposed estimator be executed significantly faster, but it also does not encounter convergence issues, unlike classical model-based state estimators. Additionally, this chapter examines the performance and robustness of the proposed estimator against various noises and loading conditions.

3.1 Introduction

The lack of voltage regulators in distribution networks causes frequent variations in system states (i.e., voltage magnitude and phase angle) due to changes in loads in traditional systems. The integration of RESs in active distribution grids, however, increases the rate of change of these variations because of the RESs' fast intermittent behavior. To effectively operate active distribution systems, the ADMS should be fast executed to quickly manage these rapid state variations. Since the DSSE function serves as the backbone of ADMS, upon which any other distributed automation (DA) function is based, there is not only a need for a fast DSSE function but also for a fast measurement unit that provides the DSSS function with low-latency measurement inputs. As mentioned in Section 2.3, except for synchrophasor measurement devices such as PMUs and μPMUs, the latency of other meters downstream of distribution systems is high, often in

the range of minutes or even hours, making them unsuitable for tracking the fast variations of operating conditions. For instance, smart meters typically report every hour or, at best, every 15 minutes. In this context, synchrophasor measurement devices play a crucial role in monitoring the active distribution grid since their reporting rates are high, for example, 10, 25 samples per second. Therefore, PMUs/μPMUs are considered as source measurement inputs for the expected monitoring system in this dissertation. On the other hand, a new core estimation technique based on ANN is presented in this chapter and referred to as the ANN-based estimator, which can be executed extremely fast upon receiving synchrophasor measurements. The rest of this chapter introduces PMUs and μPMUs in more detail, provides a brief literature review on state-of-the-art DSSE methods that leverage synchrophasor measurements, and describes the data-driven monitoring approach along with the proposed ANN-based estimator. To meet the observability requirement of the proposed ANN-based estimator, a developed probabilistic approach in [68] is considered in this dissertation. Finally, the performance of the proposed estimator is evaluated in the results section.

3.2 Synchrophasor Measurement Devices

PMUs are advanced measurement devices designed to measure synchrophasors, which are time-synchronized numbers representing both the magnitude and phase angle of the sine waves (such as voltage and current signals) found in power systems [40]. Using a source of time synchronization (e.g., the global positioning system (GPS) signal), each measurement is tagged with the corresponding instant. Thus, wide-area visibility is achievable into what is happening across a wide interconnect power grid [41]. Although PMUs have been widely exploited in transmission systems [79], their use in distribution networks is naturally limited by the high cost of these units [40, 41, 80]. Nevertheless, the adoption of low-cost dedicated hardware platforms such as micro-PMU (μ PMU) or distribution-level PMU (D-PMU) is contributing to their potential massive use in distribution networks [42–44]. The reporting rates of these devices are high. Although PMUs can provide synchronized measurements to within a microsecond [40], μ PMUs report phasor measurements once every 8 to 100 milliseconds [81, 82]. In this respect, the high reporting rates of these measurement devices have made it possible to capture the high dynamic of power distribution systems that cannot be taken by other meters (e.g., smart meters) in these grids [83]. Out of a wide range of applications of PMU/μ PMU in operation, monitoring, protection, modeling, and control of power systems [40, 42], monitoring based on the state estimation concept is the main focus of this dissertation. In this context, a lot of research has been conducted to use synchrophasor measurement in SE problems. In general, PMUs improve the system observability

[84] and enhance the accuracy of the estimations [51]. The impact of the PMUs on the accuracy of estimated results calculated by the weighted least squares estimators is discussed in [85]. [86] proposes an innovative adaptive DSSE solution that adjusts PMU measurement accuracy values and adapts the rate of the DSSE based on operating conditions (steady-state or dynamics) of the network. A model reduction approach based on PMU measurements has been described in [80], which reduces the required number of measurements while satisfying observability and enhancing computational performance. From a mathematical point of view, using only synchrophasor measurements in the WLS-based methods in the rectangular coordinate leads to a linear SE problem [18, 19, 41, 87]. Although the linear WLS-PMU-based solution is computationally more efficient than the non-linear WLS methods, Chapter 4 of this dissertation shows that the proposed ANN-based estimator [12] is executed faster than the linear WLS counterparts upon receiving synchrophasor measurements.

3.3 Data-Driven Monitoring Approach

Compared to model-based SE methods, which apply the laws of electricity to formulate SE problems, data-driven SE methods apply artificial intelligence (AI) training algorithms over a power system training dataset ($D = Z|X$) to train/derive mathematical models that correlate measurement inputs (Z) to power system states (X). In the domain of AI methods, mapping some inputs to outputs is done by applying regression models. On this basis, among the supervised learning methods, the ANN has been selected to perform DSSE for distribution systems in this dissertation since it is one of the powerful non-linear regression methods. Although the computational complexity of ANN training algorithms is heavy, the obtained ANN-based SE mathematical model is more undemanding compared to the complex model-based system of equations, as shown in Chapter 4. Thus, it can be executed much faster than classical SE methods in runtime. Therefore, it is more efficient in real-time applications.

Data is the main requirement in data-driven approaches. In this work, the dataset represents the entire behavior found in the power distribution network. In this respect, the training data is collected either from archived DSO load flow data or from PF calculations or real measured values. To generate the training data, this dissertation uses the data generated by PF calculations. After generating data by performing PF calculations over thousands of random case scenarios, as shown in Fig 3.1, the obtained data is segregated into training input and output datasets corresponding to synchrophasor

measurements and system states, respectively. By applying an appropriate learning algorithm over the input-output dataset, then, the ANN-based estimator is ready to calculate/estimate the system states upon receiving synchrophasor measurements. Finally, the estimated states are used in other distributed automation functions in ADMS.

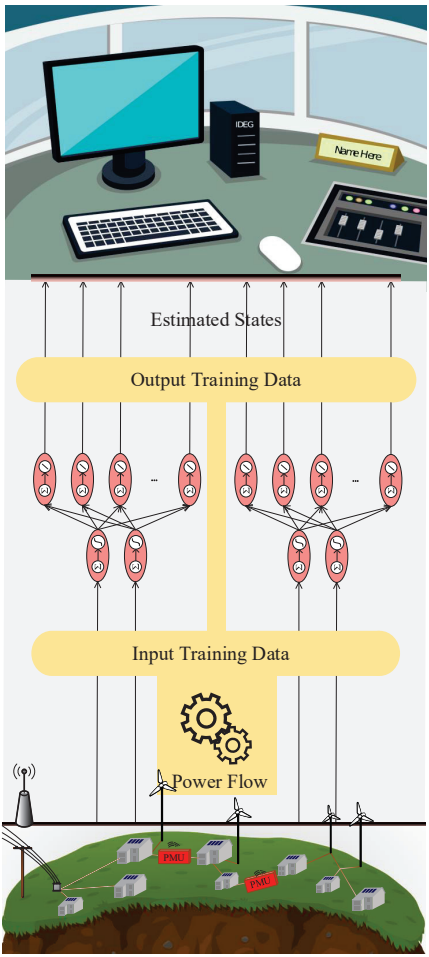

FIGURE 3.1: Data-Driven Monitoring Approach

3.4 ANN-Based State Estimation Components

In addition to the ANN-based estimator, which is the core estimation component in the proposed data-driven DSSE method, the SE system consists of different components as already explained in Section 2.4. In this respect, the proposed core estimation function, explained in Section 3.6, can be equipped with the following developed components:

- **Bad Data Detection and Identification:** to identify gross or large errors that may arise from biases, incorrect meter connections, telecommunication system failures, or interference from certain devices, [69] and [70] have proposed methods using neural networks. Since synchrophasor data is used as the measurement input, furthermore, data-driven denoising techniques have been described in [71] and [72], which detect outliers from measurement data and enhance the quality of the measurements.
- **Topology Processor:** a configuration identification (CI) unit described in [75] dedicates appropriate ANN weights corresponding to the actual configuration of the grid. In addition to this, [77] proposes a deep learning (DL)-based approach for topology identification (TI) using sparse synchrophasor measurements.
- **Observability Analysis:** a probabilistic observability approach described in [68] has been used in this dissertation to evaluate the system observability. This technique classifies a network as observable if, under normal operating conditions, the SE is sufficiently accurate to determine whether the true values of the network parameters are within their respective constraints.
- **Database:** in addition to the network parameters, the power flow calculations, the archived DSO load flow data, synchrophasor measurements, and the trained ANNs for different system configurations are stored in the database of this monitoring approach.

3.5 Quantifying Linear Relationships Between Power Distribution System Variables

As one of the powerful non-linear regression methods, the ANN has been utilized in this work to map the measurements from PMUs to the system states. To assess the degree of non-linearity between the input and output of the ANN in this study, the Pearson correlation coefficient [88] is employed in this section to demonstrate the extent to which paired data of system variables are linearly correlated.

For two variables, A and B, and assuming that each variable has N scalar observations, the Pearson correlation coefficient is defined as:

$$\rho(A,B) = \frac{1}{N-1}\sum_{i=1}^{N}(\frac{A_i-\mu_A}{\sigma_A})(\frac{B_i-\mu_B}{\sigma_B}) \tag{3.1}$$

μ and σ are the mean and standard deviation, respectively. The correlation coefficient matrix of these two variables is the matrix of correlation coefficients as follows:

$$r = \begin{bmatrix} \rho(A,A) & \rho(A,B) \\ \rho(B,A) & \rho(B,B) \end{bmatrix}$$

Considering the fact that each variable is perfectly correlated to itself, the above matrix is written as:

$$r = \begin{bmatrix} 1 & \rho(A,B) \\ \rho(B,A) & 1 \end{bmatrix}$$

For the off-diagonal elements, however, the Pearson correlation coefficient is within the:

$$-1 \leq r \leq 1$$

The closer the value is to 1 or -1, the stronger the linear correlation. Positive and negative values represent positive and negative linear correlations, respectively. Additionally, there is no correlation if the value is equal to zero.

Since the aim of the proposed monitoring system is to map the PMU measurements into the system states, it is important to investigate whether a linear relationship exists between variables without having to fit a specific model (like ANN) to the data in question. In this respect, the degree of linearity among different power system variables has been quantified by the Pearson correlation coefficient over the obtained training data of the considered test system (IEEE 123-bus network) in this work. There are 20,000 scalar observations available for each grid variable in the training data set. The outcome of this quantification is shown in Fig. 3.2 for some exemplary pairs of variables, including the voltage magnitude of node 67 and one of the following variables:

- Voltage magnitude of nodes: 68, 40, 51, 1 and 149
- Voltage angles of nodes: 68, 40, 51, 1 and 149
- Current magnitude of lines: 67-68, 40-42, 50-51, 1-7 and 149 -1

This figure illustrates the dispersion of data for the considered pairs of variables. Additionally, the corresponding Pearson correlation coefficient values are provided. Among

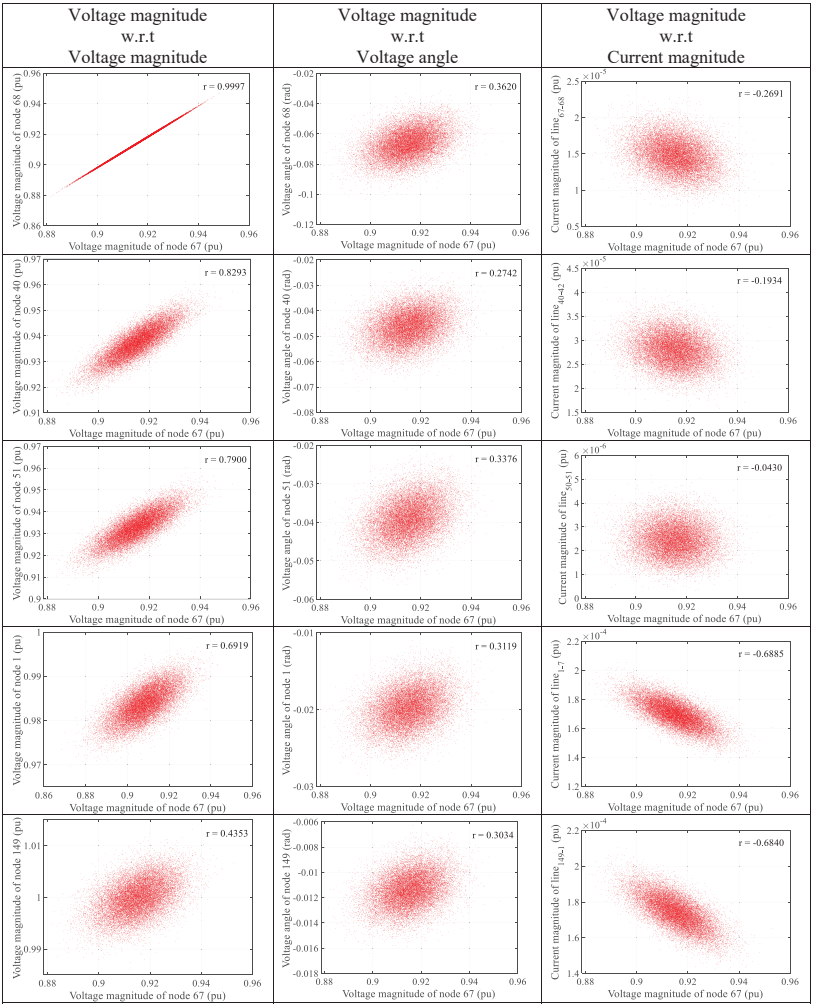

FIGURE 3.2: The scattered plots of various pairs of grid variables along with their Pearson correlation coefficient values

the considered pairs, only the voltage magnitude pair of nodes (67, 68) exhibits a strong linear relationship (r = 0.9997). The perfect correlation in this case may be attributed to the fact that the measured voltages are obtained from neighboring nodes, where there

are minimal relative voltage variations. The correlation coefficients for the other selected pairs range from -0.043 (for the pair involving node 67 voltage magnitude and the line 50-51 current magnitude) to 0.8293 (for the pair involving node 67 voltage magnitude and node 40 voltage magnitude). In addition to the Fig. 3.2, the following figure

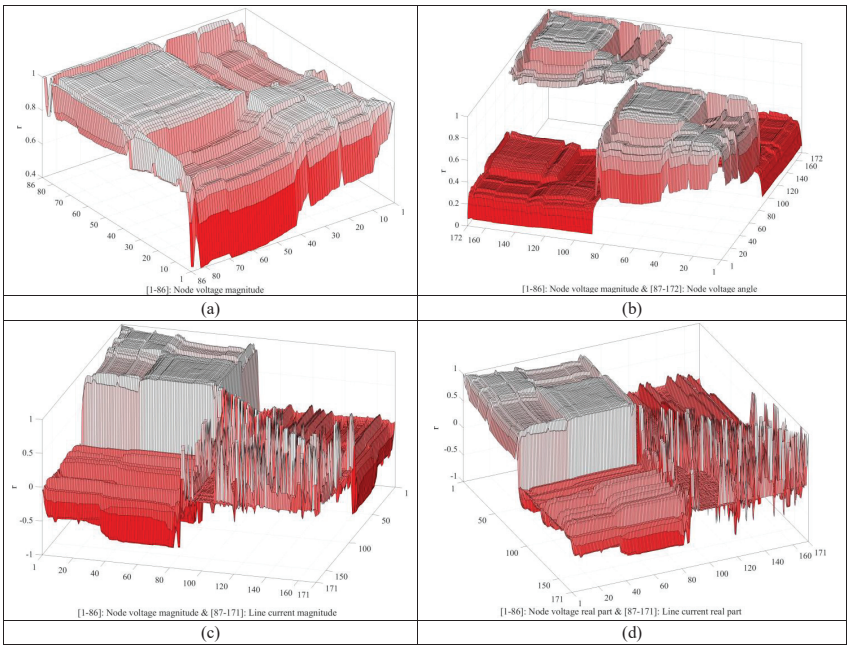

FIGURE 3.3: Pearson correlation coefficient: (a) of the voltage magnitude of all nodes. (b) of the voltage magnitude and voltage angle of all nodes. (c) of the voltage magnitude of all the nodes and the current magnitudes of all the lines. (d) of the real part of the voltage of all the nodes and the real part of the current of all the lines

gives a better picture of how the degree of linearity is changing on the whole system with respect to the voltage magnitude of all nodes (Fig. 3.3 (a)), with respect to the voltage magnitude and voltage angle of all nodes (Fig. 3.3 (b)), with respect to the all nodes voltage magnitude and lines current (Fig. 3.3 (c)), and even in the rectangular coordinate with respect to the real parts of all nodes voltage and lines current (Fig. 3.3 (d)). It is clear that the Pearson correlation coefficient of each variable with respect to itself is 1. However, this measure is within the range of (-1,1) for the pairs including two different

variables. Considering the voltage magnitude of the whole system, the Pearson correlation coefficient (Fig. 3.3 (a)) is around 1 for all pairs including the neighboring nodes. In the case of non-adjacent nodes, however, this measure has even reached the value of around 0.4 for some pairs. For the pairs including the nodes' voltage magnitude and the nodes' voltage angle, this measure is in the range of (0.07-0.4). This means that the degree of linearity between these two variables is low. The degree of linearity could reach the values around 0 for the pairs including the lines' current magnitude and the pairs including the lines' current magnitude and the nodes' voltage magnitudes (Fig. 3.3 (c)). It can be seen even the negative correlations for pairs including the lines' current magnitude and the nodes' voltage magnitudes. Moreover, the same trends have been seen with respect to the lines' current angle. A similar observation has been also seen between the real parts and imaginary parts of the variables in question in the rectangular coordinate. For instance, there are similar trends in both Fig. 3.3 (c) and Fig. 3.3 (d) for the pairs including the lines' current and the voltage of the nodes in the polar and rectangular coordinate, respectively. Finally, regardless of the type of system coordinate (polar or rectangular), a linear relationship does not exist between PMU measurements and most of the system states. Then, the ANN, as one of the powerful non-linear regression methods, has been exploited in this work to fulfill the requirements of this mapping as explained in more detail in the next sections.

3.6 ANN-Based SE

Among AI methods, ANN is a common and powerful solution to establish an accurate mathematical correlation between the input and output training data. According to the **universal approximation theorem** [89], a feedforward multilayer perceptron network with a linear output layer and at least one hidden layer featuring any "squashing" activation function (such as the logistic sigmoid activation function) can approximate any nonlinear function. To map the synchrophasor measurements (inputs) to the system states (outputs) in either polar or rectangular coordinate, a proper training algorithm, later described in this section, is applied to a feedforward network consisting of input, output, and hidden layers. This process is employed to build the data-driven distribution system state estimation (DDDSSE) in this dissertation:

$$DDDSSE : Z \xrightarrow{\text{ANN}} X \tag{3.2}$$

Both polar and rectangular coordinates can be taken into account to map the synchrophasor measurements to the system states. Since the measurement accuracy has usually been defined in polar coordinate for PMU measurements in most research work, such

as [15] (1% for voltage and current magnitude and 1$crad$ for voltage and current phase angle measurements), this coordinate system has also been selected in this work to fulfill the requirement of the following mapping:

$$DDDSSE : Z \xrightarrow{\text{ANN}} X(V, \delta)$$

ANN, as a supervised learning method, requires training data, including input and output datasets. In this dissertation, the training data is generated by means of a three-phase power flow solver, which has been executed over a wide range of operating conditions (thousands of random case scenarios) in which the load powers are randomly varied. To consider the impact of environmental noise on the measurements, the PF data corresponding to the measurements have been corrupted by Gaussian noise (3SD $= 1\%$ for the voltage/current magnitudes and 3SD$= 1crad$ for phase angles).

In addition to the training data, an appropriate node character, network architecture, and learning algorithm should be exploited to minimize the estimation inaccuracy. The main component in the ANN is the neuron. Each neuron is responsible for collecting data from either inputs or other neurons and then scaling it via activation functions. As already explained, a feedforward network consisting of an input, an output, and a hidden layer shapes the network architecture for the proposed estimator. Each layer consists of a set of neurons. In general, it is not possible to analytically calculate the number of layers or the number of nodes to be used per layer in an artificial neural network to address a specific real-world predictive modeling problem. As discussed in [75], however, acceptable solutions for estimating voltage magnitudes are obtained when two neurons are considered in the hidden layer. Considering system states classification with respect to voltage magnitude and phase angle in the output training data, as explained in more detail later in this section, the same number of hidden neurons (two neurons) is also considered in this work to obtain an accurate estimation of both voltage magnitude and voltage angles. The number of neurons in the input and output layers is equal to the number of synchrophasor measurements and the number of considered system states, respectively. To obtain more accurate estimation results, a greater number of neurons (more than two) in the hidden layer or a greater number of hidden layers (more than one) or both may be selected in the ANN architecture. However, a larger ANN architecture may put the ANN-based estimator at risk of the overfitting issue. In this respect, the number of neurons and layers can be gradually increased to meet the required estimation accuracy. In addition to keeping the ANN architecture as small as possible, the Bayesian regularization learning algorithm is used for training the ANN in this work to make the estimator more robust against the overfitting concern. This algorithm makes the estimator less likely to overfit the training patterns [90].

As already pointed out, the flowing data through the ANN network is scaled via activation functions. Referring to the universal approximation theorem, any squashing activation function, such as the logistic sigmoid, can be used for the hidden neurons. As explained later in this section, however, the hyperbolic tangent activation function (tanh) typically performs better than the logistic sigmoid [89]. Therefore, this function (instead of the logistic sigmoid) has been used in this work for the hidden neurons.

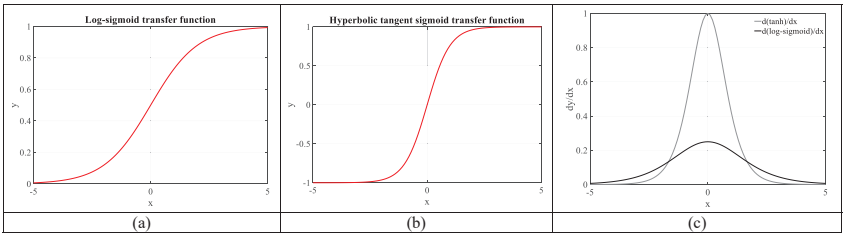

FIGURE 3.4: The output range of both tanh and the logistic sigmoid functions and their rates of change

Fig. 3.4 shows the output range of both the tanh and logistic sigmoid functions. Since $\tanh(0) = 0$ and $\text{logsig}(0) = \frac{1}{2}$, the tanh function more closely behaves like the identity function. Therefore, training a deep neural network $y = b_{Oy} + O_{Wy}(\tanh(I_{Wy}x + b_{Iy}))$ would be similar to training a linear model $y = b_{Oy} + O_{Wy}(I_{Wy}x + b_{Iy})$ as long as the activations of the network can be kept small. This makes training the tanh network easier [89]. In addition, the output of an activation function in the hidden layer is fed as an input to the nodes in the following layer. Therefore, when the sigmoid is the activation function of the nodes in the hidden layer, the directions of the inputs of the following layer (output of the sigmoid is always positive, as shown in Fig. 3.4-(a)) are not changed. Accordingly, the connecting weights of nodes can either all increase or all decrease at the same time in a single step of gradient descent during the training process. By using the tanh activation function in the hidden layer instead, the sign of inputs of the following layer can vary (the output of the tanh could be both positive and negative values, as shown in Fig. 3.4-(b)). Therefore, the directions of the connecting weights of nodes are independent of one another. This makes the learning more flexible [91, 92]. Furthermore, since the rate of change of the tanh function is greater than that of the sigmoid, as shown in Fig. 3.4-(c), the network with the tanh activation function may be learned much more quickly. This is useful when dealing with big data, as the training method could quickly find the local or global minimum for the network using the tanh activation function compared to the network consisting of the sigmoid activation function [92].

The training data mainly consists of various dimensions like volt, radians, and Amperes in this work. The differences within the scales throughout the entire variables may make it difficult to train the estimator [93]. To improve the convergence and generalization tasks, the training data is generally normalized [93, 94]. In this respect, the training input and output matrices are scaled into the range [-1, 1] in this work. To do so, Equation 3.3 is used to process input and output training data matrices by mapping row minimum and maximum values to [y_{min} y_{max}]=[-1 1]:

$$y = \frac{(y_{max} - y_{min})(x - x_{min})}{(x_{max} - x_{min})} + y_{min} \tag{3.3}$$

In this work, each row corresponds to a measurement and a system state in the input and output training matrices, respectively.

It should be noted that mapping the synchrophasor measurements to the system states is a multi-output regression problem since all the system states are expected to be estimated at the same time [95]. Although, in theory, based on the universal approximation

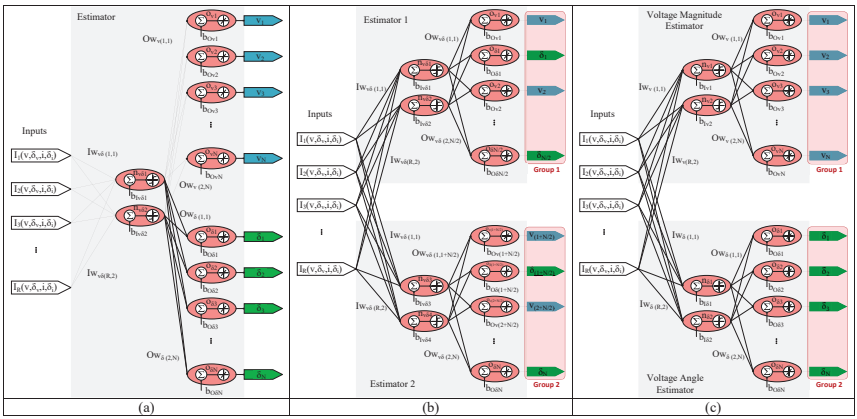

FIGURE 3.5: Training ANNs on different groups of states

theorem, it is possible to fit a feedforward network to satisfy the requirements of this mapping, there would be a problem with the processing time and memory when training the network in the case of large distribution systems. Distributed-based estimation can tackle this issue. It is feasible to divide the target states into smaller groups, each comprising a different combination of the system states. Then, a unique ANN is trained to map the measurements to the states of each group. Thanks to synchronized PMU

measurements, all the trained ANNs of the divided groups simultaneously receive the measurement inputs. Consequently, all the system states are calculated at the same time. To assess the efficiency of the distributed approach, three scenarios are evaluated in which different ANNs, as shown in Fig. 3.5, are trained to map the measurements from 4 PMUs (at nodes 51, 55, 67, and 91) to all phase-A system states of the test system IEEE 123-bus network. In the first scenario, an ANN, as shown in Fig. 3.5-(a), is trained to estimate all the system states. As the training process is rather demanding (trained for nearly 10000s) in this case, the distributed scheme is considered in the second and third scenarios. In this way, in the first step, the output training data is segregated into two groups, with each group containing half of the number of states. In the second scenario, the voltage magnitude and the phase angle of half of the nodes are grouped in group 1, and the voltage magnitude and the phase angle of the remaining nodes are gathered in group 2. In the third scenario, however, the voltage magnitude of all the

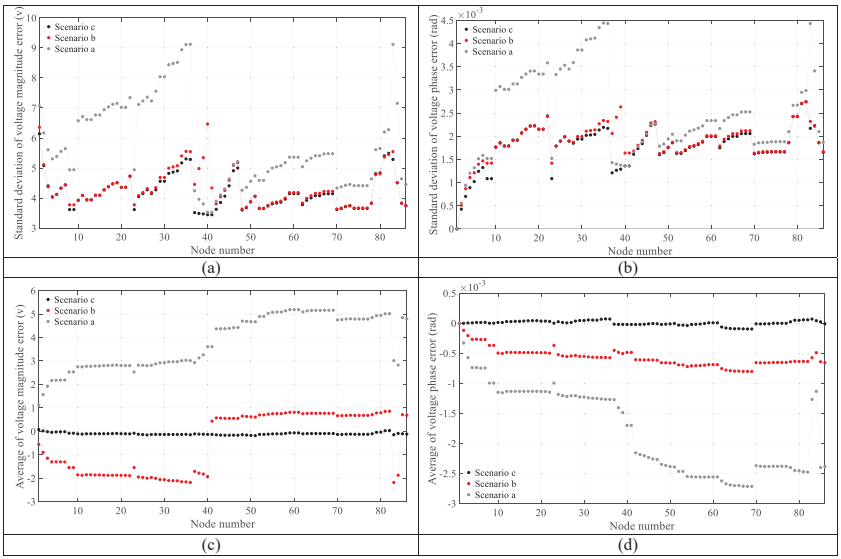

FIGURE 3.6: Standard deviation and average of the estimation errors

nodes is grouped in Group 1, and the phase angle of all the nodes is gathered in Group 2. In the second step, two ANNs are trained to map the PMU measurements to the system states per group, as shown in Fig. 3.5-(b,c). The training process time for each ANN takes nearly 2000 seconds, which is substantially less than the required time to train only one ANN to estimate all the states. To assess the quality of the estimated

states (explained in more detail in the results Section 3.9), the standard deviation and the average of the errors are evaluated. The former indicator indicates how close the obtained estimations are to the true value (PF data), and the latter indicator shows if the estimator has bias. The corresponding results are shown in Fig. 3.6. Fig. 3.6-(a,b) indicate that the estimated states, particularly in scenarios (b) and (c), are very close to the true values in all three scenarios. Except for the trained ANN for scenario (c), there are biases in the estimations of the trained estimators in scenarios (a) and (b). The reason for this could be related to the distribution of the output data. Fig. 3.7 shows how the normalized output data is distributed in scenarios (a) and (b). As can be seen,

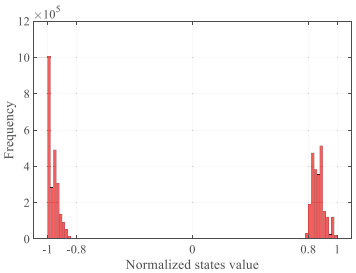

FIGURE 3.7: Distribution of normalized states in scenario (a) and (b)

the data output is accumulated near the ranges [0.8,1] and [-0.8,-1]. The positively nor-

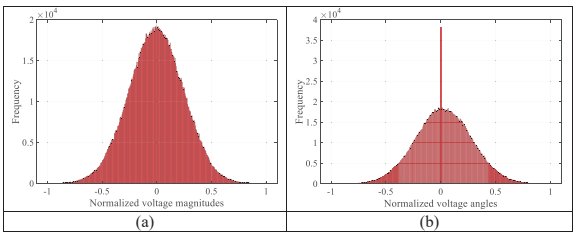

FIGURE 3.8: Distribution of normalized states in scenario (c)

malized data are related to the voltage magnitude, and the negatively normalized data correspond to the phase angle. In scenario (c), however, the distribution of output data is in the range of [-1, 1] for both voltage magnitude and the phase angle, as shown in Fig. 3.8-(a) and Fig. 3.8-(b), respectively. Compared to scenarios (a) and (b), the training algorithm has more flexibility to map the measurements to a wide output range in scenario (c). In other words, it seems that the trained ANNs are overfitted to map the

measurements into the pointed small output ranges in scenarios (a) and (b). To obtain accurate estimation results without biases, the proposed ANN-based estimator consists of two ANNs, as shown in Fig. 3.9 in this dissertation. One estimates the voltage magnitude, and the other calculates the phase angle. Considering these networks, the system

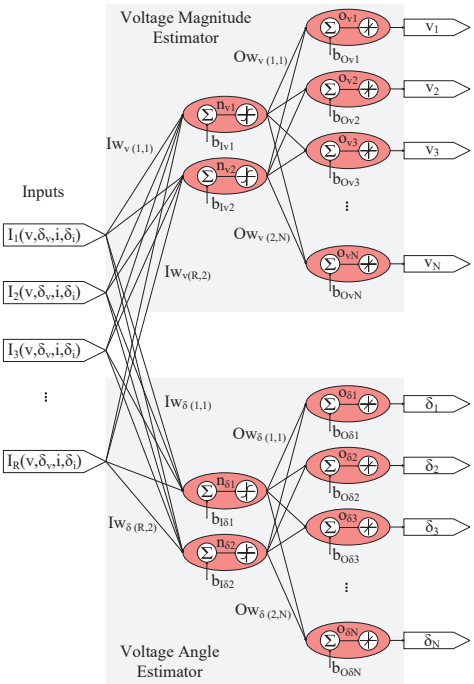

FIGURE 3.9: ANN-Based Estimator

states are mathematically articulated based on the following linear systems:

$$V = b_{Ov} + O_{Wv}(\tanh(I_{Wv}I + b_{Iv})) \tag{3.4}$$

$$D = b_{O\delta} + O_{W\delta}(\tanh(I_{W\delta}I + b_{I\delta})) \tag{3.5}$$

where

V : Estimated voltage magnitude vector

D : Estimated voltage angle vector

I : ANN input vector

I_W : Weight vector of the ANN hidden neurons

O_W : Weight vector of the ANN output neurons

R : Number of elements in ANN input vector

N : Number of elements in ANN output vector

n : ANN hidden neuron number

o : ANN output neuron number

The hyperbolic tangent terms correspond to the activation functions in the hidden layer. According to the SE classifications outlined in Section 2.6, the proposed ANN-based estimation approach is a node-voltage-based SE technique in polar coordinate in this dissertation.

Considering the described basic vector calculations, the proposed estimator does not involve the time-consuming calculations of the Jacobian matrix and the gain matrix inverse, as in normal WLS algorithms. It also does not require network parameters to calculate the grid states in real-time. In this context, the FLOPs number of the proposed SE method is compared with those in other linear and non-linear techniques in the next chapter. Based on this, the proposed ANN-based estimation solution is computationally very low-demanding compared to other DSSE methods. Furthermore, compared to the exploited WLS method in the results section, the computational cost of the proposed approach is significantly low (a few milliseconds). Thus, considering the reporting rate of $f_{PMU} > 1Hz$, by coupling the PMUs to the proposed estimator, a very fast monitoring system, which is the goal of this dissertation, is achieved.

The proposed automation architecture based on international standards (CIM, IEC 61850, and so on) in the IDE4L project [96] can be used to exchange the required data (grid model, measured values, GIS mapping, etc.) from the field to the operating stations.

To deal with changing the system configuration, the ANN weights corresponding to the actual configuration of the grid section are selected based on the output of the configuration identification (CI) unit proposed in [75].

Noise in the environment is another important aspect to be dealt with by the estimator. In this context, the PMU measurement noise follows a tailed distribution, which is non-Gaussian ([20], [21]). Despite the tailed distribution of the PMU measurement noise, as shown in Section 3.9, adding random Gaussian noise to the input training data makes the estimator robust against measurement uncertainty and the impact of the noise.

Providing the training input and output datasets, the ANN-based estimator is trained through a supervised learning method. This, in turn, overcomes the observability issue since the trained estimator calculates one good solution even with very few inputs. However, based on the observability assessment method used in this dissertation (explained in Subsection 3.8) and the shown results in Subsection 3.9, observability improves with considering more inputs in the training process. In this regard, PMUs can enhance system observability since they provide more inputs (the number of measured variables) to the estimator compared to traditional measurement devices. Via multiple PMU channels, it provides the measured voltage phasor (voltage magnitude and phase angle) of the connected bus and also the measured current phasors (current magnitude and phase angle) of lines that connect the PMU bus to the adjacent buses. As a result, by exploiting PMUs, the number of required measurement units to achieve a target estimation accuracy is decreased.

3.7 Three-Phase ANN-Based SE

Unlike the transmission networks, the presence of unbalanced loads, non-transposed lines, and single, double, and three-phase lines causes unbalanced conditions in distribution grids. Thus, the three-phase model of the power system with all the phase quantities, as well as the phase couplings (as shown in Fig. 3.10), is required in the operation of distribution systems. Hence, the TSSE methods based on the positive sequence model are not the right techniques for distribution systems. In addition to this, the formulation of the full three-phase system model, instead of a single-phase one, significantly adds more computational burden in performing the classical SE problems [97]. In this respect, the proposed ANN-based estimator is a powerful technique since not only is it a lightweight solution from the computational point of view, but also it can be easily implemented for all the system phases. To do so, an independent ANN-based estimator is dedicated to each phase of the system while its input training data consist of the synchrophasor measurements of all the phases. For instance, Fig. 3.10 shows the PMU three-phase measurement inputs. Compared to traditional monitoring units, a fewer number of measurement units are required in this approach since the PMUs measure the voltage and current phasors for all three phases of the system (through PMU channels). The input-output training data is calculated by a three-phase PF method or obtained from the three-phase load flow DSO archived data. Therefore, the generated data considers the phase coupling. The proposed PF method described in Chapter 6 generates the training data for the considered case studies in this dissertation. The training output elements are V_a, δ_a, V_b, δ_b, and V_c, δ_c. As the training and the execution of the ANN-based estimator for each phase are independent, these tasks are executed in

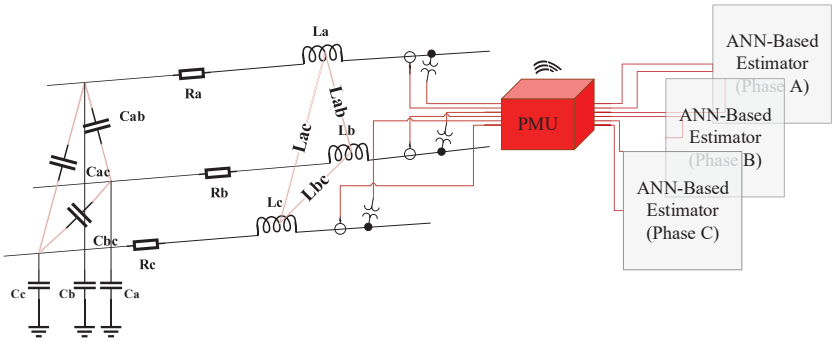

FIGURE 3.10: PMU Three-Phase Measuremnt Inputs

parallel. The algorithm in Fig. 3.11 shows how the three-phase ANN-based estimator is built in offline mode. In the first step, the three-phase load flow solver calculates the bus voltage phasors and the line current phasors for all three phases of the system over a large number of random case scenarios. Then, in the second step, the generated PF data set is segregated into three smaller data packages corresponding to each phase. To make the estimator robust against the impact of noise, the calculated input data corresponding to the synchrophasor measurements are corrupted by random Gaussian noise. In the last step, ANN-based estimators are trained by the Bayesian regularization learning algorithm to synthesize the weights and biases. The created three-phase estimator is ready to be used by DSOs to operate their networks based on power quality standards like EN 50160 [5] or EN 61000 [6]. For instance, they can check if the system voltage is confined within its limits or they can quantify the voltage unbalance to efficiently operate the distribution grids.

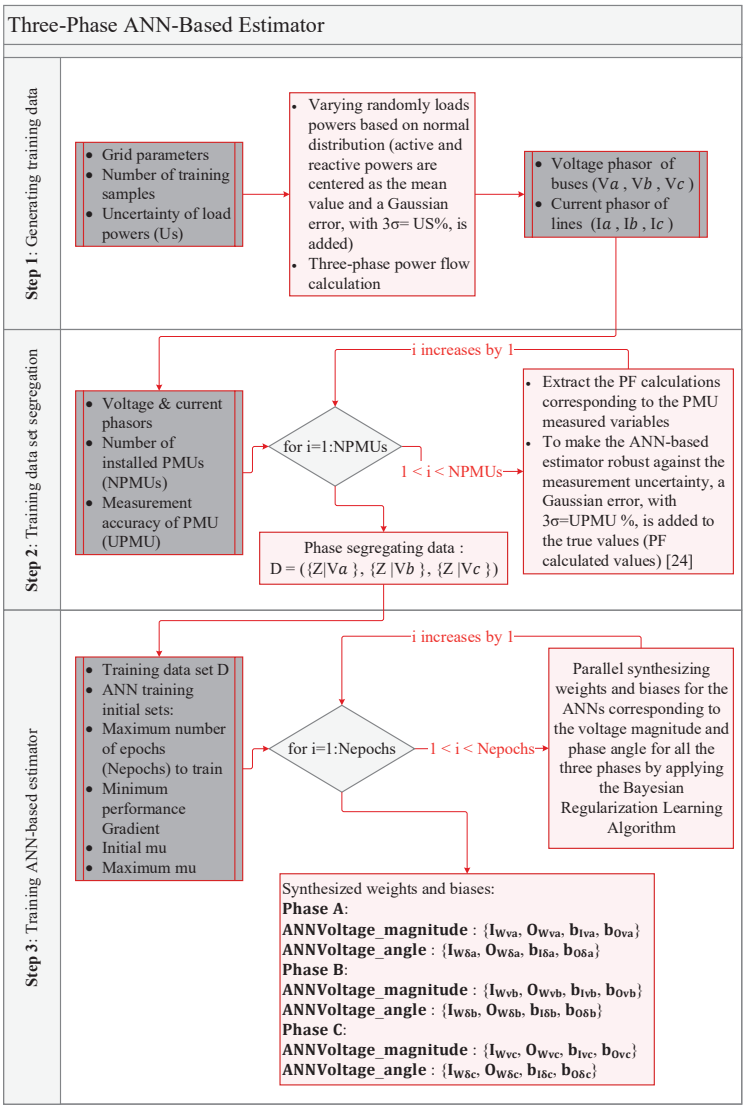

FIGURE 3.11: Algorithm 1

3.8 Observability Assessment

The system observability check is an SE prerequisite. By providing a set of measurements (considering their locations), this assessment indicates whether the estimator is able to calculate the system states. In this respect, the probabilistic observability approach explained in [68] has been used to make the observability check of the proposed ANN-based estimator possible. Considering normal operating conditions, a network is classified as observable by this approach if the estimated states are accurate enough to ensure that the critical grid variables are within their limits (defined in the power quality standards). In the offline mode, accordingly, the following steps should be taken into account for the observability assessment of the ANN-based estimator over the provided testing data set:

1. **Confidence Interval Calculation**: to assess the accuracy of the estimated value, this interval is considered. The endpoints of the confidence interval (CI) are represented by the maximum expected difference between the estimated variable and its true value over the provided test data. Moreover, with a predefined confidence level (CL), the true value is expected to be within this interval. To put it differently, CL is represented as the probability that the true value lies outside of the CI. Thus, the lower CL leads to a higher risk, and vice versa. To calculate the CI, the probability density function (PDF) of the estimated variable is obtained. As the ANN-based estimated states have a Gaussian distribution, the CI is calculated by multiplying the standard deviation (SD) by the coverage factor (k) associated with the predefined CL. Considering n test samples, the CI for the mean μ and different CLs is represented as:

$$[a_{i,min}, a_{i,max}] = \left[\mu_n - \frac{k.SD}{\sqrt{n}}, \mu_n + \frac{k.SD}{\sqrt{n}}\right] \tag{3.6}$$

   where $a_{i,min}$ and $a_{i,max}$ are the CI endpoints.

2. **Required Accuracy of an Estimated Variable**: from the safe operating point of view, the true value of the grid voltage should be confined within its operational constraints described in the power quality standards. To satisfy the working limits, then, the estimated states should be sufficiently accurate. In this respect, the difference between the estimated voltage value and its constraints (e.g. ± 10 % as per EN 50160) is the considered criterion for the required accuracy.

$$MA_{i,min} = [L_{min} - X_i] \tag{3.7}$$

$$MA_{i,max} = [L_{max} - X_i] \tag{3.8}$$

where L_{min} and L_{max} are the minimum and maximum values of the limits, respectively.

3. **Worst Case Scenarios**: in spite of infinite operating conditions, only a limited number of worst-case scenarios are considered. The network's operating limits are most likely to be violated in these scenarios. In general, there are two worst-case scenarios:

   (a) maximum load and minimum generation

   (b) minimum load and maximum generation

4. **Observability Criterion**: given the above-mentioned steps, a network fulfills the observability criterion if the accuracy of every estimated state is equal to or greater than their respective required accuracy values.

$$a_{i,min} \geq MA_{i,min} \wedge a_{i,max} \leq MA_{i,max} \tag{3.9}$$

5. **Observability Level (Compliance Ratio)**: obtaining the ratio between the number of estimates (those that satisfy the observability criterion) and the total number of performed simulations. For example, if the compliance ratio of an estimated variable is equal to 0.99, then the confidence of the estimated value to satisfy Equation (3.9) is 99% of the time.

Finally, a network is classified as observable if the observability level of the system state is equal to or greater than the desired DSO value. In the case that a system does not meet the expected compliance ratio, installing additional PMUs improves the accuracy of estimations, as shown in the next section.

3.9 Results

The ability of the proposed ANN-based estimator for calculating accurate estimations is evaluated in this section. Initially, its performance is compared with the classical WLS-based method. The robustness of the proposed ANN-based estimator against various noise magnitudes and loading conditions has also been assessed. In addition to synchrophasor measurements, other types of measurements can be added to the inputs. In this regard, the estimator's performance when power measurements are included in the inputs is also evaluated. It has been demonstrated that the proposed estimator is robust against both Gaussian and non-Gaussian noises. Finally, its observability is checked using the proposed probabilistic method. To conduct the evaluations, the IEEE 123-bus benchmark test system, as shown in Fig. 3.12, has been used. This system operates at

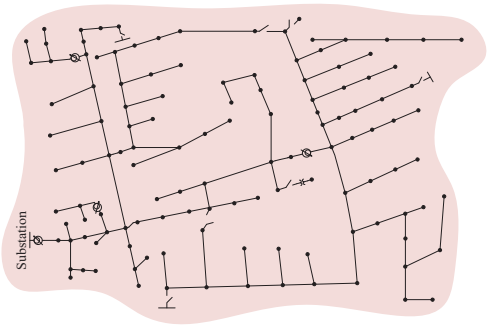

FIGURE 3.12: IEEE 123-bus Benchmark Test System

the nominal voltage (V_n) of 4.16 kV. The grid parameters and the load values are available in [98]. All the tests have been executed using the MATLAB platform on an Intel Core i5-6500 CPU @ 3.20 GHz with 8 GB of RAM.

1. **ANN- vs WLS-Based Estimator**

   Through Monte Carlo analysis, the performance of the proposed ANN-based estimator is compared with the rectangular WLS branch-current estimator explained in [54] in this section. The chosen WLS method is as accurate as other WLS estimators but has a lighter computational burden. Thus, the average and standard deviation (SD) of the errors of voltage magnitude and its angle are considered as accuracy criteria for each phase of the system. The training data, including measurement inputs and system states, are produced by the PF calculations, ensuring that the variation of active and reactive power of loads is based on the normal distribution, as per PF calculation. For the WLS estimator, pseudo-measurements of powers are generated similarly to the load variations to produce the training data sets, which are then corrupted by random noise with uncertainty equal to 50%. The maximum execution time values of both estimators during the Monte Carlo trials are chosen to assess how much faster the proposed ANN-based estimator is compared to the WLS method. To train and execute the estimator, the following assumptions are considered:

   - The training datasets include 20,000 different operating conditions. To this end, the number of Monte Carlo simulations is adjusted to 20,000.
   - During the PF calculations, the loads are normally varied in such a way that their provided values in [98] are centered as the mean value, and the desired

SD is $\frac{100\%}{3}$. Under these assumptions, the system voltage drop exceeds 10% of the system nominal voltage along the feeder. Furthermore, over the performed 20,000 PF calculations, as shown in Fig. 3.13, the voltage variation per node for phase A changes from nearly 3% to 8%. However, the maximum voltage variation is approximately 6.5% and 7% for phases B and C, respectively.

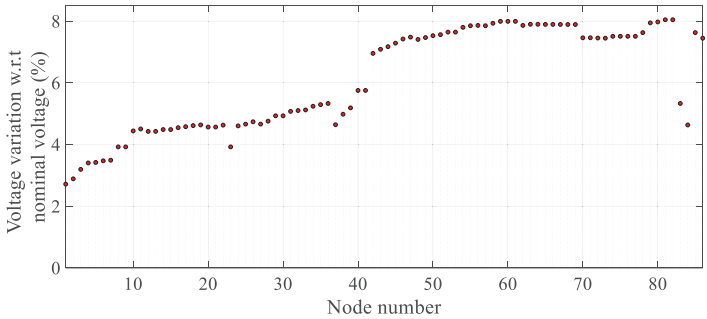

FIGURE 3.13: Node voltage variation w.r.t nominal voltage

- The inputs are synchrophasor measurements monitored at the following nodes:
  (a) **Set 1**: 51, 67.
  (b) **Set 2**: 51, 55, 67, and 91.
- To model the PMU measurements, Gaussian errors with 3 SD = 1% and 3 SD = 1 *crad* are added to the voltage/current magnitudes and phase angles, respectively. These values are calculated by the PF solver and correspond to the synchrophasor measurements.

As already mentioned, the estimators are compared with each other from the following perspectives:

(a) **Estimator Execution Time**: the execution time of both WLS- and ANN-based estimators elapsed during the Monte Carlo trials. The heaviest computational cost for the ANN-based estimator was around a few milliseconds ($\approx 4ms$), and for the WLS-based estimator, it was around a second. However, the WLS-based estimator under test was not optimized to perform real-time fast operations.

(b) **Average Error**: the estimator bias is the difference between the population mean of the estimated values and the true values. Thus, the average value

[99] of the estimation error represents this quality measure. Considering the already measured sets (Set 1 and Set 2), the maximum mean of estimated state errors for voltage magnitude and phase angle, calculated over all nodes, is tabulated in Tables 3.1 - 3.4. Considering two termination tolerance values of 10^{-3} and 10^{-5} for the WLS-based estimator, these results are tabulated per phase in Table 3.1 and Table 3.3 for voltage magnitude and voltage angle estimation errors, respectively. For the ANN-based estimator, the corresponding results are indicated in Table 3.2 and Table 3.4.

Input Set	Termination tolerance value					
	10^{-3}			10^{-5}		
	Phase A	Phase B	Phase C	Phase A	Phase B	Phase C
1	0.2296	0.3831	0.1332	0.1808	0.1039	0.3027
2	0.2814	0.1837	0.2045	0.3363	0.1150	0.1672

TABLE 3.1: WLS-Based Estimator: Maximum Average Voltage Magnitude Error (V)

Input Set	Phase A	Phase B	Phase C
Set 1	0.2185	-0.0236	0.1947
Set 2	0.0748	0.1070	0.2323

TABLE 3.2: ANN-Based Estimator: Maximum Average Voltage Magnitude Error(V)

Input Set	Termination tolerance value					
	10^{-3}			10^{-5}		
	Phase A	Phase B	Phase C	Phase A	Phase B	Phase C
1	0	2.53e-05	8.86e-05	4.52e-05	0	4.12e-05
2	0	1.04e-04	6.04e-05	9.42e-05	4.43e-05	1.53e-04

TABLE 3.3: WLS-Based Estimator: Maximum Average Voltage Angle Error (rad)

Input Set	Phase A	Phase B	Phase C
Set 1	1.0880e-04	5.9315e-05	3.8435e-05
Set 2	1.1971e-04	7.6084e-05	1.7222e-04

TABLE 3.4: ANN-Based Estimator: Maximum Average Voltage Angle Error (rad)

According to the above-tabulated results, there is no biased under- or overestimation of the true values, as the maximum average error of both estimators is close to zero.

(c) **Standard Deviation of the Error**: as another quality measure, the precision of the estimator is evaluated by the statistical variance [99] of the estimation

errors in this dissertation. To do so, the maximum SD of errors for the estimated voltage magnitudes and phase angles observed over all the network nodes is summarized in Tables 3.5 - 3.8. It should be noted that, for 68.2% of the generated random operating conditions, the estimation error of the magnitude and the phase angle over all the nodes falls within the tabulated SDs as per phase. As shown in Tables 3.5 and 3.7, in general, more accurate estimation results are obtained by the WLS-based estimator when there is a lower termination tolerance value. Nevertheless, the tabulated results for the ANN-based estimator in Tables 3.6 and 3.8 are more accurate in comparison with those obtained by the WLS-based estimator. The main reason for this may come from the fact that the ANN-based estimator is trained with the system states that are obtained by the PF solver, which uses the exact loading values. However, the utilized pseudo-measurements [45] in the WLS methods are usually extracted from load profiles that are not exact and deteriorate the estimation accuracy in these problems.

Input Set	Termination tolerance value					
	10^{-3}			10^{-5}		
	Phase A	Phase B	Phase C	Phase A	Phase B	Phase C
1	8.3740	9.6753	9.5616	8.4642	7.7906	8.6967
2	8.1376	8.7192	8.9338	7.9962	7.4531	8.2378

TABLE 3.5: WLS-Based Estimator: Maximum SD of Voltage Magnitude Error (V)

Input Set	Phase A	Phase B	Phase C
Set 1	6.5815	7.1454	9.6701
Set 2	6.3730	6.2742	8.3752

TABLE 3.6: ANN-Based Estimator: Maximum SD of Voltage Magnitude Error (V)

Input Set	Termination tolerance value					
	10^{-3}			10^{-5}		
	Phase A	Phase B	Phase C	Phase A	Phase B	Phase C
1	0.0049	0.0040	0.0046	0.0044	0.0039	0.0045
2	0.0045	0.0039	0.0045	0.0044	0.0038	0.0045

TABLE 3.7: WLS-Based Estimator: Maximum SD of Voltage Angle Error (rad)

Input Set	Phase A	Phase B	Phase C
Set 1	0.0030	0.0031	0.0039
Set 2	0.0028	0.0025	0.0034

TABLE 3.8: ANN-Based Estimator: Maximum SD of Voltage Angle Error (rad)

In general, more accurate estimation results are obtained when the input of the estimators consists of a larger number of measurements. As can be seen in the tables above, using measurement Set 2 rather than Set 1 yields more accurate estimation results.

2. **ANN-based Estimator Operating Point**

As a supervised learning method, ANN has been used to satisfy the requirement of the non-linear regression state estimation model in this dissertation. Considering thousands of random operating scenarios, the training data is generated by PF calculations. To make the ANN robust against environmental noise, the input dataset corresponding to the available measurements is taken from the PF results and corrupted by Gaussian noise according to the uncertainty characteristics of the measurement. The learning method trains the ANN to map the modeled measurements to the system states. Then, upon receiving the measurements, the trained ANN-based estimator calculates the system states based on what it has learned during the learning process. The trained ANN-based estimator accurately estimates the states as long as there are no changes in the system topology, measurement accuracy, load variation per node, and so on. Changes in the pointed conditions may either impact the estimation accuracy or impose bias on the obtained estimations. For instance, five scenarios (a-e) are considered in Fig. 3.14 to show the impact of measurement uncertainty on the estimation accuracy of the phase-A nodes over 2000 test random cases. It is assumed that there are PMUs at nodes 51, 55, 67, and 91 in all of these scenarios. In scenario (a), the measurement uncertainty of inputs is the same as the considered measurement uncertainty (e.g. $3SD = 1\%$ for the voltage/current magnitudes and $3SD = 1crad$ for phase angles) during the training process. According to the obtained results in this scenario (as shown in Fig. 3.14-(a)), 3SD of the voltage magnitude error and voltage angle error are 0.5268% and 0.5221 *crad*, respectively. By increasing the uncertainty of the angle measurements to 2 *crad* in scenario (b), 3SD of the voltage magnitude error and voltage angle error are increased to 0.5605% and 0.7989 *crad*, respectively. This scenario shows that changing the measurement angle uncertainty mainly impacts the accuracy of voltage angle estimations and not the estimation accuracy of the voltage magnitude. The vice versa results have been seen in scenario (c) i.e. changing the measurement magnitude uncertainty mainly impacts the accuracy of voltage magnitude estimations and not the estimation accuracy of the voltage angle. The estimation uncertainty of both voltage magnitude and phase angle is increased to 0.8496% and 0.8195 *crad*, respectively, in scenario (d) where 2 % and 2 *crad* uncertainty are considered for the magnitude and angle measurements.

Scenario	Measurement Uncertainty	Phase A	
a	U_{Vm} = 1% $U_{V\delta}$ = 1 crad U_{Im} = 1% $U_{I\delta}$ = 1 crad	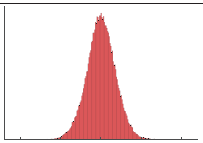	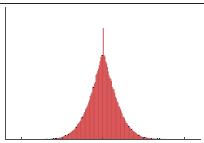
		Average SD of voltage magnitude error (V) = 4.2346 V	Average SD of voltage angle error (rad) = 0.0017 rad
b	U_{Vm} = 1% $U_{V\delta}$ = 2 crad U_{Im} = 1% $U_{I\delta}$ = 2 crad	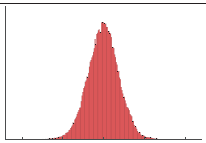	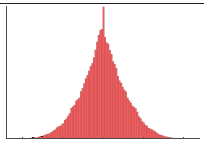
		Average SD of voltage magnitude error (V) = 4.4872 V	Average SD of voltage angle error (rad) = 0.0027 rad
c	U_{Vm} = 2% $U_{V\delta}$ = 1 crad U_{Im} = 2% $U_{I\delta}$ = 1 crad	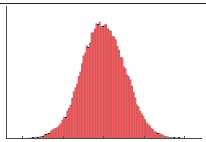	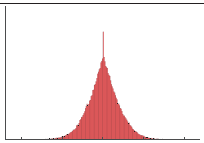
		Average SD of voltage magnitude error (V) = 6.4884 V	Average SD of voltage angle error (rad) = 0.0018 rad
d	U_{Vm} = 2% $U_{V\delta}$ = 2 crad U_{Im} = 2% $U_{I\delta}$ = 2 crad	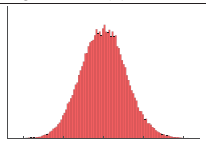	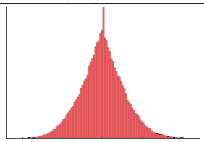
		Average SD of voltage magnitude error (V) = 6.8020 V	Average SD of voltage angle error (rad) = 0.0027 rad
e	U_{Vm} = 10% $U_{V\delta}$ = 1 crad U_{Im} = 10% $U_{I\delta}$ = 1 crad	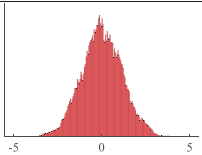	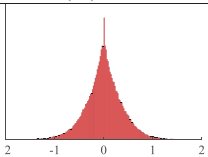
		Average SD of voltage magnitude error (V) = 27.926 V	Average SD of voltage angle error (rad) = 0.0035 rad

FIGURE 3.14: Impact of measurement uncertainty on the estimation accuracy

Maintaining the angle measurement uncertainty at 1 *crad* and increasing the magnitude measurement uncertainty to 10 % yields the voltage magnitude and phase angle estimation uncertainties of 3.4882% and 1.0509 *crad*, respectively, in scenario (e). In this case, similar to scenario (c), the magnitude measurement uncertainty has the dominant impact on the accuracy of voltage magnitude estimations and not on the estimation accuracy of the voltage angle.

Changing the measurement uncertainty impacts the estimation accuracy without imposing any bias. However, when changing the base value of the load per node, biases are introduced in the estimation results. To illustrate this impact, two scenarios are considered in Fig. 3.15. It is assumed that PMUs are present at nodes 51, 55, 67, and 91 in these scenarios. In scenario (a), similar to the load variation in the training phase, the trained ANN-based estimator is tested over 2000 randomly generated test cases in which the loads are randomly changed over their base values (per node). In scenario (b), however, the loads are randomly varied to two times their base values (per node) during the tests. As can be seen, changing the base values of the load deteriorates the estimation quality since biases are present in both voltage magnitude and phase angle estimations. Additionally, the distribution profiles of the estimations are not Gaussian in this scenario (b).

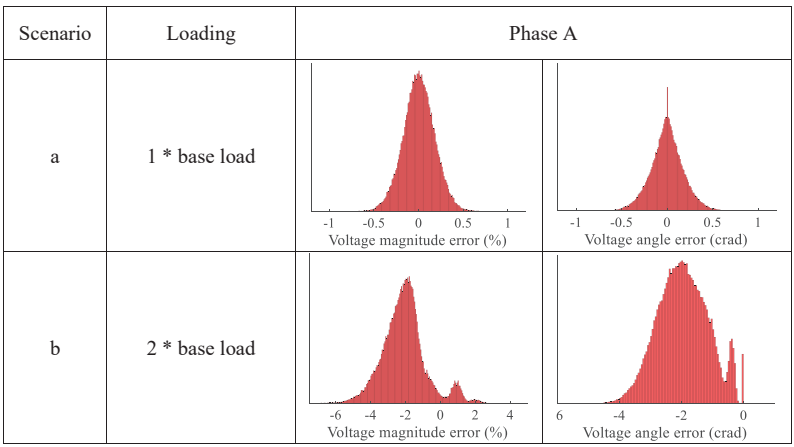

FIGURE 3.15: Impact of changing the loads on the estimation quality

3. **Adding Power Measurements in the Input Set**

Although the main focus of this dissertation is using synchrophasor measurements to perform state estimation by the proposed estimator, it is also possible to include other types of measurements (such as power and even meteorological measurements) in the input set. Considering the fact that some power measurements might already be installed in the substations, in addition to the synchrophasor measurements, the flow of active and reactive powers (with a measurement uncertainty of 1% [100]) is also considered in the input set in this part. To this end, the following input sets are used in training the proposed ANN-based estimator:

(a) **Set 1**: synchrophasor measurements at nodes 51 and 67

(b) **Set 2**: active and reactive power flow at substation and synchrophasor measurements at nodes 51 and 67

(c) **Set 3**: synchrophasor measurements at nodes 51, 55, 67, and 91

(d) **Set 4**: active and reactive power flow at substation and synchrophasor measurements at nodes 51, 55, 67, and 91

The accuracy of estimation results, in terms of the maximum SD of the voltage magnitude error and the maximum SD of the voltage angle error, is provided in Table 3.9. As can be seen, in general, adding power measurements to the input set improves the estimation accuracy. The summarized average of estimation results in Table 3.10 indicates that there are no biases in the estimations.

Input Set	Maximum SD of V_m error (V)			Maximum SD of V_δ error (rad)		
	Phase A	Phase B	Phase C	Phase A	Phase B	Phase C
1	6.5815	7.1454	9.6701	0.0030	0.0031	0.0039
2	6.7221	6.8156	9.2302	0.0027	0.0025	0.0034
3	6.3730	6.2742	8.3752	0.0028	0.0025	0.0034
4	6.5401	6.2858	8.0970	0.0026	0.0022	0.0031

TABLE 3.9: Maximum SD of Voltage Magnitude and Voltage Angle Error

Input Set	Maximum mean of V_m error (V)			Maximum mean of V_δ error (rad)		
	Phase A	Phase B	Phase C	Phase A	Phase B	Phase C
1	0.2185	-0.0236	0.1947	1.08e-04	5.93e-05	3.84e-05
2	0.1015	0.3271	0.0635	4.03e-05	6.08e-05	3.77e-05
3	0.0748	0.1070	0.2323	1.19e-04	7.60e-05	1.72e-04
4	0.1916	-0.0763	0.0999	8.47e-05	4.72e-05	3.11e-05

TABLE 3.10: Maximum Average of Voltage Magnitude and Voltage Angle Error

4. **Noise Robustness of the ANN-Based Estimator**

It is shown in [75] that the trained monitoring unit is robust against noise when the training input data are corrupted by random Gaussian errors. However, its effectiveness against non-Gaussian noise has not been taken into account. Here, the robustness of the ANN-based estimator against noise is assessed:

(a) **Gaussian Noise**: as already pointed out, an estimator trained with input corrupted by Gaussian noise is robust against this type of noise. In this manner, a Gaussian error with $3SD = 1\%$ and $3SD = 1$ *crad* is added to the phasor magnitude and phasor angle of the calculated synchrophasor measurements (via PF solver), respectively. For instance, Fig. 3.16 shows the corrupted voltage magnitude of node 67 during the 20,000 Monte Carlo simulations. Additionally, the other inputs are similarly corrupted with Gaussian noise.

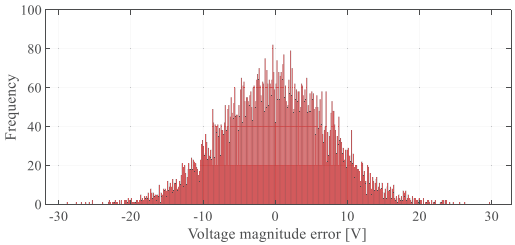

FIGURE 3.16: Corrupted voltage magnitude of the node 67 by the Gaussian noise

Providing training input data Set 2 (synchrophasor measurements at nodes 51, 55, 67, and 91) and adding the input elements with Gaussian error, the performance of the trained estimator in estimating the voltage magnitude at each node is shown in Fig. 3.17.

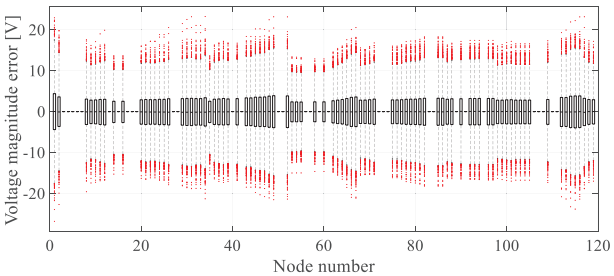

FIGURE 3.17: Per Node voltage estimation error under the Gaussian Noise

The same performance has been observed for the voltage angle on the other phases (Phase B and Phase C) as well. As can be seen, there is no bias in the estimated voltage magnitude of all the nodes. Moreover, the estimator calculates very accurate estimations.

(b) **Non-Gaussian Noise**: considering the fact that the PMU measurement noise follows a tailed distribution, non-Gaussian noise, created by the mixture of two different Gaussian distributions with the following components, is added to the input elements:

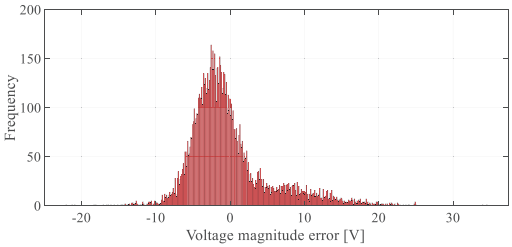

FIGURE 3.18: Node 67 corrupted voltage magnitude by the non-Gaussian noise

i. Gaussian distribution 1: $(Mean, SD) = (-2.40V, 2.64V)$

ii. Gaussian distribution 2: $(Mean, SD) = (4.8V, 7.93V)$

Fig. 3.18, as an example, displays the Gaussian mixture distribution error of the voltage magnitude at node 67. The same distribution is applied to the other inputs when assessing the performance of the estimator.

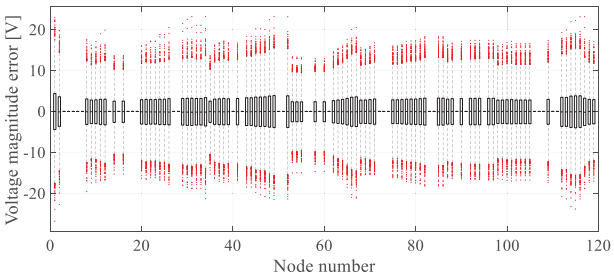

FIGURE 3.19: Per Node Voltage estimated valu of phase A under the non-Gaussian Noise

By conducting 20,000 Monte Carlo tests, it has been found that the proposed ANN-based estimator is robust against non-Gaussian noise. Its estimations

exhibit no bias and are highly accurate, as illustrated in Fig. 3.19. This robustness is also evident in voltage angle estimation and other phases.

5. **Observability Check**

The observability of the proposed ANN-based estimator, according to the suggested probabilistic observability approach, is numerically quantified here, assuming that the desired compliance ratio and the confidence level (CL) are 0.99 and 95 % respectively. The considered lower bound voltage limit in the exploited passive grid is 2161.6 V, $(V_n - (0.1V_n))$. In a stepwise manner, various ANN-based estimators, based on the following synchrophasor measurement sets, were constructed.

- **Set 1**:V_{67}, δ_{67}.
- **Set 2**:V_{67}, δ_{67}, V_{51}, δ_{51}.
- **Set 3**:V_{67}, δ_{67}, V_{51}, δ_{51}, V_{55}, δ_{55}.
- **Set 4**:V_{67}, δ_{67}, V_{51}, δ_{51}, V_{55}, δ_{55}, V_{91}, δ_{91}.

In this study, 10,000 Monte Carlo tests were conducted to calculate the observability level of the ANN-based estimators created. As explained in the following, system observability is achieved when the estimator is trained with the input set 4. In this regard, the voltage estimation error bars across all grid nodes and the convergence trend of the compliance ratio for the non-observable nodes are depicted in Fig. 3.20. All grid nodes, except N110, N111, N112, N113, and N114, are fully observable with the estimator trained using input Set 1, resulting in a calculated compliance ratio of 100. However, Fig. (3.20-*a*) illustrates the error bars corresponding to the mentioned nodes (N110, N111, N112, N113, and N114) exceeding the lower bound voltage constraint (depicted by the red dotted line). For further insight, Fig. (3.20-*b*) indicates that only nodes N113 and N114 are not observable, as the compliance ratio for these nodes (N110, N111, N112, N113, and N114) converges to 99.98, 99.60, 99.30, 95.30 and 93.55, respectively, over 10000 simulation tests. Therefore, only nodes N113 and N114 fail to meet the desired compliance ratio, necessitating additional measurements to achieve the desired observability level. By incorporating additional synchrophasor measurements from Node 51, the compliance ratio is increased. However, Fig. (3.20-*c*) shows that the voltage constraint of the mentioned nodes are crossed. As illustrated in Fig. (3.20-*d*) , nodes N114 and N115 remain unobservable. While nodes N110, N111, and N112 do not exceed the voltage limit (as shown in Fig. (3.20-*e*)) when using inputs from

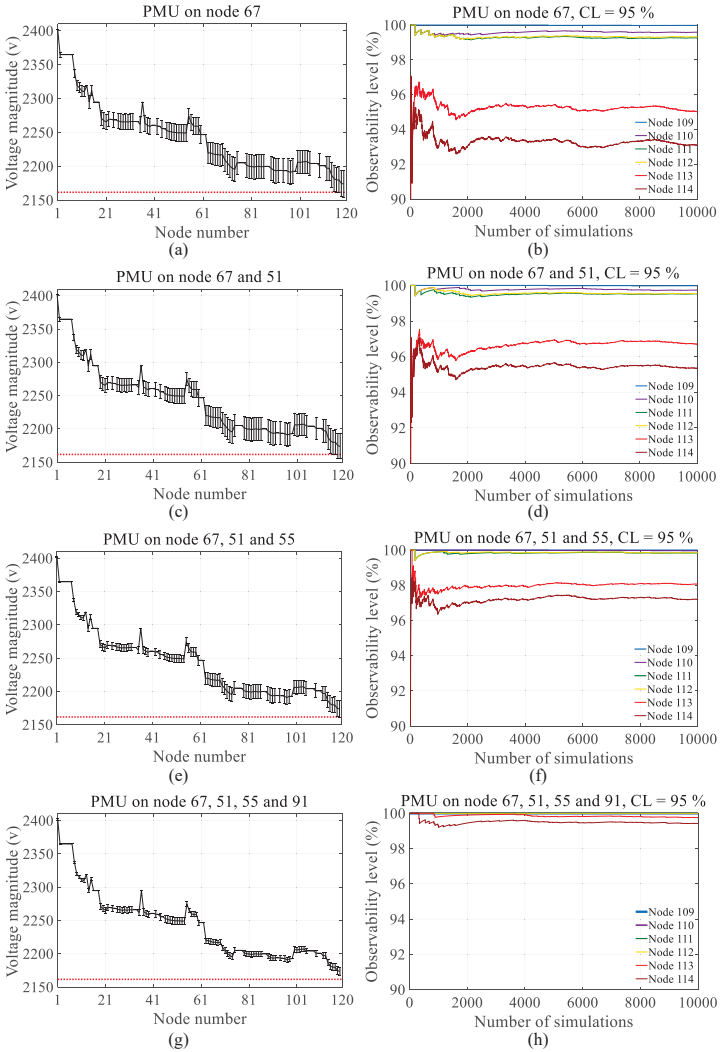

FIGURE 3.20: Observability using different PMUs. Voltage estimation error bar: (a) a PMU is on N67, (c) PMUs are on N67 and N51, (e) PMUs are on N67, N51, and N55, and (g) PMUs are on N67, N51, N55, and N91. Observability level: (b) a PMU is on N67, (d) PMUs are on N67 and N51, (f) PMUs are on N67, N51, and N55, and (h) PMUs are on N67, N51, N55, and N91.

Set 3, Fig. (3.20-*f*) reveals that nodes N113 and N114 fail to achieve 0.99 observability. Finally, the desired system observability is achieved when the estimator is trained using measurement inputs from Set 4. In this case, not only is there no overlap between the error bars and the voltage limit (as shown in Fig. (3.20-*g*)), but Fig. (3.20-*h*) also indicates that the compliance ratios for all five nodes are above 0.99. For other phases (phase B and phase C), observability is addressed using only measurements from Set 1.

3.10 Conclusion

A new distribution system state estimation, exploiting artificial neural networks, is introduced in this chapter. Although the accuracy of the proposed data-driven model is comparable to the classical model-based WLS state estimation technique, it is executed significantly faster than model-based solutions as it does not involve the calculation of the Jacobian matrix and the gain matrix inverse. As shown in the results section, the computational cost of the proposed data-driven method is in the range of just a few milliseconds. Moreover, it has been described how the proposed estimator can be easily expanded for all system phases to recognize the system's unbalanced conditions and how observability is achieved by exploiting a few PMUs. It has also been explained that when input measurements are provided by the PMUs, it is possible to quickly capture the behavior of the distribution grids within a range of seconds. Consequently, the monitoring system, consisting of the proposed ANN-based estimator and the PMUs, can track any fast control actions occurring in the distribution networks.

Chapter 4

Distribution Systems State Estimation Computational Complexity

In this chapter, the computational complexity of different types of DSSE methods, including non-linear and linear WLS-based techniques, and the proposed data-driven ANN-based approach, is compared across various sizes of distribution networks. This is done through the elapsed time, serving as a machine-dependent indicator, and FLOPs, acting as a machine-independent measure.

4.1 Introduction

As discussed in Chapter 1, there are fast and significant changes in the active distribution system states (e.g., the voltage magnitude and the phase angle) due to frequent topological changes and the intermittency of renewable and distributed energy resources. Depending on the requirements of the DSO, a real-time snapshot of the current operating state of the entire distribution grid should be provided at a specific time granularity by the monitoring system. In this respect, the computational burden of the used DSSE method, as the core function in the monitoring system, should be taken into account in the designing procedure, since its reporting rate is limited between the reporting rate of the measurement units and the system operator's expected time resolution for applying automation functionalities, such as forecast algorithms, the coordinated control of DERs, on-load tap changers, and SCADA systems [15]. Commonly, elapsed time is the used indicator for assessing the computational cost of DSSE methods in the literature [12, 25, 74, 81, 101–104]. However, this time is a machine-dependent measure since it is affected by the properties of the machine on which the algorithms, including DSSEs, are being run. These machine properties, for example, are clock rate,

pipelines, parallel processing, caches, storage hierarchy, programming language, compiler, and even the pair of jobs being executed. As a result of these machine dependencies, nevertheless, this measure is not a reliable indicator and might misguide the system designer to pick out a fast enough estimator if the benchmark test grid consists of a small number of nodes and measurements. To understand to what extent a DSSE technique can run quicker than another, regardless of data acquisition and bad data detection steps, this dissertation has exploited the FLOP as a machine-independent criterion instead of elapsed time. In this way, the number of FLOPs, per iteration in the case of iterative solvers, needed for executing different DSSE methods including non-linear [16, 46, 50, 51, 105, 106] and linear WLS-based [18, 19] techniques, and the proposed data-driven ANN-based approach [12], are counted and compared with each other in this chapter. The gain matrix inversion is the heaviest computational part in solving the non-linear DSSE methods. The required FLOPs for the matrix inversion cubically increase with the matrix size. In the case of the DSSE gain matrix, the matrix size is equal to the number of nodes in the distribution grids, which is typically a large number. Therefore, this matrix is heavily inverted for large distribution systems. To subside the computational burden, the gain matrix can be factorized into its Cholesky factors [9]. In [46], moreover, the gain matrix can be decoupled into the real and imaginary parts, and as shown in this chapter, the required number of FLOPs quadratically increases with the number of nodes. To further alleviate the computational burden, exploiting the PMU measurements in the rectangular coordinate leads to the linear WLS-based DSSE method in [18, 19]. Based on the counted FLOPs for this case, the computational cost is linearly dependent on the product of the number of nodes and the number of measurements. As expected, therefore, it runs quicker than the non-linear problems. As a model-based technique, the laws of electricity have been applied to derive this linear problem. On this basis, this method needs the grid parameters in its problem formulation. To be independent of the grid model, [10–12, 75] have used ANN to perform the state estimation. These approaches are tremendously fast. In the context of the proposed ANN-based estimation in this dissertation, the required number of FLOPs is linearly dependent on the sum of the number of nodes and the number of measurements. Consequently, it is executed more quickly than the pointed linear WLS state estimation problem. This chapter, then, shows how the computational complexity for pointed DSSE techniques is evaluated based on the FLOPs. It is worth noting, moreover, the counted FLOP numbers could guide the system designer to select a proper central processing unit (CPU) on which the DSSE algorithm would be run [107, 108]. In the rest of this chapter, the FLOP as a machine-independent complexity measure is introduced and based on which the computational burdens of the pointed DSSE methods are derived and compared with their computational burdens in terms of elapsed time.

4.2 Computational Complexity Based on FLOPs

As a machine-independent measure, the computational complexity of a solver can be represented in terms of floating-point operations or *FLOPs* required to find the solution. In a mathematical operation, a FLOP is considered a basic unit of computation, including addition, subtraction, and multiplication or division. This criterion is used in practical situations when a rough estimation of the solver's computational burden is interesting. Then, compared to the elapsed time affected by machine-dependent aspects like clock rate, pipelines, parallel processing, caches, storage hierarchy, programming language, compiler, and even the pair of jobs being executed, the FLOP mathematically delves into the complexity of an algorithm like the DSSE. Considering the matrix multiplication of $C = AB$ (where $A \in \mathbb{R}^{m \times n}$ and $B \in \mathbb{R}^{n \times p}$), as an example, the result is obtained through the dot product of matrix A and B as:

$$c_{ij} = \sum_{k=1}^{n} a_{ik} b_{kj}$$

Where each c_{ij} requires n multiplies and $n - 1$ adds. Thus, the required number of FLOPs for this product is represented as:

$$\mathcal{O}(C) = \mathcal{O}(AB) = mp(2n - 1) = 2mnp - mp$$

As an effective approach, then, this criterion is exploited in this dissertation to obtain a rough computational cost estimation of the proposed ANN-based estimator. In this context, moreover, this complexity is compared with that in the pointed linear and non-linear WLS-based estimators in the following section.

4.3 DSSE Computational Complexity Based on FLOPs

Considering the pointed ANN-based estimation approach [12], as well as the non-linear methods [16, 46, 50, 51, 105, 106] and linear WLS-based methods [18, 19] for state estimation, their computational complexities are derived based on the FLOP in the following subsections. For the sake of simplicity, the required FLOPs for calculating the Jacobian matrices in the WLS methods are neglected in this dissertation. Additionally, this complexity is counted per iteration in the case of non-linear solvers.

4.3.1 Normal WLS-Based Estimation Method

As explained in Subsection 2.6.1, the system states are iteratively calculated using Equation 2.4, ensuring that an appropriate tolerance is reached for Δx_k. Neglecting the measurement models and the calculation of the Jacobian matrix, the required FLOPs to update the states in this iterative approach are counted per iteration by assessing the necessary FLOPs for the indicated sub-matrices, which are numbered based on their order in the calculation process:

$$x_{k+1} = x_k + \overbrace{G_k^{-1}\, \underbrace{H_k^T\, \overbrace{W\, \overbrace{[z - h(x_k)]}^{[M_1]_{m\times 1}}}^{[M_2]_{m\times 1}}}_{[M_4]_{n\times 1}}}^{[M_3]_{n\times 1}}}^{[M_5]_{n\times 1}} \tag{4.1}$$

Where n in the matrix dimension is equal to the number of states $\big(3(2N-1)\big)$, and m is the number of measurement inputs. Thus, the required FLOPs to update x_{k+1} are counted over the ordered sub-matrices:

Order 1 : $\mathcal{O}([M_1]_{m\times 1}) = \mathcal{O}([z]_{m\times 1} - [h(x_k)]_{m\times 1}) = m$

Order 2: $\mathcal{O}([M_2]_{m\times 1}) = \mathcal{O}([W]_{m\times m}[M_1]_{m\times 1}) = 2m^2 - m$

Knowing that the *transposition* operator needs no FLOP [109], the complexity of matrix M_3 is:

Order 3: $\mathcal{O}([M_3]_{n\times m}) = \mathcal{O}([H_k^T]_{n\times m}[M_2]_{m\times 1}) = 2nm - n$

According to [110], the matrix inversion operation requires n^3 FLOPs. Therefore, the complexity over the next order is:

Order 4: $\mathcal{O}([M_4]_{n\times 1}) = \mathcal{O}([G^{-1}]_{n\times n}[M_3]_{n\times 1}) = n^3 + 2n^2 - n$

Taking into account the n adds in M_5, the corresponding required number of FLOPs is counted in the last order as:

Order 5: $\mathcal{O}([M_5]_{n\times 1}) = \mathcal{O}([x_k]_{n\times 1} + [M_4]_{n\times 1}) = n$

Finally, the required total number of FLOPs per iteration in this approach is obtained by the sum of FLOPs over the pointed orders:

$$\mathcal{O}_{Estimator} = \sum_{i=1}^{order} \mathcal{O}(M_i) = n^3 + 2n^2 + n(2m-1) + 2m^2 \tag{4.2}$$

The most demanding operation in the indicated orders is related to the gain matrix inversion. To deal with this heavy burden, instead, the gain matrix can be factorized into either its QR or Cholesky factors [9, 110]. To demonstrate how this decomposition can alleviate the computational complexity, only the Cholesky method is considered in this dissertation, as it is more efficient than the QR technique [110]:

- **Cholesky Decomposition:** since the gain matrix is symmetric and positive definite, it is possible to represent this matrix as the product of a lower triangular matrix L and its transpose [110]. This decomposition requires $\frac{n^3}{3}$ FLOPs [110]:

$$A = G_k = LL^T$$

In this way, the Equation 2.4 can be represented as:

$$\underbrace{LL^T}_{A}\underbrace{\Delta x_k}_{x} = \underbrace{H_k^T W[z - h(x_k)]}_{b}$$

Then, the obtained $Ax = b$ can be solved by applying the forward/backward substitution steps:

1. **Forward Substitution Step:** in the forward step the matrix y is calculated as:

$$y = (L)^{-1}b$$

2. **Backward Substitution Step:** in the backward step, then, the system solutions are obtained as follows:

$$x = (L^T)^{-1}y$$

According to **Appendix A** and [110], the required number of FLOPs for each forward and backward step is n^2. Considering the number of FLOPs in the previous first three orders, vector b takes $n(2m-1)+2m^2$ FLOPs. In addition to this, n adds are required to update the system states ($x^{k+1} = x^k + \Delta x_k$). All in all, the needed FLOPs to solve the system of Equation 2.4 per iteration are:

$$\mathcal{O}_{Estimator} = \mathcal{O}_{decomposition} + \mathcal{O}_{ForwardStep} + \mathcal{O}_{BackwardStep} + \mathcal{O}_b + \mathcal{O}_{(x^{k+1}=x^k+\Delta x_k)} =$$

$$\sum_{i=1}^{order} \mathcal{O}(M_i) = \frac{n^3}{3} + 2n^2 + 2nm + 2m^2 \tag{4.3}$$

Compared to the calculated sum in Equation 4.2, the required number of FLOPs is

smaller when the gain matrix is decomposed into its Cholesky factors (as counted in the sum indicated in Equation 4.3).

4.3.2 State Estimation Method with Equality Constraints

In addition to telemetry and pseudo-measurements, [16, 46] have utilized zero injection buses, as described in Section 2.5, as equality constraints in the WLS problem. In the approach known as "current-based fast-decoupled SE with equality constraints (CFD/C)", inspired by reference [46], the Lagrange multipliers technique is applied. This technique involves factorizing the gain matrix, which is then decoupled into its real and imaginary parts. Consequently, this method can run more efficiently than traditional WLS methods. To support this claim, the corresponding number of FLOPs for this method is calculated in this subsection after providing a brief problem description. In this SE problem, the system states ($x = v_{re} + jv_{im}$) are calculated by minimizing the following WLS objective function in the rectangular coordinate:

$$minJ(x) = \frac{1}{2} r^T(x) R^{-1} r(x) \tag{4.4}$$

$$s.t.$$

$$c(x) = 0$$

Where $r = \Delta z$ is the measurement residual of $z - h(x)$ derived from the measurement function vector (2.1). The equality constraint vector, which includes zero injections (virtual measurements), has the dimension of $l \times 1$. Considering the Lagrangian optimization problem, the system of Equation 4.4 is solved as:

$$L(x, \lambda) = \frac{1}{2} r(x)^T R^{-1} r(x) + \lambda^T c(x) \tag{4.5}$$

Where λ is the Lagrange multiplier vector. Considering the optimality conditions, then, the estimated states are iteratively calculated by solving the following system:

$$\left[G(x^k)\right] \begin{bmatrix} \Delta x^k \\ \lambda^k \end{bmatrix} = \begin{bmatrix} H^T R^{-1} \Delta z^k \\ -c(x^k) \end{bmatrix} \tag{4.6}$$

Where gain matrix G is:

$$G(x^k) = \begin{bmatrix} H^T R^{-1} H & C^T \\ C & 0 \end{bmatrix}$$

In this approach, equivalent current measurements (ECM) of the power measurements are taken into account at every iteration. Considering the current-based model of the

feeder in [46], the corresponding Jacobian matrix (which is shown in the following system of state equations) is found:

$$\left[H\right]\left[\Delta x^k\right] = \left[\Delta I^k\right] \tag{4.7}$$

where

$$H = \begin{bmatrix} G & -B \\ B & G \end{bmatrix}$$

G and B correspond to the conductance and the susceptance matrices in the ECM-based Jacobian matrix H. On this basis, the term $H^T R^{-1} H$ in the gain matrix could be written as:

$$\begin{bmatrix} G^T R_p^{-1} G + B^T R_q^{-1} B & -G^T R_p^{-1} G + B^T R_q^{-1} G \\ -B^T R_p^{-1} G + G^T R_q^{-1} B & G^T R_q^{-1} G + B^T R_q^{-1} B \end{bmatrix} \tag{4.8}$$

The matrix 4.8 can be simplified in the following matrix since the balanced structured off-diagonal blocks would be much smaller than the corresponding terms in the diagonal blocks:

$$\begin{bmatrix} G^T R_p^{-1} G + B^T R_p^{-1} B & 0 \\ 0 & G^T R_p^{-1} G + B^T R_p^{-1} B \end{bmatrix} \tag{4.9}$$

In this way, the term $H^T R^{-1} \Delta z$ in system of Equation 4.6 is represented as:

$$\begin{bmatrix} G^T R_p^{-1} \Delta z^{re} + B^T R_p^{-1} \Delta z^{im} \\ -B^T R_p^{-1} \Delta z^{re} + G^T R_p^{-1} \Delta z^{im} \end{bmatrix} \tag{4.10}$$

The Jacobian matrix for the ECM-based zero injection measurements, moreover, is represented as:

$$C(x) = \begin{bmatrix} Z_G & -Z_B \\ Z_B & Z_G \end{bmatrix} \tag{4.11}$$

Where Z_G and Z_B contains of G_{ij}s and B_{ij}s. Then, the SE problem is reformulated in system of Equation 4.12 by substituting matrices 4.9-4.11 into Equation 4.6.

$$\begin{bmatrix} G_p & Z_G & 0 & Z_B^T \\ Z_G & 0 & -Z_B^T & 0 \\ 0 & -Z_B & G_p & Z_G \\ Z_B & 0 & Z_G & 0 \end{bmatrix} \begin{bmatrix} \Delta v_{re} \\ \lambda^{re} \\ \Delta v_{im} \\ \lambda^{im} \end{bmatrix} = \tag{4.12}$$

$$\begin{bmatrix} G^T R_p^{-1} \Delta z^{re} + B^T R_p^{-1} \Delta z^{im} \\ -I^{re} \\ -B^T R_p^{-1} \Delta z^{re} + G^T R_p^{-1} \Delta z^{im} \\ -I^{im} \end{bmatrix}$$

I^{re} and I^{im} are the real and imaginary parts of the current of zero-injection measurements in the previous equation. Knowing that $G > B$ in the distribution system, the off-diagonal blocks in Equation 4.12 can be neglected. The following decoupled estimation formulas in the rectangular coordinate are derived, and these are separately calculated in parallel:

$$\begin{bmatrix} G_p & Z_G \\ Z_G & 0 \end{bmatrix} \begin{bmatrix} \Delta v_{re} \\ \gamma_1 \end{bmatrix} = F(x) \begin{bmatrix} \Delta v_{re} \\ \gamma_1 \end{bmatrix} = \begin{bmatrix} G^T R_p^{-1} \Delta z^{re} + B^T R_p^{-1} \Delta z^{im} \\ -I^{re} \end{bmatrix} \tag{4.13}$$

$$\begin{bmatrix} G_p & Z_G \\ Z_G & 0 \end{bmatrix} \begin{bmatrix} \Delta v_{im} \\ \gamma_2 \end{bmatrix} = F(x) \begin{bmatrix} \Delta v_{im} \\ \gamma_2 \end{bmatrix} = \begin{bmatrix} -B^T R_p^{-1} \Delta z^{re} + G^T R_p^{-1} \Delta z^{im} \\ -I^{im} \end{bmatrix} \tag{4.14}$$

Therefore, not only is the gain matrix decoupled into two "identical" sub-gain matrices, but also the update and factorization of the sub-gain matrix need to be done only once. Compared to the normal WLS methods, then, a large SE problem is split into two smaller systems where there is no need to update the gain matrix. As a result, it is expected that the CFD/C state estimation algorithm will run faster than the normal WLS counterparts. In this respect, the required FLOPs in this approach are counted for only one of the above estimation problems, for example, the system of Equation 4.13 in this subsection. In this way, this system can be written based on the Cholesky factorization (done in offline mode) as:

$$\underbrace{F(x)}_{LL^T} \underbrace{\begin{bmatrix} \Delta v_{re} \\ \gamma_1 \end{bmatrix}}_{x} = \underbrace{\begin{bmatrix} G^T R_p^{-1} \Delta z^{re} + B^T R_p^{-1} \Delta z^{im} \\ -I^{re} \end{bmatrix}}_{b}$$

Then, the states are calculated by applying forward–backward substitution at each iteration. In this context, solving $b = Ly$ yields $y = L^T x$ in the forward step. In the backward step, the updated states are then found from $y = L^T x$. Thus, the total needed FLOPs

are counted over these two steps. It should be noted that the FLOPs associated with the ECM-based measurement models are neglected in this dissertation. In this process, however, the number of FLOPs associated with the first element (b_1) of the right-hand side vector (b) in Equation 4.13 is counted based on the order of operations over the following indicated sub-matrices:

$$b_1 = \underbrace{\overbrace{G^T \underbrace{{R_p}^{-1}\Delta z^{re}}_{[M_3]_{N_V\times 1}}}^{[M_4]_{N_V\times 1}} + \overbrace{B^T \underbrace{{R_p}^{-1}\Delta z^{im}}_{[M_1]_{N_V\times 1}}}^{[M_2]_{N_V\times 1}}}_{[M_5]_{N_V\times 1}}$$

The dimension N_V in these matrices is equal to $3N$, where N is the number of nodes in the grid.

Considering $R_I = {R_p}^{-1}$ (that is calculated in the offline mode) and N_V subtractions in Δz^{im}, then, the number of counted FLOPs over the first and the second orders are counted as:

Order 1: $\mathcal{O}([M_1]_{N_V\times 1}) = \mathcal{O}([R_I]_{N_V\times N_V}[\Delta z^{im}]_{N_V\times 1}) = 2N_V^2$

Order 2: $\mathcal{O}([M_2]_{N_V\times 1}) = \mathcal{O}([B^T]_{N_V\times N_V}[M_1]_{N_V\times 1}) = 2N_V^2 - N_V$

There are N_V subtractions, moreover, in Δz^{re}. Then, the number of FLOPs in the next orders is:

Order 3: $\mathcal{O}([M_3]_{N_V\times 1}) = \mathcal{O}([R_I]_{N_V\times N_V}[\Delta z^{re}]_{N_V\times 1}) = 2N_V^2$

Order 4: $\mathcal{O}([M_4]_{N_V\times 1}) = \mathcal{O}([G^T]_{N_V\times N_V}[M_3]_{N_V\times 1}) = 2N_V^2 - N_V$

Order 5: $\mathcal{O}([M_5]_{N_V\times 1}) = \mathcal{O}([M_4]_{N_V\times 1} + [M_2]_{N_V\times 1}) = N_V$

Considering the counted FLOPs over the previous orders, the total FLOPs for the element b_1 are obtained as:

$$\mathcal{O}(b_1) = \sum_{i=1}^{order} \mathcal{O}(M_i) = N_V(8N_V - 1)$$

Focusing on the forward-backward substitution steps, the required FLOPs are counted per iteration as follows:

1. **Forward Substitution Step:** in the forward step the matrix y is calculated from $b = Ly$. Matrices L and b have dimensions of $(N_V + l) \times (N_V + l)$ and $(N_V + l) \times 1$, respectively. According to the **Appendix A**, the require number of FLOPs in this

step is:

$$\mathcal{O}_{ForwardStep} = (N_V + l)^2$$

2. **Backward Substitution Step:** system states are calculated from the system equation of $y = L^T x$ in the backward step. As shown in **Appendix A**, this step takes the same number of FLOPs as the forward step:

$$\mathcal{O}_{BackwardStep} = \mathcal{O}_{ForwardStep} = (N_V + l)^2$$

And, N_V FLOPs are required to updated the system states ($\mathbf{v}_{re}^{k+1} = \mathbf{v}_{re}^{k} + \Delta\mathbf{v}_{re}^{k}$). Therefore, the total FLOPs required to solve the states per iteration in this method are calculated by the following summation:

$$\mathcal{O}_{Estimator} = \mathcal{O}_{\mathbf{b_1}} + \mathcal{O}_{ForwardStep} + \mathcal{O}_{BackwardStep} + \mathcal{O}_{\mathbf{v}_{re}^{k+1}=\mathbf{v}_{re}^{k}+\Delta\mathbf{v}_{re}^{k}} \tag{4.15}$$

$$= 10N_V^2 + 4N_V l + 2l^2$$

4.3.3 Linear WLS-Based State Estimation Method

Exploiting the non-linear model of traditional SCADA measurements in the already-discussed WLS approaches makes the state estimation system non-linear. However, the use of PMU measurements in the WLS approach results in a linear SE system in the rectangular coordinate, as these measurements exhibit a linear relationship with the system states. As demonstrated in [18, 19], this linear system can be expressed as:

$$x = [h^T W h]^{-1} h^T W z \tag{4.16}$$

where

$$\underbrace{\begin{bmatrix} h_V \\ h_I \\ h_S \end{bmatrix}}_{h} x = \underbrace{\begin{bmatrix} z_V \\ z_I \\ z_S \end{bmatrix}}_{z}$$

And, h_V and h_I are linear voltage and current measurements:

$$\underbrace{\begin{bmatrix} u_i & 0 \\ 0 & u_i \end{bmatrix}}_{h_V} x = \underbrace{\begin{bmatrix} \Re\{V_i\} \\ \Im\{V_i\} \end{bmatrix}}_{z_v}, \underbrace{\begin{bmatrix} G_{ij} & -B_{ij} \\ B_{ij} & G_{ij} \end{bmatrix}}_{h_I} x = \underbrace{\begin{bmatrix} \Re\{I_{ij}\} \\ \Im\{I_{ij}\} \end{bmatrix}}_{z_I}$$

Where $\mathbf{u}_i = \Big[0,\ldots,1,\ldots,0\Big]$ is $1 \times n$ unitary vector whose element i^{th} is equal to 1 and other elements are zero. In $\mathbf{h_I}$, G_{ij} and B_{ij} are the real part and imaginary part of the admittance of the line ij. $\mathbf{h_S}$ is the linear pseudo-measurements model.

$$\underbrace{\begin{bmatrix} G_{bus}[i] + u_i P_i & -B_{bus}[i] - u_i Q_i \\ B_{bus}[i] - u_i Q_i & G_{bus}[i] - u_i P_i \end{bmatrix}}_{h_S} x = 2 \underbrace{\begin{bmatrix} \Re\{P_i\} \\ -\Im\{Q_i\} \end{bmatrix}}_{z_S}$$

where $G_{bus}[i]$ is a $1 \times n$ vector whose i^{th} is $\sum_{i \in \mathcal{N}_j} G_{ij}$ and j^{th} element is $-G_{ij}$; $B_{bus}[i]$ is a $1 \times n$ vector whose i^{th} is $\sum_{i \in \mathcal{N}_j} B_{ij}$ and j^{th} element is $-B_{ij}$. And, $\mathcal{N}_j$ is the set of the nodes that are connected to node i. After calculating h_V, h_I and h_S in the offline mode, the equation 4.16 is simplified as:

$$x = Mz \tag{4.17}$$

Where $M = [h^T W h]^{-1} h^T W$ and has dimension of $6N \times m$. Therefore, the number of FLOPs taken by the linear WLS estimation problem is:

$$\mathcal{O}_{Estimator} = \mathcal{O}([M]_{6N \times m}[z]_{m \times 1}) = 6N(2m-1) \tag{4.18}$$

4.3.4 Data-Driven ANN-Based Estimation Method

As explained in Section 3.6, two independent ANN-based estimators are trained to map the PMU measurements to the voltage magnitude and phase angle. This mapping is based on the system of Equations 3.4 and 3.5, respectively. Since these two systems are executed in parallel at runtime, the required number of FLOPs is counted for one estimator. For example, the voltage magnitude estimation function is considered in this subsection. In this manner, based on the order of operations in Equation 3.4, certain sub-matrices are identified as:

$$v = \overbrace{b_{Ov} + \underbrace{O_{Wv}(\tanh(\overbrace{\overbrace{I_{Wv} I}^{[M_1]_{2\times1}} + b_{Iv}}^{[M_2]_{2\times1}}))}_{[M_4]_{N\times1}}}^{[M_3]_{2\times1}}}^{[M_5]_{N\times1}}$$

It is worth noting that the dimensions of sub-matrices correspond to the selected artificial neural network architecture shown in Fig. 3.9. In this respect, 2, M, and N are associated with the number of hidden neurons, the number of synchrophasors from PMU

measurements as the system inputs, and ANN outputs, respectively, which are the estimated voltages of buses in this case. On this basis, the required FLOPs are counted for each sub-matrix based on the following order:

Order 1: $\mathcal{O}([M_1]_{2\times1}) = \mathcal{O}([I_{W_v}]_{2\times M}[I]_{M\times1}) = 4M - 2$

Order 2: $\mathcal{O}([M_2]_{2\times1}) = \mathcal{O}([M_1]_{2\times1} + [b_{I_v}]_{2\times1}) = 2$

The required number of FLOPs for the tanh function should be considered in counting the FLOPs in the third order. According to the [111, 112], however, the complexity of the tanh function is equivalent to five multiplications and three additions, therefore, it requires eight FLOPs in total. Thus, the number of FLOPs taken by order 3 is:

Order 3: $\mathcal{O}([M_3]_{2\times1}) = \mathcal{O}(tanh([M_2]_{2\times1})) = 8 \times 2$

Since the matrix multiplication and matrix summation are performed in order 4 and order 5, respectively, the corresponding number of FLOPs in these orders are:

Order 4: $\mathcal{O}([M_4]_{N\times1}) = \mathcal{O}([O_{W_v}]_{N\times2}[M_3]_{2\times1}) = 3N$

Order 5: $\mathcal{O}([M_5]_{N\times1}) = \mathcal{O}([b_{O_v}]_{N\times1} + [M_4]_{N\times1}) = N$

Therefore, the computational burden of the proposed ANN-based estimation technique is obtained by adding the counted FLOPs over the pointed orders:

$$\mathcal{O}_{Estimator} = \sum_{i=1}^{order} \mathcal{O}(M_i) = 4(N + M + 4) \tag{4.19}$$

SE Method	Number of FLOPs
ANN	$4(N + M + 4)$
Linear WLS	$6N(2m - 1)$
CFD/C	$k\left(10(3N)^2 + 4(3N)l + 2l^2\right)$
Normal WLS with Cholesky factorization	$k\left(\frac{n^3}{3} + 2n^2 + 2nm + 2m^2\right)$
Normal WLS without factorization	$k\left(n^3 + 2n^2 + n(2m - 1) + 2m^2\right)$

TABLE 4.1: FLOPs for Different SE Methods.

After all, the obtained FLOP numbers for the pointed SE techniques are summarized in Table 4.1. As pointed out in Section 3.7, three independent ANN-based estimators are dedicated to the system phases. On this basis, the provided FLOPs for the ANN-based estimator correspond to only one phase of the system. The number of states in the normal WLS method is n, and N is the number of buses. m is the number of measurements (including telemetry and pseudo-measurements) in the pointed WLS-based SE methods. To satisfy the observability criterion, the redundancy should be

sufficiently large $(m > n)$ [113, 114]. M is the number of telemetry measurements $(M < m)$. As pointed out in Section 3.6, since the ANN-based estimator has been trained with PF training data in the offline mode, it does not need to make itself observable by using pseudo-measurements as in the WLS-based approaches in runtime. Considering these points, it can be found that the computational burden of the proposed ANN-based estimator is much less than its WLS-based counterparts. The provided results in the next section could numerically give a relatively rough estimation of the burden of the pointed SE methods.

4.4 Results

To demonstrate the effectiveness of FLOPs in evaluating the computational complexity of DSSE methods, the required number of FLOPs has been counted for various SE techniques outlined in the preceding section. This count was performed across four benchmark test distribution networks in the present section. The FLOPs were determined based on the semi-derived SE system of equations pertaining to these benchmark test grids. In addition to the FLOP metric, the corresponding measured elapsed times were obtained using the MATLAB profiling approach on an Intel Core i5-6500 CPU @ 3.20 GHz with 8 GB of RAM. Despite the DSSE methods used providing sufficiently accurate states, they may demand varying numbers of measurements due to differences in their methodologies. For example, the ANN-based estimator relies solely on telemetry measurements, while WLS-based algorithms also incorporate other measurement types (such as pseudo-measurements and zero-injections) during runtime. In the reference [46], the model of three distribution grids with 15, 30, and 60 nodes (each node consisting of three phase-buses) was utilized to evaluate the performance of the CFD/C SE algorithm. In this section, we consider a modified model of these three systems to compare the complexity of different DSSE solutions. Additionally, to address a larger system, the modified IEEE 123-bus distribution system, where each node consists of a three-phase bus, has been employed. In this case, the measurements used were selected in accordance with [12, 105] to ensure system observability. The number of measurements associated with each system is presented in Table 4.2.

Measurement type	**15-bus**	**30-bus**	**60-bus**	**123-bus**
Telemetry	24	30	48	72
Pseudo measurements	90	180	360	738
Zero-Injection	5	22	38	114

TABLE 4.2: Number of measurements used in SE methods.

Considering the required number of measurements and the size of distribution grids, the computational complexity of the already-discussed estimation methods is tabulated in terms of elapsed time and FLOPs in Tables 4.3 and 4.4, respectively.

SE Method	15-bus	30-bus	60-bus	123-bus
ANN	0.007	0.008	0.008	0.010
Linear WLS	0.038	0.053	0.184	0.995
CFD/C	0.323	0.839	5.804	49.256
Normal WLS (Cholesky factorization)	0.790	2.523	25.654	162.748
Normal WLS (No factorization)	4.950	15.492	74.079	456.593

TABLE 4.3: Required elapsed time(s) for SE methods.

SE Method	15-bus	30-bus	60-bus	123-bus
ANN	172	256	448	796
Linear WLS	20430	75420	293400	1194822
CFD/C	21200	89888	354248	1555866
Normal WLS (Cholesky factorization)	280467	2073609	16045569	135938475
Normal WLS (No factorization)	719382	5770254	46378074	400647990

TABLE 4.4: Required FLOPs for SE methods.

The elapsed time values in Table 4.3 have been measured by the MATLAB profiler over 10,000 trial tests. For example, the measured time for the proposed ANN-based and the linear WLS-based estimation techniques performed on the 15-bus system are shown on the left and right-hand sides of Fig. 4.1. These profilers reveal the percentage of time that has been spent by different parts of the code during solving these SE problems. As

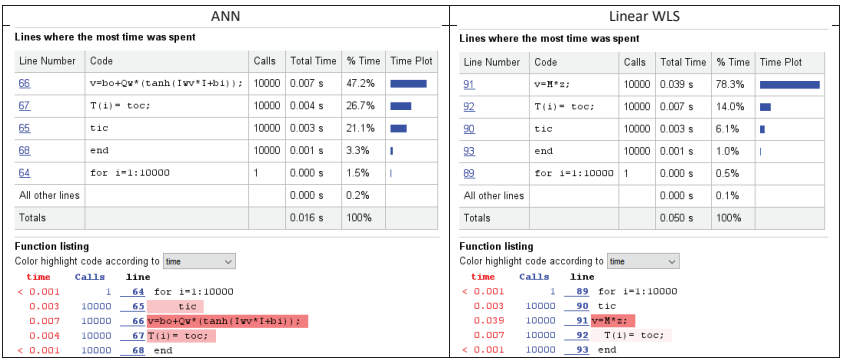

FIGURE 4.1: SE elapsed time taken by MATLAB profiler

can be seen in this figure, the *for loop*, *tic*, and *toc* functions take nearly 52.6% and 21.6% of the total executed time in the case of ANN-based and the linear WLS-based estimators over 10,000 tests, respectively. Thus, as a machine-dependent aspect, this example reveals that the elapsed time depends on the way a code is implemented. To observe the impact of the machine-dependent nature of the elapsed time, moreover, Fig. 4.2 shows that the measured time varies over the performed 10,000 tests and occasionally surpasses the standard deviation band by several orders of magnitude. Focusing on the

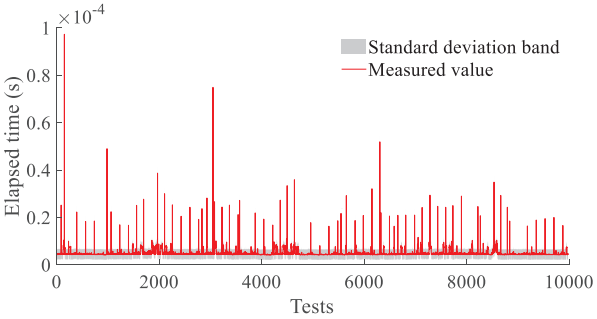

FIGURE 4.2: Measured elapsed time over 10000 tests.

tabulated values in Table 4.3 and Table 4.4, as expected, the larger test grids yield higher values for both elapsed time and the number of FLOPs. Moreover, the non-linear SE methods are more demanding than other approaches. In this regard, the gain matrix decomposition technique significantly contributes to improving the computational performance of non-linear solutions. For instance, the profiler measures 456.593 seconds for performing normal WLS SE on the IEEE 123 test system over 10,000 trial tests where the gain matrix has been inverted. However, by applying Cholesky factorization, this time is reduced to 162.748 seconds. By examining the elapsed time and FLOPs corresponding to the ANN- and linear WLS-based estimators for the 15-bus system, the power of FLOP over elapsed time becomes evident. According to Table 4.3, applying MATLAB profilers on the ANN- and linear WLS-based estimators results in 0.007 seconds and 0.039 seconds, respectively, over 10,000 tests. The ratio of these elapsed times ($\frac{0.039}{0.007}$) is 5.571. The corresponding number of FLOPs for the linear WLS estimator and the ANN-based estimator is $20,430$ and 172, respectively. In this case, however, the FLOP ratio of the linear WLS with respect to the ANN is 118.8, which is way larger than their corresponding ratio of elapsed times. In this way, the FLOP ratio and the elapsed time ratio of linear WLS with respect to the ANN-based estimator are plotted for these four distribution grids in Fig. 4.3. Although both ratios increase with the size of the network, the rate of increase of the FLOP ratio is much larger than the elapsed time ratio.

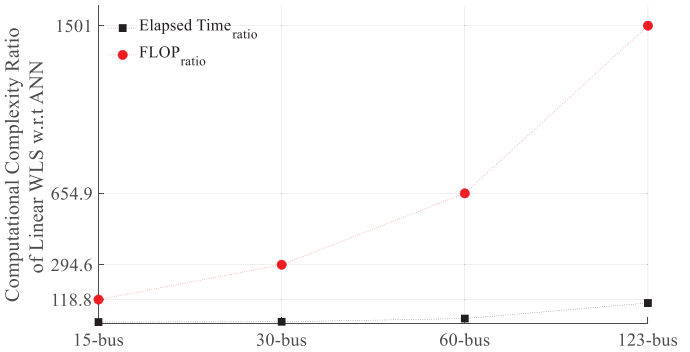

FIGURE 4.3: Computational complexity ratio of linear WLS- over ANN-estimator.

Thus, as a relative performance measure, FLOP is a better indicator than elapsed time. In the case of the bus-30 and bus-60 grids, furthermore, the measured elapsed time by the profiler for the corresponding ANN-based estimators is the same with a value of 0.008s over 10,000 tests (shown in Table 4.3). However, taking a look at the corresponding counted FLOPs in Table 4.4, it is found that the ANN-based estimator trained for the bus-60 system takes 488 FLOPS compared to the 256 FLOPs counted for the trained one in the bus-30 test grid. These case studies, then, show the effectiveness of FLOP over the measured elapsed time in the evaluation of the computational complexity of the DSSE techniques.

4.5 Conclusion

FLOP, as a fair complexity measure, is introduced as a machine-independent indicator in this chapter. Therefore, unlike elapsed time, it cannot be affected by machine properties such as clock rate, pipelines, parallel processing, caches, storage hierarchy, programming language, compiler, and even the pair of jobs being executed. In this respect, FLOP is a robust and reliable indicator. On this basis, the computational burden of different DSSE methods has been compared across various distribution networks consisting of different numbers of buses. Based on the obtained results, in general, the burden of each SE solver increases with the grid size. However, when dealing with systems with a small number of nodes, FLOP proves to be a more effective measure than elapsed time in evaluating the system's complexity. Based on the derived FLOP functions and the corresponding results, it has been shown that the proposed ANN-based

estimator is quicker than WLS-based estimators. To meet the real-time requirements of the monitoring system in large distribution power systems, therefore, it is a potential solution that can be integrated into the ADMS systems.

Chapter 5

Distributed State Estimation Computation

Although the proposed ANN-based estimator has a very light computational burden, the training process of this data-driven model is a demanding task performed in offline mode. One way to reduce the learning computational complexity is to split this task into several smaller problems dealing with smaller training datasets. To this end, this chapter describes two distributed ANN-based state estimation architectures named "parallel" and "multi-area". Both architectures contribute to reducing the training and executing burden of the ANN-based estimator in offline and runtime, respectively. In addition to this, the proposed multi-area approach fulfills the requirement of a scalable method, allowing multiple desired grid areas to be independently monitored by multiple ANN-based estimators.

5.1 Introduction

The generated huge power at conventional power plants, onshore and offshore wind farms, PV plants, and other large power generating units is transmitted through several high-voltage substations and transmission lines towards distribution systems where the power is distributed to different residential, commercial, and industrial areas via many substations and distribution lines. Compared to the transmission systems, however, distribution systems operate at different voltage levels associated with the medium voltage and the low voltage grids. The integration of RESs in the distribution systems, moreover, leads to the already-mentioned power quality issues (in Chapter 1) that should be observed and fixed. To apply suitable countermeasures to operate the system in safe mode, observability downstream of the substations would be required. Nevertheless, applying the appropriate control strategies over the large distribution grid, including several thousand nodes and a large number of active players (e.g., RESs, BESS, and

prosumers), requires not only exchanging a huge amount of data between monitoring devices and the control entities but also performing heavy automation function algorithms (like SE, PF, and so on). Therefore, operating a large distribution network is a cumbersome task if the control and monitoring functions are applied to the integrated system. To address this issue, distribution grids can be divided into smaller subsections (as shown in Fig. 5.1) that do not include a large number of nodes and can be independently operated by a single control entity. Accordingly, the dedicated manage-

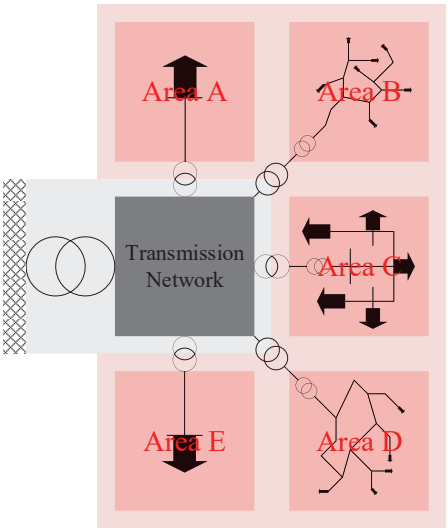

FIGURE 5.1: Sub-Areas in Distribution Network

ment system for each subsection requires performing much lighter automation functions compared to those devised for the integrated large network. Considering the key role of the SE function in the distribution system automation loop, there is a need for SE computation in a distributed manner. To this end, the following sections focus on how a big SE problem can be divided into smaller solutions computed in parallel.

5.2 Parallel Architecture

To enhance the accuracy of the SE and accelerate the training and execution process of the ANN-based estimator for a large integrated power system, the training dataset is divided into smaller packages containing output training data associated with smaller portions of the power grid in this architecture. Instead of dealing with a large dataset

and a large ANN architecture consisting of numerous neurons (associated with many buses) in the output layer, several smaller ANN-based estimators are trained with the smaller data packages corresponding to smaller grid subsections. The divided data packages contain the system states (or training output data) corresponding to the involved buses in the subsections. The synchrophasor measurements from all installed PMUs in the integrated grid, however, serve as the training input data. Therefore, a fewer number of weights and biases are tuned during the training process in each divided area over the same measurement inputs. This, in turn, reduces the computational cost in the training phase. As fewer weights and biases are processed in the SE phase in this approach as well, the ANN-based estimator executes faster than the estimator trained for the integrated system. Considering similar input datasets in both the integrated and the proposed parallel approach, the training algorithm for all the ANN-based estimators dedicated to the sub-areas deals with fewer numbers of weights and biases. Therefore, it has more freedom to more accurately map the input measurements to a fewer number of system states for each area. As a result, the aggregated estimated states from all the sub-areas are more accurate than those calculated by the estimator designed for the integrated grid. It is worth mentioning that the training and the execution of the dedicated estimators for the sub-areas are independent of each other. Therefore, the required computations (e.g., training and executing) for the divided areas are treated in parallel. This is why the described distributed computation for the proposed ANN-based estimation approach is named the "Parallel Architecture." To minimize the overall execution time of SE and prevent a scenario where no ANNs serve as bottlenecks in the parallel computation process, allocating an equal number of nodes per divided area would be the ideal criterion for segregating the training data into smaller packages. As already mentioned in Subsection 3.7, three independent ANN-based estimators for the three phases of the system are trained and executed in parallel. Subsequently, these estimators are seamlessly integrated into the proposed parallel architecture. In this context, the proposed approach is schematically demonstrated in Fig. 5.2. The exemplary grid shown in this figure is divided into three sub-areas: A1, A2, and A3. Aside from the nodes (indicated by the red cubes) monitored by the PMUs, the number of other nodes is consistent in each subsection (eight cubes). The entire segregated data packages, indicated in light gray, gray, and black colors, corresponding to each area, along with the monitored data, are also displayed. To train the ANN-based estimators for each area in the parallel architecture, the entire data package is divided into three smaller packages based on the designated colors. Subsequently, three datasets associated with the three phases of the grid are extracted from each data package. From a parallel computation perspective, an ANN-based estimator for each phase of the system in all the divided

packages is simultaneously trained. Finally, the estimated states are calculated by parallel execution of the ANN-based estimators upon receiving the PMUs' measurements.

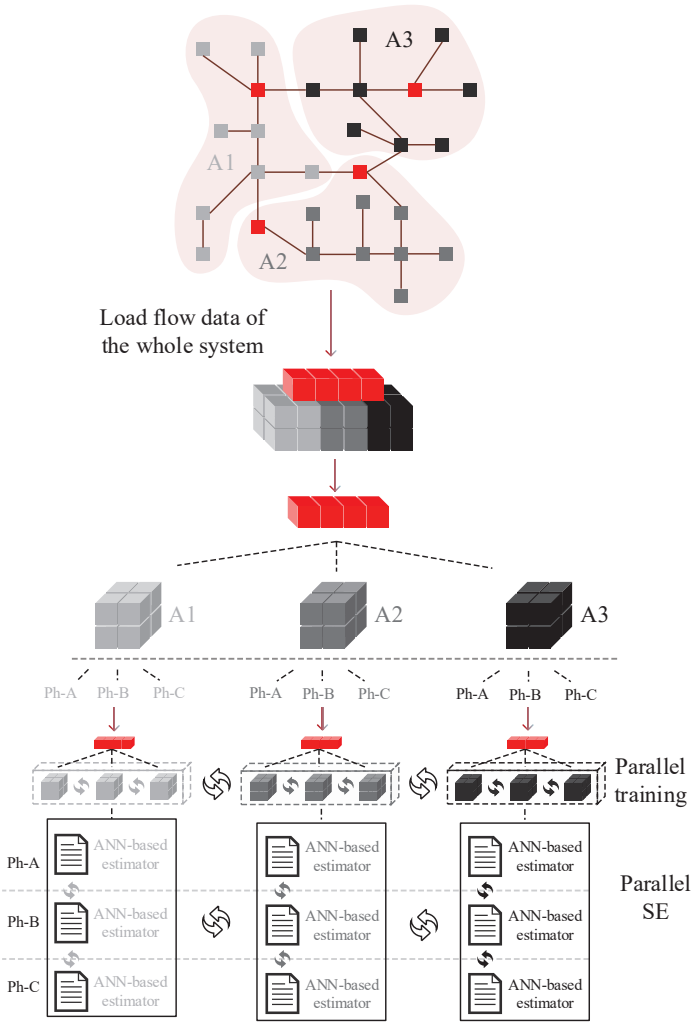

FIGURE 5.2: Parallel Training and Execution of ANN-Based Estimators

5.3 Multi-Area Architecture

As another distributed computation method, multi-area architecture is an important concept applied in wide-area interconnected power systems to distribute the monitoring, automation, and control computation burdens over different local management systems. Apart from reducing the automation function execution time, this concept allows system operators to independently operate their grids. In this way, the power system is split into several sub-areas (zones), where local management systems operate and control their zones. Focusing on the SE function, several studies have been conducted to implement this concept. Various state-of-the-art multi-area SE (MASE) approaches for transmission grids have been introduced in the literature, differentiated in terms of the subdivision procedure, the type of estimator, and how multi-area is performed in the estimator [115–118]. Due to the different specifications of these systems with respect to distribution grids pointed out in Subsection 3.1, however, these methods cannot be directly applied in distribution systems [119]. In this context, nevertheless, few works are focusing on distribution grids. Garcia and Grenard introduced a two-step MASE method for distribution grids in [120]. The system states are locally calculated by the WLS estimators in the first step. Then, the system voltage profile is centrally harmonized among the subareas in the second step. However, the computational burden is rather heavy in this method since the exploited estimation algorithm is based on the WLS formulations. A data-driven multi-area approach based on a differential evolution algorithm has been introduced in [121]. The cost of communication is high in this method as the local estimators require exchanging data with the adjacent zones in each iteration of the algorithm. To subside the computational burden, make it possible to use low data exchange among the subareas, perform SE in a decentralized scheme, and improve the SE accuracy, different two-step multi-area techniques, in which the local estimators are WLS-based, are also presented in [119], [122], and [105]. The computational burden of the algorithm is rather heavy since the estimation solution in these works is nonlinear. To have a much lighter solution, a decentralized ANN-based SE approach is proposed in [11]. In this approach, the ANN estimates the loads' consumption of the balanced systems. This solution exploits the non-synchronized measured values from a large number of smart meters and requires the load flow data from the integrated system. Therefore, independent operators should share their grid parameters and run the PF calculations on large grids, which is a cumbersome task. In this dissertation, a data-driven MASE based on the proposed ANN-based estimation technique is introduced, which is executed very fast and needs low data exchange among neighboring areas. It can be integrated into both centralized and decentralized schemes. The design considerations and the solution are described in detail in the following parts.

1. **Multi-Area Design Considerations**:

   The following factors are considered in designing the MASE:

   (a) A decentralized scheme is exploited in this dissertation, based on which the local system management independently performs the following tasks:

   - PF calculations for data generation
   - Training the local estimators
   - SE execution

   (b) As one of the grid decomposition factors in this work, zone partitioning is done based on possibly having a similar number of nodes for each zone.

   (c) As another grid decomposition factor, the zones are decoupled from each other at the overlapping nodes.

   (d) PMU presence at the overlapping nodes is intended to fulfill:

   - The observability of different areas with a fewer number of measurement points
   - Data synchronization of different areas

2. **Data-Driven Multi-Area DSSE Solution**:

   The proposed ANN-based multi-area DSSE method consists of the following two phases:

   (a) **Training Phase**: to train the dedicated ANN-based estimators for the divided sub-areas, the training data specific to each zone is required. To this end, the training dataset for each subarea is generated through PF calculations in a decentralized manner, as follows:

   - The presence of a large number of nodes in the integrated distribution grids, along with the inclusion of the three-phase power system model in the PF formulation, results in a significant computational burden during each PF run. Therefore, the decentralized execution of the PF problem, organized by zone, serves to distribute the computational cost of a large PF problem into smaller and more manageable sub-problems.
   - A scalable solution is desired. In the operation of the power system, grid monitoring is not deemed essential for certain portions of the grid, and a sophisticated control scheme is unnecessary for these sections (e.g., passive sections). Therefore, there is no need to generate training data or

allocate state estimators for these areas. Additionally, in some cases, grid parameters are unavailable for certain parts of the system. Consequently, training data cannot be generated, and as a result, state estimation is not applied in these specific areas.

To implement decentralized PF calculations, network decomposition is carried out based on the parent-child relationship, as illustrated in Fig. 5.3. In this process, the overlapping nodes play a crucial role.

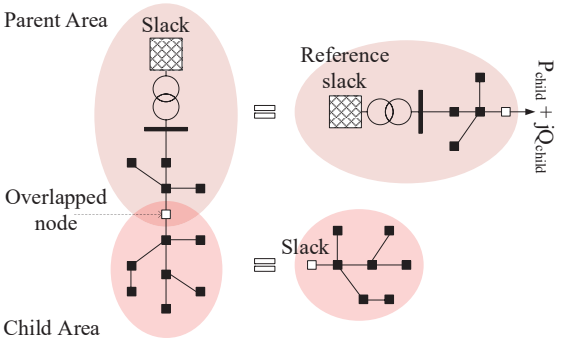

FIGURE 5.3: Grid Decomposition at Overlapping Node

In this approach, the parent area encompasses the reference slack bus, which is connected to the HV/MV substation for the MV networks and the MV/LV substation for the LV grids, respectively. However, for the child areas, the overlapping nodes serve as local slack buses, acting as reference points for conducting local PF calculations. Upon decomposing the grid, it is essential to replace the equivalent load model of the child area within the parent area to ensure that the PF results in the parent area align with the results of the integrated grid. To achieve this, the average values of active and reactive PFs of the connecting branches from the child area to the parent area are considered as the equivalent load of the child zone, to be connected to the overlapping node in the parent area. PF calculations on the integrated system, conducted over a wide range of random operating conditions or using real PMU measurements at the overlapping nodes, are employed to calculate the equivalent power of the child areas. To generate training data for each area, the variation range of the variables for the child slack bus is set as three times the SD of the voltage magnitude and phase angle. The angles of the three phases of the child's slack bus are determined with respect to the angles of the parent

reference slack bus, assumed to be 0°, 120°, and −120°. Providing the training data sets, three ANN-based estimators are trained to estimate the system states for each phase in each sub-area.

(b) **SE Phase**: upon receiving synchrophasor measurements from PMUs, all the ANN-based estimators dedicated to the divided zones calculate the system states in parallel. It's important to note that the dedicated estimators in each area receive measurements from the installed PMUs in the associated area. In this context, the states of the overlapping nodes are simultaneously calculated by the adjacent areas. The number of provided estimated variables at a specific overlapping node equals the number of zones that include the overlapping node. Therefore, one of those estimations should represent the states of this node. To achieve this, the most accurate estimations calculated by the involved zonal ANN-based estimator are selected. For the test dataset, in offline mode, the uncertainty of the estimated states of the overlapping nodes from the estimators of neighboring areas is calculated and compared after the training process. The estimator with the best accuracy is chosen to provide the overlapping node states. Despite estimating sufficiently accurate states by the local estimators, the accuracy of the estimated voltage profile is enhanced by substituting the real PMU measurements in the estimator input set with the corresponding estimates of the overlapping nodes obtained from the most accurate local estimator. The state estimation of the overlapping nodes is more accurate than the corresponding measured values when enough synchrophasor measurements are available. The propagation of measurement uncertainty through layers of the ANN is evaluated based on Monte Carlo simulation. This approach is chosen as the propagation is intractable due to the nonlinearities of the ANN in the proposed SE method. This fact has been validated in [123]. In Section 5.4, the results demonstrate that providing the magnitude and phase angle of the measured voltage phasor (as the inputs) gives more accurate estimates of the measured variables. Using these "more accurate" estimates of the overlapping nodes instead of the measured values in the other neighboring local estimators improves the SE accuracy in those neighboring sub-areas. In summary, Algorithm 2 shown in Fig. 5.4 outlines that the proposed MASE method is based on a two-step state estimation scheme. The states are estimated from the local estimators in parallel in the first step. In the second step, the estimations from the most accurate zonal estimator are substituted with the corresponding measurements in the other local neighboring estimators, improving the accuracy of SEs in those areas.

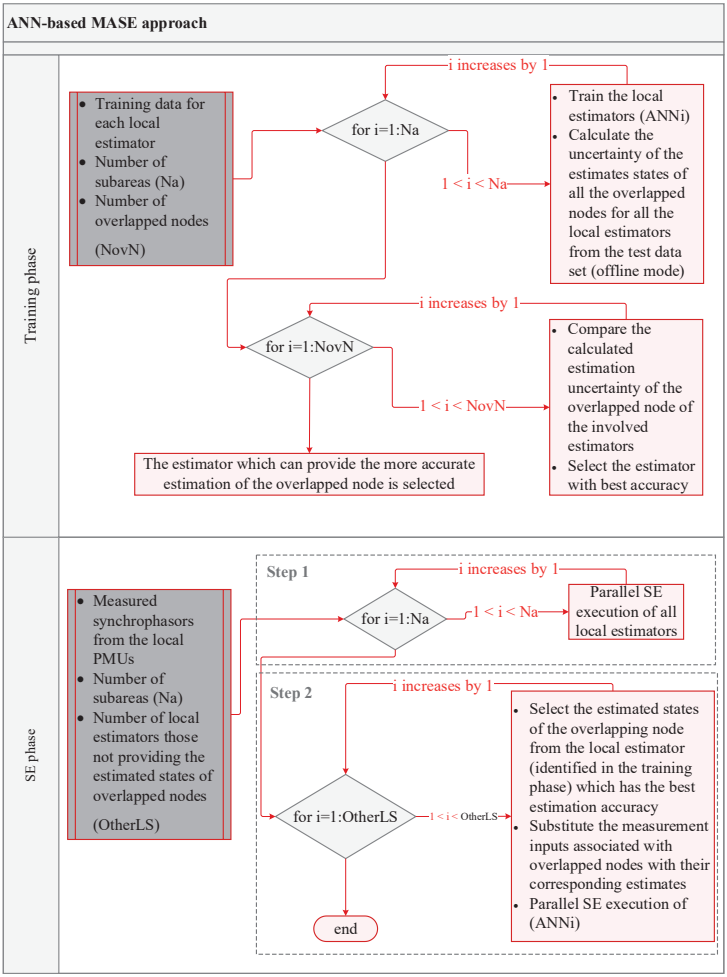

FIGURE 5.4: Algorithm 2 (Proposed MASE Method)

5.4 Results

In this subsection, the proposed distributed computation approaches are evaluated on the integrated IEEE 123 distribution benchmark system described in Subsection 3.9 in Chapter 3. The network under consideration is divided into four sub-areas, with an attempt to involve similar numbers of nodes in each zone for both architectures, as

explained in the following sections. The selected installation points for PMUs are nodes 149, 18, and 67.

1. **ANN-Based State Estimation in Parallel Architecture**

   In this distributed method, the IEEE 123 integrated system (depicted in Fig. 3.12) is divided into Zone A, Zone B, Zone C, and Zone D, as illustrated in Fig. 5.5. The entire training data for the IEEE 123 network is accordingly divided into four data packages, each containing the training data for these smaller portions of the grid. PMUs are located in Zone A, Zone B, and Zone D. The PF calculations associated with synchrophasor measurements from these PMUs serve as input training data for dedicated ANN-based estimators in each zone. Considering the presence of non-Gaussian noises, the SD of the error of the three-phase state estimates for all nodes is aggregated for both the integrated and parallel methods, represented in red and black colors, respectively, in Fig. 5.6.

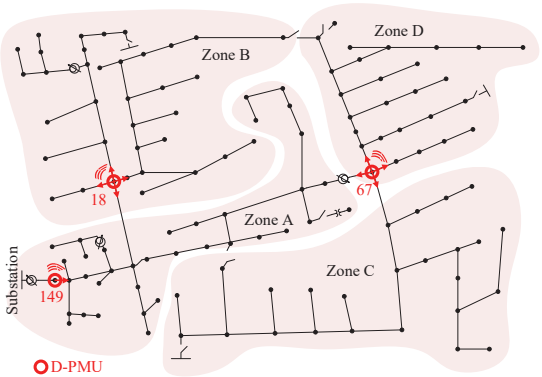

FIGURE 5.5: Zones in the Parallel Architecture

As evident, overall, the accuracy of the SE in the parallel approach surpasses the results calculated by the estimators trained for the integrated grid. This improvement can be attributed to the fact that the measured values of the entire system are mapped to the state of fewer nodes by the estimator dedicated to each zone. Consequently, the training algorithm has greater flexibility to adjust the weights and biases more effectively. The variation in nodes' estimation uncertainty can be discussed based on the electrical distance of each zone with respect to the slack bus and taking into account the locations of the PMUs.

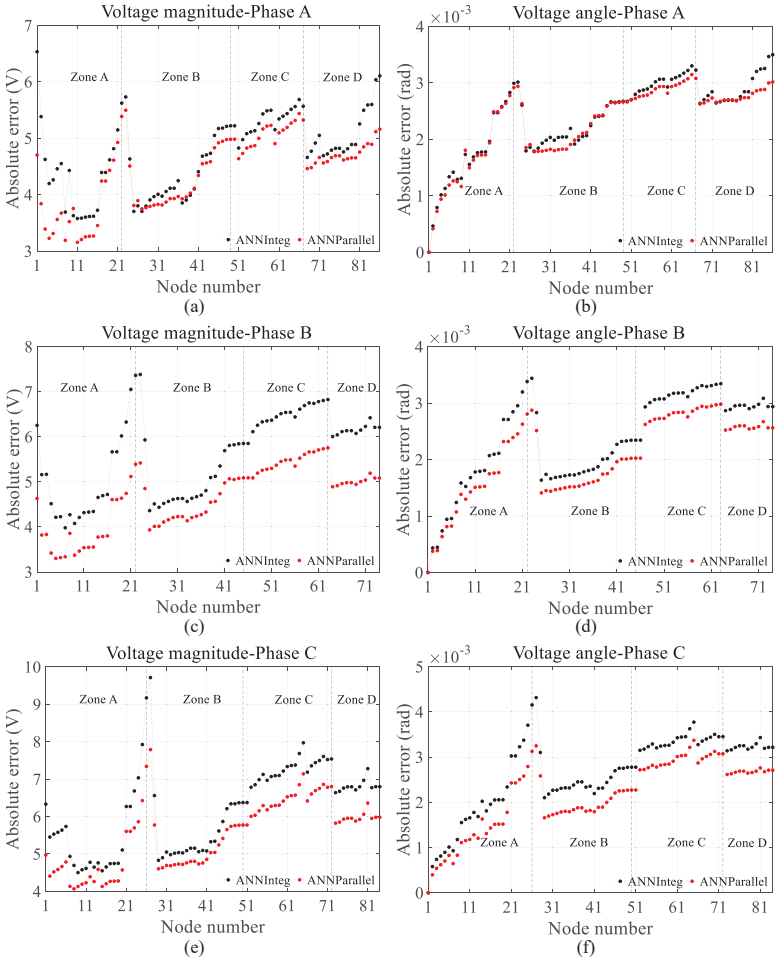

FIGURE 5.6: Uncertainty of the Estimated States of the Integrated System and the Parallel Approach.

To induce the maximum voltage drop, the network is operated radially. Moving from the substation toward the end of the radial feeder, the voltage variation generally increases per node in radial grids. Due to this radial operation, the voltage variation for nodes located closer to the slack bus is less than for nodes located farther from this bus. Consequently, the weights and biases of the ANN-based estimators are better tuned for nodes closer to the slack bus. Based on the results

shown in Fig. 5.6, the estimation uncertainty generally increases from Zone A to Zone D. Compared to the other zones, the estimation accuracy is less precise in Zone C. This is attributed to the fact that Zone C is not only far away from the slack bus, but its behavior is primarily captured from a few measurements by the PMU installed at node 67, as the locations of the other PMUs are distant from Zone C. Among the trained estimators for the divided areas, the estimation results obtained in sub-area B are more accurate than the other zones. This is because Zone B is not only close to the slack bus but also benefits from the proximity of the PMUs located at nodes 149 and 18. Node 67 serves as the connection point for Zone D, linked via a branch to both Zone A and Zone C. Similar to Zone C, Zone D is located far from the slack bus. However, as a PMU monitors the state of node 67, more synchrophasor measurements from this point can effectively represent the behavior of Zone D. Therefore, the estimation uncertainty of Zone D is lower than that of Zone C but still larger than Zone B. It is noteworthy that all the phases exhibit the same trend, as depicted in Fig. 5.6.

2. **ANN-Based State Estimation in Multi-Area Architecture**

According to the described parent-child scheme and considering the overlapping buses where the PMU existence is necessary, the IEEE 123 integrated network is divided into four sub-areas shown in Fig. 5.7. Zone A is the parent area, and the other zones are the children. To generate the training data, three-phase PF calculations are independently performed for each zone. The input training data include the voltage magnitude and voltage phase angle of the PMU installation point (only the overlapping node in this case), along with the current magnitude and current phase angles of the connected branches to this point. The input phasors corresponding to each zone are represented as follows:

- **Input training data set for Zone A:**
  [V_{149}**,** V_{18}**,** V_{67}**,** I_{149-1}**,** I_{13-18}**,** I_{60-67}**].**
- **Input training data set for Zone B:**
  [V_{18}**,** I_{18-19}**,** I_{18-35}**,** I_{18-21}**].**
- **Input training data set for Zone C:**
  [V_{67}**,** I_{67-72}**].**
- **Input training data set for Zone D:**
  [V_{67}**,** I_{67-68}**,** I_{67-97}**].**

Node 18 is the decoupling point between zone A and zone B as shown in Fig. 5.7.

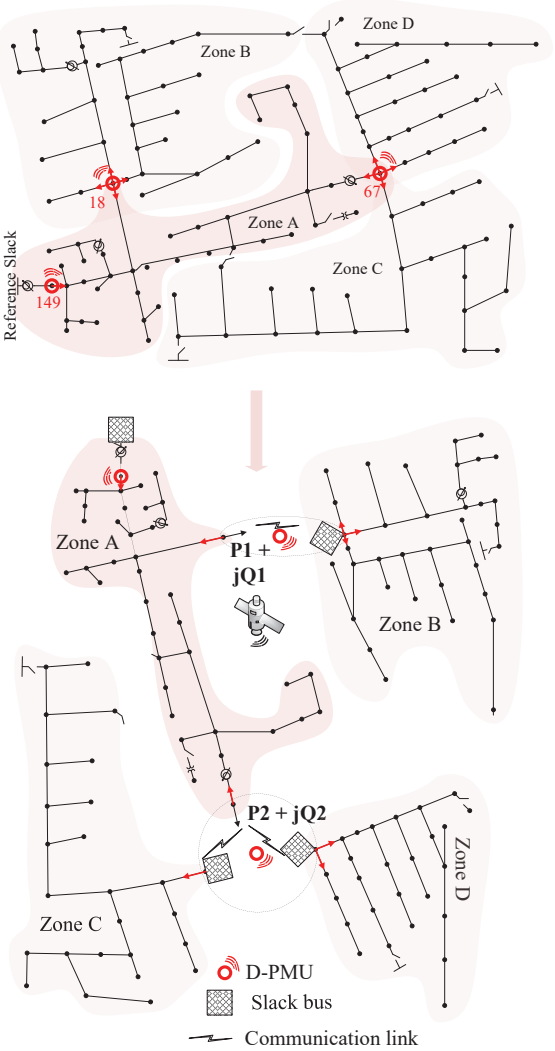

FIGURE 5.7: IEEE 123-Bus Test System Zones in the Multi-Area Architecture

The other two zones are decoupled at node 67. Since the decoupling nodes are the points of common coupling between the parent and child zones, these nodes are considered the connecting points of the equivalent load model of the child zones. In performing the PF calculations, these points play the role of slack buses for the

child zones. The variation of the voltage magnitude of the reference slack bus located in the parent area (Zone A) is around 1 pu. In this respect, a 1 % variation in the voltage on the high-voltage side is considered in this work. Subsection 5.3, however, describes that the applied voltage variation of the slack bus is obtained by the PF calculation of the integrated system or from real PMU measurements. To this end, in this dissertation, the voltage of the overlapping nodes is calculated by the PF calculations on the integrated system over a wide range of random scenarios (10,000 Monte Carlo simulations) in which the active and reactive powers were randomly varied based on a Gaussian distribution with (3 SD = 100%). The variation range of the variables of the child slack buses is then set as three times the SD of the calculated voltage magnitude and phase angle. Providing the training datasets, the ANN-based estimators are trained for each zone. To determine which estimator should provide the state estimation of the overlapping nodes in the state estimation phase in the proposed MASE approach, the estimation uncertainty of the local estimators is compared in the offline mode via a test dataset. Estimation uncertainty of the local estimators in the presence of Gaussian and non-Gaussian noises is tabulated in Tables 5.1 and 5.2, respectively.

Overlapped Node	Node 18		Node 67		
Zone	A	B	A	C	D
SD (Vmag PE (%))	0.31	0.33	0.29	0.33	0.33
SD (Vang PE (*crad*))	0.20	0.31	0.29	0.33	0.33

TABLE 5.1: Estimation uncertainty of the local estimator for the overlapped nodes in the presence of Gaussian noise

Overlapped Node	Node 18		Node 67		
Zone	A	B	A	C	D
SD (Vmag PE (%))	0.24	0.25	0.22	0.25	0.24
SD (Vang PE (*crad*))	0.16	0.22	0.21	0.23	0.23

TABLE 5.2: Estimation uncertainty of the local estimator for the overlapped nodes in the presence of non-Gaussian noise

It has been observed that the local estimator of Zone A can provide more accurate estimations for the overlapping nodes in Phase A (similar outcomes have been observed for the other two phases). Therefore, this estimator is selected to provide the overlapping node state estimation for the proposed two-step MASE method. Upon receiving the synchrophasor measurements, the local ANN-based estimators calculate the local estimations in parallel in the first step, as shown in black in Fig. 5.8. In the next step, the synchrophasor measurements of nodes 18 and 67

are replaced, in the input sets of the local estimators of Zones B–D, by their corresponding estimations estimated by the dedicated estimator for the parent area.

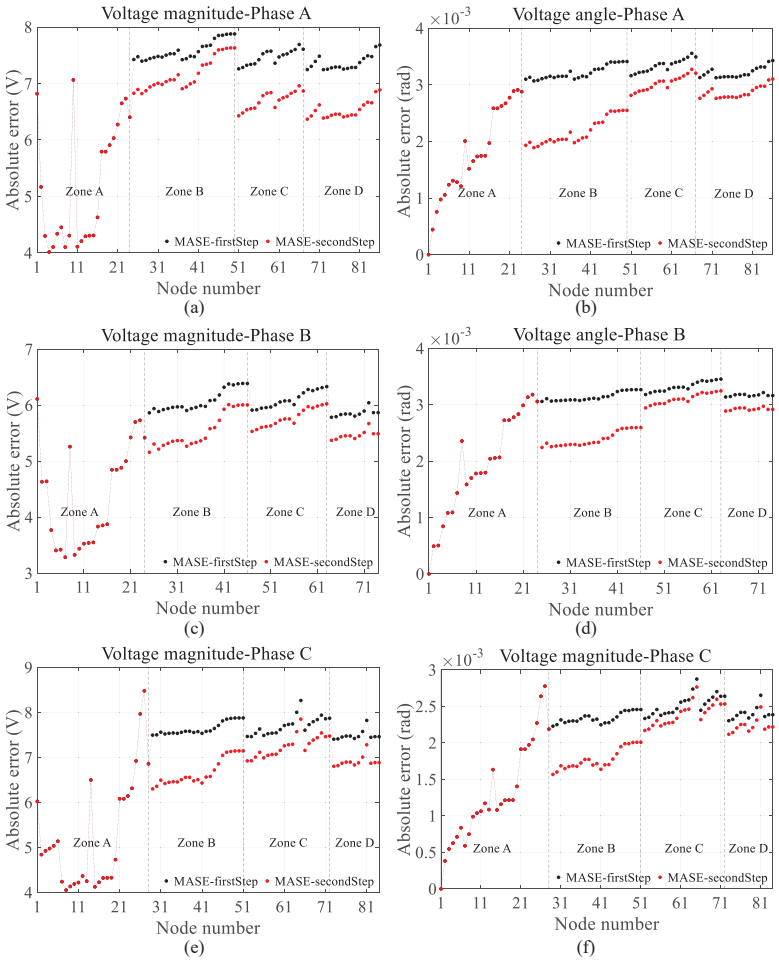

FIGURE 5.8: IEEE 123-Bus Test System Zones in the Multi-Area Architecture

Due to the low amount of data (state estimations of the overlapping node) communicated among the neighboring zones, the cost of the required communication infrastructure is low in this architecture. It should be noted that the estimation accuracy of the parent's estimator is better than the PMU measurements. As a result,

more accurate estimations are obtained for Zones B–D in the second step of SE, as shown in red in Fig. 5.8. In this context, according to [124], the estimation accuracy of the ANN-based estimator is equivalent to or better than its inputs when it takes inputs corrupted by Gaussian noise while training to recover the original undistorted inputs. To quantify this fact in accordance with the proposed ANN-based estimator, the trained local ANN-based estimators are executed for 10,000 random scenarios based on the following inputs:

- **Set 1**: δ_{67}
- **Set 2**: V_{67}
- **Set 3**: V_{67}, δ_{67}
- **Set 4**: Input training data set for zone D

Gaussian errors with 3 SD = 1% and 3 SD = 1 *crad* are added to the true values (PF calculated values) of the voltage magnitudes and phase angles, respectively, to model the uncertainty of the synchrophasor measurements. Table 3.3 indicates the uncertainty of PMU measurements and their corresponding estimations of node 67 in terms of standard deviation percentage error (PE) and the average error (AE) for voltage magnitude and the phase angle, respectively. The tabulated results for the input Set 1 indicate that the uncertainty of the voltage magnitude estimation is greater than the measurement uncertainty of the voltage angle of node 67. The vice versa situation is seen for the input Set 2.

Input Set	Node 67			
	PMU 67		Estimation	
	V_{mag} PE (%)	V_{ang} AE (crad)	V_{mag} PE (%)	V_{ang} AE (crad)
1	-	0.33	0.47	0.30
2	0.33	-	0.31	0.39
3	0.34	0.33	0.34	0.30
4	0.33	0.33	0.33	0.31

TABLE 5.3: Uncertainty of Measurement (Corrupted by Gaussian Noise) and Estimation of Node 67

It should be noted that the first two sets are considered here only to demonstrate how the ANN propagates the uncertainty of the measurements into the estimated

states. In the real case, however, the provided synchrophasor measurements include both voltage magnitude and voltage angle. Therefore, the minimum number of measured variables is two in input Set 3 and Set 4, compared to one measurement in the first two input sets. Thus, exploiting the voltage magnitude and the voltage phase angle measurements in the training process results in estimation accuracy better than that of the measured values, as shown for the last two input sets in Table 5.3. The same outcome has been observed when the measurements are affected by non-Gaussian noises. For instance, the mean square error (MSE) of the measurement and estimation is provided in Table 5.4. In this case, the MSE is chosen as an indicator for the accuracy assessment since the distribution of noise on the measurements is non-Gaussian.

Input Set	Node 67			
	PMU 67		Estimation	
	V_{mag} Error (V)	V_{ang} Error (crad)	V_{mag} Error (V)	V_{ang} Error (crad)
4	29.0191	5.8655e-04	23.1393	4.5550e-04

TABLE 5.4: Uncertainty of Measurement (Corrupted by non-Gaussian Noise) and Estimation of Node 67

Therefore, the estimation accuracy of the voltage profile in the proposed data-driven ANN-based MASE is enhanced by performing the second step SE. Although the estimation results are comparable with proposed WLS-based solutions in [119], [122], and [105], the computational cost of the ANN-based estimator is lower.

5.5 Conclusion

To enable the execution of the proposed ANN-based estimation technique within a distributed computation framework, this chapter discusses both a parallel and a multi-area architecture. In both architectures, a large distribution grid is divided into smaller subareas, with each divided area containing a possibly similar number of nodes. In the parallel architecture, dedicated ANN-based estimators for each divided zone map synchrophasor measurements from all the installed PMUs in the integrated network into the states of the nodes in each zone. Consequently, the training algorithm has more degrees of freedom to better tune a fewer number of weights and biases compared to the case where the ANN is trained to provide state estimations for the entire integrated grid. As a result, more accurate estimations are obtained in the parallel architecture. In cases where performing PF calculations is heavy or it is desired to monitor only specific

subareas, PF calculations and state estimation are independently executed based on the proposed multi-area approach. In this approach, the grid is split based on the parent-child relationship at decoupling nodes where PMUs are available. The parent area consists of the reference slack bus (main substation), and the equivalent load model of the child area is connected to the parent area at the decoupling points after grid decomposition. Nevertheless, the decoupling points are utilized as slack buses for the child areas. The training data is then produced by PF calculations specific to each area. After the training process, a two-step state estimation is performed. In the first step, the local estimators estimate the system states in each zone. Then, the accuracy of the estimation is enhanced in the second step by substituting the overlapping node measurements with their corresponding estimations calculated by the most accurate estimator.

Chapter 6

Linear Iterative Current Injection Power Flow Method

In this chapter, a new fast PF approach tailored for distribution system studies has been introduced. The core of this method relies on a fixed-point iteration solver, incorporating a linearized current injection model of P-Q and P-V nodes. Notably, the applied P-Q node model in this method is voltage-dependent, considering voltage variations in distribution grids. While traditional distribution grids typically have few or no voltage control components, the controllability of power converters has opened the possibility to operate certain distributed energy resources, such as battery storage systems, as voltage controllers or P-V nodes in active distribution grids. In line with this, a linear model of the P-V node based on the current injection concept has been developed in this dissertation. Beyond the various applications of PF in the planning, operation, automation, and control of power systems, the primary objective of utilizing the proposed PF method in this dissertation is to rapidly generate training data for the proposed data-driven monitoring system.

6.1 Introduction

To ensure efficient operation of power systems within their operating limits, system operators conduct PF studies, examining the impact of power flowing through network branches from generation units to customers. PF studies have diverse applications in planning, automation, and operation of power systems. The role of PF in planning and operating distribution grids is discussed in [125], emphasizing its use in evaluating network behavior and managing alternatives based on voltage regulation, power factor targets, and generation constraints. From an automation perspective, PF is utilized for monitoring distribution grids, as demonstrated in [126–128]. Traditional PF methods, such as Gauss-Seidel and Newton-based approaches, designed for transmission grids

[129], may not be optimal for distribution systems due to different network characteristics, as pointed out in Section 2.3. Common solutions for distribution systems include the backward-forward sweep [130, 131] and the current injection method (CIM) [132]. However, these solutions encounter convergence issues in the presence of more than one voltage-controlled node (or P-V node). Moreover, conventional PF approaches for distribution systems have a high computational burden [133], making them unsuitable for fast real-time automation and operation functions. To address these challenges, research has focused on increasing the convergence rate of nonlinear PF methods, linearizing the PF problem, and leveraging data-driven techniques for faster solutions [134–136]. Linearization is a common approach to simplify and accelerate PF calculations. A classical direct-current (DC) PF method is described in [137], mainly used for MW-oriented applications where the effects of network voltage and VAR conditions are minimal. However, this approach cannot be applied in distribution systems due to comparable resistive and reactive parts of line impedances [138, 139]. In comparison, the DC PF approach proposed in [140] considers the exact effect of net reactive loads on phase angles and has acceptable accuracy even under cold-start conditions. However, it faces the drawback that voltage magnitude and phase angle are not completely decoupled, leading to a quadratic programming (QP) problem if used for optimization. Addressing this issue, a decoupled linearized power flow (DLPF) model with respect to voltage magnitude and phase angle is introduced in [141], assuming uniform resistance-to-reactance ratios and a radial network. A sparse linear approximation of feasible power flows is derived in [142] based on a geometric approach, suitable for unbalanced three-phase power systems. Another linear balanced PF model is proposed in [143] for radial distribution systems, neglecting the load voltage-dependent characteristic. Considering small voltage drops along branches and an operating voltage magnitude around 1 pu, [144] proposes a linear expression-based PF solution. However, this approach does not consider PV buses and ZIP load. In [138], a linear power flow approach is introduced for distribution systems, incorporating the ZIP load model but not considering P-V nodes. In distribution grids, the voltage-dependent characteristic of the load is addressed in a novel linear non-iterative PF formulation based on the ZI load type, as presented in [145]. This method utilizes the curve-fitting technique to derive the load model, a technique also adopted in the PF approach proposed in this chapter. While [145] employs the P-Q model (negative load) for modeling DG units, the proposed approach in [146] lacks coverage of DGs as voltage regulators (voltage-controlled nodes). To address this limitation, this chapter focuses on a PF formulation based on the fixed-point iteration technique (described in Section 6.2). It integrates a proposed linear model of the synchronous generator (explained in Section 6.3), representing it as a P-V node (the bus where the voltage is controlled either by synchronous generators or by grid-forming

converters [147]). Additionally, it incorporates the linear ZI load model derived in [145] (explained in Section 6.4). To facilitate this integration, the power angle of the generator is relaxed using the relaxation method and a relaxation factor. From the perspective of distribution system imbalances, three-phase linear PF approaches have been introduced in [148] and [149]. The proposed linearized model of the synchronous generator in this dissertation can also be applied in [139], which represents the three-phase extension of the balanced PF formulation proposed in [145]. The computational complexity of the proposed method is compared with the Newton-Raphson PF technique in Section 6.5. Finally, the performance of the proposed linear PF approach is assessed in the results, Section 6.6.

6.2 Fixed-Point PF Solver

The system of linear equations (SLE) in (6.1) is obtained by applying Kirchhoff's Current Law to a power system consisting of n nodes, along with the equivalent current injection model of sink and source components.

$$Yv = i(v) \tag{6.1}$$

Given the admittance matrix $Y \in \mathbb{C}^{n\times n}$ and the current injection vector $i \in \mathbb{C}^n$ (which includes the load and generator equivalent current injection models within the framework of this dissertation), the vector of node voltages $v \in \mathbb{C}^n$ is determined by solving the system of linear equations in (6.1). To achieve this, the dissertation employs the general fixed-point iteration (FPI) solver described in **Algorithm 1**. This solver is faster than the Newton and Dishonest Newton methods [150]. The rate of convergence for this problem is significantly improved in the proposed PF solution due to the integration of the linear current injection model of P-Q and P-V nodes, as demonstrated in Section 6.5. A hybrid solution is observed in terms of the required number of iterations. On one

Algorithm 1: CIM Using Fixed-Point Iteration

Data: Network parameters and load data
Result: Voltage magnitude and voltage phase angle
$k = 0$;
while $E \geq \varepsilon$ **do**
  update current injections $i(v)$;
  solve $Yv = i(v)$;
  $E = \left\| v_{k+1} - v_k \right\|$;
  $k \leftarrow k + 1$;
end

hand, the system, including only P-Q nodes, converges without any iteration. On the other hand, iteration is necessary when a P-V node is present in the system. As illustrated in Fig. 6.1, the equivalent current injection model of nodes and the node voltages are updated during the iteration process, while the admittance matrix remains constant. The independence of all these current elements allows them to be executed in parallel

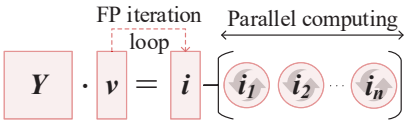

FIGURE 6.1: Parallel Computing of Current Injections

using a high-performance multi-core computer. This is a key advantage of the proposed PF formulation over other existing PF methods. The iteration process concludes when the difference between two consecutive results, calculated by the SLE in (6.1), meets the predefined tolerance (ϵ). The initial guess for the system's bus voltages is taken from the unloaded grid condition. However, the previous solution serves as a more accurate initial guess for solving the next problem. Generally, a closer initial voltage guess to the final solution enhances the rate of convergence.

6.3 P-V Node Current Injection Model

In the context of PF calculation, net real power and voltage magnitude are regulated at P-V nodes through synchronous generators and grid-forming converters, serving as conventional and modern voltage regulators, respectively. To integrate the current injection model of this node into the proposed FPI power flow approach, the equivalent current injection model of the rotating synchronous generator is derived in this dissertation under the assumption that the resistance of the armature winding is neglected. In this regard, the correlation between net active power and voltage magnitude of the synchronous generator is expressed as [151]:

$$p_g = \frac{E.v_g}{x_g} \sin(\delta) \tag{6.2}$$

where

E: Electromotive force (emf) (i.e. the internal voltage of the machine)

x_g: Generator's synchronous reactance

v_g: Terminal voltage of the generator

δ: Power angle, the angle between the terminal voltage and the generator emf

The Thévenin equivalent circuit model of the synchronous generator along with its phasor diagram is shown in Fig. 6.2. In performing the proposed PF calculation, the gener-

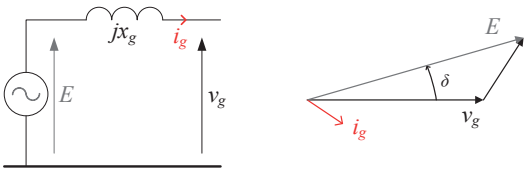

FIGURE 6.2: Single-line and Phasor Diagram of Synchronous Generator

ator reference operating settings (E_{ref}, P_{ref}) are adjusted to the P-V node target values (P_{target}, V_{target}); $E_{ref} = V_{target}$ and $P_{ref} = P_{target}$. Consequently, the generator injected current i_g needs to be adjusted to meet these targets. As per the phasor diagram depicted in Fig. 6.2, the machine emf is expressed as:

$$E = E_{ref} \exp\left(j(\delta + \angle v_g)\right) \tag{6.3}$$

Given that the magnitude of E is set to be E_{ref}, the power angle and the terminal voltage of the generator are the only variables changing the emf during the PF iteration process so that the generator equivalent current injection i_g can meet the P_{ref}. In this manner, the changing rate (per iteration) of the power angle is calculated using a linearized form of Equation 6.2, derived by applying the partial derivative rule as follows:

$$\Delta p_g = \underbrace{\frac{E.\Delta v_g}{x_g}\sin(\delta)}_{\text{Term 1}} + \underbrace{\frac{E.v_g}{x_g}\cos(\delta)}_{\text{Term 2}}.\Delta\delta \tag{6.4}$$

Then, the changing rate of the power angle is obtained based on the defined terms (Term 1 and Term 2) in the Equation 6.4:

$$\Delta\delta = \frac{\Delta p_g - \text{Term 1}}{\text{Term 2}} \tag{6.5}$$

Δp_g is the difference between of P_{ref} and the generator's active power (p_g):

$$\Delta p_g = P_{ref} - p_g \tag{6.6}$$

To align the generator with the reference power, the described FPI procedure aims to make this difference zero:

$$FPI\colon \Delta p_g \rightarrow 0 \tag{6.7}$$

While the linearized form of the generator active power is utilized to calculate the power difference in Equation 6.6 in this dissertation, the active power of the generator is updated by extracting the real part of the generator complex power (s_g), as follows:

$$s_g = p_g + jq_g = v_g.i_g^* = v_g.\Big(\frac{E - v_g}{jx_g}\Big)^* \tag{6.8}$$

$$p_g = Re\left(v_g.\Big(\frac{E - v_g}{jx_g}\Big)^*\right) \tag{6.9}$$

The multiplication of the generator terminal voltage (v_g) and its current injection conjugate (i_g^*) yields the generator complex power (s_g). Both of these variables vary so that the generator's active power meets the active power reference point (P_{ref}) during the FPI process. Considering the zero initial power angle value, the initial generator's active power would be zero. However, in the FPI process, the power angle is increased until the generator's active power reaches P_{ref}. In this iteration process, the generator terminal voltage is updated by solving, per iteration, the SLE in system of Equations 6.1. Simultaneously, the power angle varies based on the changing rate calculated in Equation 6.5. To achieve this, the power angle is relaxed through the applied relaxation factor (γ) as follows:

$$\delta \leftarrow \delta + \gamma.\Delta\delta \tag{6.10}$$

The relaxation method has been explained in **Appendix B**. The rate of change of the generator current injection and, consequently, the power flow rate of convergence are altered by γ. When $\gamma = 1$ (Gauss-Seidel method), it is the boundary between under-relaxation and over-relaxation. Under over-relaxation conditions $(\gamma > 1)$, the solution decays with oscillations, while under under-relaxation conditions $(\gamma < 1)$, there are no oscillations. The relaxation factor serves as a convergence-controlling parameter, determining whether the system reaches the solution with oscillations or not. Selecting the right value for the relaxation factor minimizes the number of iterations required to reach the solution. In this respect, Monte Carlo simulation based on random operating conditions is taken into account to obtain the optimum value for the relaxation factor in this dissertation, as shown in Section 6.6. During this process, while the number of required iterations satisfying the solutions is counted, γ varies in a range starting from under-relaxation mode and ending at a point in the over-relaxation mode for each

Monte Carlo trail. The γ resulting in the minimum number of required iterations represents the optimal relaxation factor.

6.4 P-Q Node Current Injection Model

The voltage-independent load model is conventionally used in load flow calculations. This type of load is suitable for performing the PF at the transmission levels where the voltage variation is limited, as TSOs regulate the voltage at most nodes. To integrate this model into the FPI technique, the load current injection model is derived from the load's complex power (s_l) and relaxed through the formulation in B.2 as follows:

$$s_l = p_l + jq_l = v_l.i_l^* \tag{6.11}$$

$$i_l \leftarrow (1-\gamma)i_l + \gamma.\Big(\frac{p_l + jq_l}{v_l}\Big)^* \tag{6.12}$$

Due to the absence of voltage control devices, the voltages can vary widely along the system feeders in distribution grids. To obtain more accurate system operating points, the load voltage-dependent characteristic should be taken into account in PF studies in these networks. A more accurate PF result can lead to cost reduction in delivering power to end customers, as there is no need for under or over-compensation for voltage regulation. In this context, the constant active and reactive power in 6.12 should be replaced with a load voltage-dependent equivalent characteristic, as follows:

$$i_l \leftarrow (1-\gamma)i_l + \gamma.\Big(\frac{p_l(v_l) + jq_l(v_l)}{v_l}\Big)^* \tag{6.13}$$

In this context, the load voltage dependency models are commonly expressed as:

- **Exponential Load Model**: the following exponential load model is one of the common ways of characterizing the voltage dependency of the active and reactive power [151]:

$$\frac{p_l(v_l)}{p_{l0}} = \Big(\frac{v_l}{v_{l0}}\Big)^{\alpha} \tag{6.14}$$

$$\frac{q_l(v_l)}{q_{l0}} = \Big(\frac{v_l}{v_{l0}}\Big)^{\beta} \tag{6.15}$$

  The nominal values are indicated by a zero subscript in these representations. The load exponents α and β are determined from the load-measured data.

- **ZIP Load Model**: another common way for load voltage dependency representation is the polynomial model [151]. This model takes part three elements:

1. a constant-impedance (Z)
2. a constant-current (I)
3. a constant-power (P)

This model is formulated here:

$$\frac{p_l(v_l)}{p_{l0}} = F_Z.\left(\frac{v_l}{v_{l0}}\right)^2 + F_I.\left(\frac{v_l}{v_{l0}}\right) + F_P \tag{6.16}$$

$$\frac{q_l(v_l)}{q_{l0}} = F_Z^{'}.\left(\frac{v_l}{v_{l0}}\right)^2 + F_I^{'}.\left(\frac{v_l}{v_{l0}}\right) + F_P^{'} \tag{6.17}$$

The constant coefficients F and $F^{'}$ are extracted from the measurements and the subscripts Z, I, and P corresponded to the mentioned ZIP elements. There are only two independent parameters in formulas 6.16 and 6.17 since $F_Z + F_I + F_P = 1$ and $F_Z^{'} + F_I^{'} + F_P^{'} = 1$.

- **ZI Load Model**: this model has been introduced in [145] and is a kind of modification of the ZIP polynomial load model in which the vertical intercept is assumed to be zero:

$$\frac{p_l(v_l)}{p_{l0}} = C_Z.\left(\frac{v_l}{v_{l0}}\right)^2 + C_I.\left(\frac{v_l}{v_{l0}}\right) \tag{6.18}$$

$$\frac{q_l(v_l)}{q_{l0}} = C_Z^{'}.\left(\frac{v_l}{v_{l0}}\right)^2 + C_I^{'}.\left(\frac{v_l}{v_{l0}}\right) \tag{6.19}$$

Compared to the ZIP load model, the number of load-independent parameters decreases by one ($C_Z + C_I = 1$ and $C_Z^{'} + C_I^{'} = 1$) in ZI load model while the accuracy of the PF results is not affected.

Utilizing the above-mentioned load models, the equivalent current injection model of 6.12 is updated at each iteration, ensuring that the PF problem converges to the correct states in distribution grids. Nevertheless, these load models introduce non-linearities on the right-hand side of the SLE in 6.1. Assuming that the imaginary part of the voltage

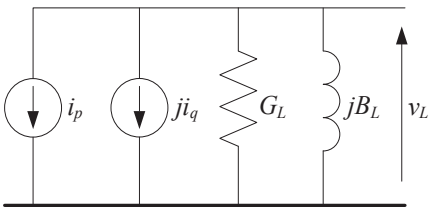

FIGURE 6.3: ZI Load Model

is much smaller than the real part by several orders of magnitude ($v_{\text{im}} \ll v_{\text{re}}$), a ZI load model is obtained. This model includes an impedance (Z) in parallel with a current source (I), as shown in Fig. 6.3. It converts the non-linear PF problem into a linear non-iterative one [145] when there are only P-Q nodes in the power network. To derive this linearized model, the active and reactive load components in the mentioned polynomial ZI load model are used in the load complex power.

$$i_l = \Big(\frac{p_l + jq_l}{v_l}\Big)^* = \tag{6.20}$$

$$\left(\frac{p_{l0}.\big(C_Z.(\frac{v_l}{v_{l0}})^2 + C_I.(\frac{v_l}{v_{l0}})\big) + jq_{l0}.\big(C_Z^{'}.(\frac{v_l}{v_{l0}})^2 + C_I^{'}.(\frac{v_l}{v_{l0}})\big)}{v_l}\right)^* =$$

$$\underbrace{\Big(\frac{p_{l0}C_Z v_{lre} + q_{l0}C_Z^{'} v_{lim}}{v_{l0}^2} + \frac{p_{l0}C_I v_{lre} + q_{l0}C_I^{'} v_{lim}}{v_{l0} v_l}\Big)}_{\Re\{i_l\}}$$

$$+$$

$$\underbrace{j\Big(\frac{p_{l0}C_Z v_{lim} - q_{l0}C_Z^{'} v_{lre}}{v_{l0}^2} + \frac{p_{l0}C_I v_{lim} - q_{l0}C_I^{'} v_{lre}}{v_{l0} v_l}\Big)}_{\Im\{i_l\}}$$

Considering $\frac{v_{lre}}{v_l} = \frac{v_{lre}}{\sqrt{v_{lre}^2 + v_{lim}^2}}$, $\frac{v_{lim}}{v_l} = \frac{v_{lre}}{\sqrt{v_{lre}^2 + v_{lim}^2}}$ and assuming that $v_{lim} \approx 0$, the above equation simplifies as:

$$i_{lre} = \Re\{i_l\} \approx \frac{q_{l0}C_Z^{'}}{v_{l0}^2} v_{lim} + \frac{p_{l0}C_Z}{v_{l0}^2} v_{lre} + \frac{p_{l0}C_I}{v_{l0}} \tag{6.21}$$

$$i_{lim} = \Im\{i_l\} \approx \frac{p_{l0}C_Z}{v_{l0}^2} v_{lim} - \frac{p_{l0}C_Z^{'}}{v_{l0}^2} v_{lre} - \frac{q_{l0}C_I^{'}}{v_{l0}} \tag{6.22}$$

Taking into account formula 6.21 and 6.22, a ZI load model is extracted as:

$$i_l = i_{lre} + j i_{lim} = \tag{6.23}$$

$$\Big(\frac{p_{l0}C_Z}{v_{l0}^2} v_{lre} - \frac{p_{l0}C_Z^{'}}{v_{l0}^2} v_{lim}\Big) + j\Big(\frac{q_{l0}C_Z^{'}}{v_{l0}^2} v_{lre} + \frac{p_{l0}C_Z}{v_{l0}^2} v_{lim}\Big) + \frac{p_{l0}C_I}{v_{l0}} - j\frac{q_{l0}C_I^{'}}{v_{l0}}$$

$$\Longrightarrow i_l = \Big(\frac{p_{l0}C_Z}{v_{l0}^2} - \frac{q_{l0}C_Z^{'}}{v_{l0}^2}\Big).(v_{lre} + j v_{lim}) + \Big(\frac{p_{l0}C_I}{v_{l0}} - j\frac{q_{l0}C_I^{'}}{v_{l0}}\Big)$$

$$\Longrightarrow i_l = \underbrace{\left(\frac{p_{l0}C_Z}{v_{l0}^2} - j\frac{q_{l0}C_Z^{'}}{v_{l0}^2}\right)}_{\underbrace{G_L + jB_L}_{Y_L}}.(v_l) + \underbrace{\left(\frac{p_{l0}C_I}{v_{l0}} - j\frac{q_{l0}C_I^{'}}{v_{l0}}\right)}_{\underbrace{i_p + ji_q}_{I_L}}$$

Therefore, the extracted load current is represented as an admittance (Y_L) in parallel with a current source (I_L), as shown in Fig 6.3. Considering P-V and Q-V characteristics based on the collected measured data, the load coefficients ($C_Z, C_I, C_Z^{'}$, and $C_I^{'}$) are calculated using the curve fitting technique [145]. This ZI load model is easily integrated into the SLE in 6.1. In this respect, the impedance of the loads and the load current sources are added to the admittance matrix diagonal elements and the current vector, respectively. Exploiting this ZI load model along with the proposed current injection model of a synchronous generator leads to a linear iterative PF formulation. According to the obtained results in Section 6.6, this PF method is accurate enough to be used in the operation of distribution grids. However, due to assumptions taken into account in the derivation of the ZI load model, it is shown that the calculated results cannot exactly match those obtained via non-linear PF (NLPF) methods. To compensate for this discrepancy, the following non-linear ZI load model based on the active and reactive powers in formulas 6.18 and 6.19 can be used in the proposed FPI PF method:

$$i_l \leftarrow (1-\gamma)i_l + \gamma.\left(\frac{p_l + jq_l}{v_l}\right)^* \tag{6.24}$$

$$= \left(\frac{p_{l0}.\left(C_Z.(\frac{v_l}{v_{l0}})^2 + C_I.(\frac{v_l}{v_{l0}})\right) + jq_{l0}.\left(C_Z^{'}.(\frac{v_l}{v_{l0}})^2 + C_I^{'}.(\frac{v_l}{v_{l0}})\right)}{v_l}\right)^*$$

$$i_l \leftarrow (1-\gamma)i_l + \gamma.\Bigg(\underbrace{\left(\frac{p_{l0}C_Z}{v_{l0}^2} - j\frac{q_{l0}C_Z^{'}}{v_{l0}^2}\right)}_{\text{Admittance Part}}.v_l + \underbrace{\left(\frac{p_{l0}C_I}{v_{l0}} - j\frac{q_{l0}C_I^{'}}{v_{l0}}\right)}_{\text{Current Part}}\Bigg)$$

When integrating this model into the SLE, the load voltage, and consequently, the load equivalent current injection are updated in each iteration so that the solver can meet the predefined tolerance (ϵ). The PF approach in this dissertation, however, utilizes the linear ZI load model and the proposed current injection model of the synchronous generator, representing the P-Q and the P-V nodes, respectively. The implementation of the proposed approach is shown in **Algorithm 2**.

Algorithm 2: Linear Iterative PF Algorithm

Data: Network parameters, Power flow data, Iteration, Tolerances (ϵ; ε), Power plant settings (E_{ref} ;p_{ref}), Relaxation factor (γ), Load Fitting coefficients (C_z; C'_z; C_I and C'_I)

Result: Voltage magnitude and voltage phase angle

Per Unit Values Conversion;

Building Admittance Matrix (including the equivalent load impedance defined in (6.23)):Y;

Calculate Impedance Matrix: $Z = Y^{-1}$;

initialization: $v = v_0$;

$k = 0$;

while $E \geq \varepsilon$ **do**

Update generators current injection model ig :

$i_g^{k*} = \left(\frac{E^k - v_g^k}{jx_g}\right)^*$;

$p_g^k = Re(v_g^k.i_g^{k*})$;

$\Delta p_g^k = p_{ref} - p_g^k$;

$t_1^k = \frac{E^k.(v_g^k - v_g^{k-1})}{x_g}$;

$t_2^k = \frac{E^k.v_g^k}{x_g}\cos(\delta^k)$;

$\Delta\delta^k = \frac{p_g^k - t_1^k}{t_2^k}$;

if $t_2 > \epsilon$ **then**

$\delta^{k+1} = \delta^k + \gamma\Delta\delta^k$;

end

$E^{k+1} = E_{ref}\exp\left(j(\delta^{k+1} + v_g^k)\right)$;

Solve $v = Z.i(v)$ for v_{k+1};

$e = \left\|v_{k+1} - v_k\right\|_2$;

$k \leftarrow k + 1$;

end

6.5 Computational Burden Assessment

To demonstrate the computational efficiency of the proposed linear iterative PF technique compared to classical PF methods, the computational burden of the proposed FPI approach is compared with the Newton-Raphson method in this section. This comparison is based on a rough estimation of the FLOPs for the main required mathematical operation functions and the solution convergence rate.

- **FLOPs**

  The computational burden of the PF problem is directly related to the number of mathematical operations executed in the PF algorithms. In this context, the number of FLOPs used in the proposed FPI and the classical Newton-Raphson method is compared here. To understand the general picture of PF algorithms, the systems of equations for both approaches are represented here:

  1. **Newton-Raphson Solution**

     Equation 6.25 shows how the voltage solutions are updated by the multiplication of the Jacobian matrix inverse and the power mismatch formulation.

$$\Delta v^k = -[J^k]^{-1} \times \begin{bmatrix} \Delta P(v^k) \\ \Delta Q(v^k) \end{bmatrix} \tag{6.25}$$

     The dimensions of the Jacobian matrix along with its elements (submatrices) are indicated here:

$$\overbrace{[J^k]}^{(2N-2-M)\times(2N-2-M)} = \begin{bmatrix} \overbrace{[J^k_{P\theta}]}^{(N-1)\times(N-1)} & \overbrace{[J^k_{PV}]}^{(N-1)\times(N-M)} \\ \overbrace{[J^k_{Q\theta}]}^{(N-M)\times(N-1)} & \overbrace{[J^k_{QV}]}^{(N-M)\times(N-M)} \end{bmatrix} \tag{6.26}$$

     N and M are the number of buses and the number of P-V nodes in the grid, respectively. The submatrices and the power mismatch formulation are found in the **Appendix C**.

  2. **Proposed Linear Iterative PF Solution**

     The voltage solution for the proposed linear iterative solution is updated based on formula 6.27:

$$\Delta v^k = \overbrace{[Z]}^{N\times N} \times \begin{bmatrix} i^k_g(v) \\ i_l \end{bmatrix} \tag{6.27}$$

To assess the computational burden of the proposed linear iterative PF method in comparison to the classical Newton-Raphson approach, the number of FLOPs in formula 6.25, representing the Newton-Raphson method, should be compared with the number of FLOPs in formula 6.27 for the proposed method. The main adverse impact on the execution time of equation 6.25 comes from the Jacobian matrix inversion function and the multiplication of this matrix with the power mismatches. For the sake of simplicity, the FLOPs for mathematical operators

altogether used in the Jacobian matrix and the power mismatch matrices are neglected, as this number is significantly larger than the FLOPs corresponding to the operators used in the current injection matrix in formula 6.27. Considering a square matrix with a size of $(N \times N)$, the computational complexity in terms of the required number of FLOPs is cubically $\mathcal{O}(N^3)$ and quadratically $\mathcal{O}(N^2)$ dependent on the size of this matrix when executing the matrix inversion and matrix multiplication functions, respectively [152, 153]. In this respect, Fig. 6.4 shows the executed MATLAB computational time for inverting square matrices where the size increases from 1×1 to 5000×5000; along with the required computational time for their multiplication with columns whose size increases from 1×1 to 5000×1.

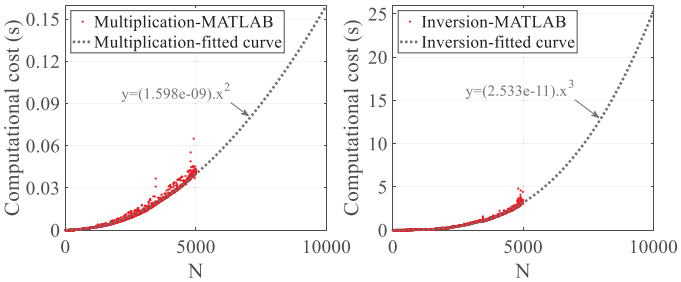

FIGURE 6.4: Computational Cost of Matrix Inversion and Multiplication

The matrix elements have been randomly selected. As the inversion task is heavy for large matrices (and consequently time-consuming), this operation has ended when the matrix size reaches 5000×5000. However, the matrix inversion and multiplication execution times for matrices with sizes between 5000×5000 and 10000×10000 have been estimated using the MATLAB curve fitting tool. To check the effectiveness of this estimation, a matrix with a size of 9000×9000 has been inverted. The elapsed time for inverting this matrix is around 23 seconds, which is compatible with the shown inversion-fitted curve. However, the impedance matrix (Z) is constant in the proposed PF method. Then, taking into account equations 6.25 and 6.27, the proposed PF solution does not involve the time-consuming calculations of the Jacobian matrix elements and the matrix inversion, with $\mathcal{O}\big((2N-2-M)^3\big)$ complexity, in each iteration as in the Newton-Raphson algorithm. In terms of the matrix multiplication operation, moreover, the Newton-Raphson and the proposed solutions have $\mathcal{O}\big((2N-2-M)^2\big)$ and $\mathcal{O}(MN)$ complexities per iteration, respectively, when there are M P-V nodes in

the system. The $\mathcal{O}(MN)$ complexity is obtained based on the following two scenarios:

1. **Grid Consisting of Only P-Q Nodes**

   As already mentioned, no iteration is required to solve the problem in this case. In this context, the equivalent constant values of the load impedance and load current injection model are integrated into the SLE of 6.28:

$$\begin{bmatrix} Z_{11} & Z_{12} & \cdots & Z_{1N} \\ Z_{21} & Z_{22} & \cdots & Z_{2N} \\ Z_{31} & Z_{32} & \cdots & Z_{3N} \\ \vdots & \vdots & \ddots & \vdots \\ Z_{N1} & Z_{N2} & \cdots & Z_{NN} \end{bmatrix} \times \begin{bmatrix} i_{L1} \\ i_{L2} \\ i_{L3} \\ i_{L4} \\ \vdots \\ i_{LN} \end{bmatrix} = \begin{bmatrix} v_1 \\ v_2 \\ v_3 \\ v_4 \\ \vdots \\ v_N \end{bmatrix} \tag{6.28}$$

$$\Longrightarrow \begin{pmatrix} v_1 = \underbrace{Z_{11}i_{L1} + Z_{12}i_{L2} + Z_{13}i_{L3} + \cdots + Z_{1N}i_{LN}}_{V_1} \\ v_2 = \underbrace{Z_{21}i_{L1} + Z_{22}i_{L2} + Z_{23}i_{L3} + \cdots + Z_{2N}i_{LN}}_{V_2} \\ v_3 = \underbrace{Z_{31}i_{L1} + Z_{32}i_{L2} + Z_{33}i_{L3} + \cdots + Z_{3N}i_{LN}}_{V_3} \\ \vdots \\ v_N = \underbrace{Z_{N1}i_{L1} + Z_{N2}i_{L2} + Z_{N3}i_{L3} + \cdots + Z_{NN}i_{LN}}_{V_N} \end{pmatrix} = \begin{bmatrix} v_1 = V_1 \\ v_2 = V_2 \\ v_3 = V_3 \\ v_4 = V_4 \\ \vdots \\ v_N = V_N \end{bmatrix}$$

   Compared to the Newton-Raphson algorithm, less complexity is required to reach the solution using the proposed PF method. The complexity of the proposed method is $\mathcal{O}(N^2)$, while the complexity of the Newton-Raphson method is $\mathcal{O}\big((2N-2)^3 + (2N-2)^2\big)$ in each iteration.

2. **Grid Consisting of Both P-Q and P-V Nodes**

   In the case of the existence of a P-V node in the system, the solver obtains the solution after executing the SLE through several iterations. In this context, the complexity of the matrix multiplication operation in 6.27 is $\mathcal{O}(MN)$ per iteration. Considering that there are only a few P-V nodes in distribution grids $(M < N)$, this complexity is significantly lower than the FLOPs ($\mathcal{O}\big((2N - 2 - M)^2\big)$) for the same operation in the Newton-Raphson method. To illustrate how this complexity is derived in the proposed PF method, let's assume that only one P-V node (at node 2) is present in the system in the initial step.

The corresponding SLE is then described in Equation 6.29:

$$\begin{bmatrix} Z_{11} & Z_{12} & \cdots & Z_{1N} \\ Z_{21} & Z_{22} & \cdots & Z_{2N} \\ Z_{31} & Z_{32} & \cdots & Z_{3N} \\ \vdots & \vdots & \ddots & \vdots \\ Z_{N1} & Z_{N2} & \cdots & Z_{NN} \end{bmatrix} \times \begin{bmatrix} i_{L1} \\ i_{L2} + i_{G1}^k \\ i_{L3} \\ i_{L4} \\ \vdots \\ i_{LN} \end{bmatrix} = \begin{bmatrix} v_1^k \\ v_2^k \\ v_3^k \\ v_4^k \\ \vdots \\ v_N^k \end{bmatrix} \Longrightarrow \tag{6.29}$$

$$\begin{pmatrix} v_1^k = \underbrace{Z_{11}i_{L1} + Z_{12}i_{L2}}_{V_{11}} + Z_{12}i_{G1}^k + \underbrace{Z_{13}i_{L3} + \cdots + Z_{1N}i_{LN}}_{V_{12}} \\ v_2^k = \underbrace{Z_{21}i_{L1} + Z_{22}i_{L2}}_{V_{21}} + Z_{22}i_{G1}^k + \underbrace{Z_{23}i_{L3} + \cdots + Z_{2N}i_{LN}}_{V_{22}} \\ v_3^k = \underbrace{Z_{31}i_{L1} + Z_{32}i_{L2}}_{V_{31}} + Z_{32}i_{G1}^k + \underbrace{Z_{33}i_{L3} + \cdots + Z_{3N}i_{LN}}_{V_{32}} \\ \vdots \\ v_N^k = \underbrace{Z_{N1}i_{L1} + Z_{N2}i_{L2}}_{V_{N1}} + Z_{N2}i_{G1}^k + \underbrace{Z_{N3}i_{L3} + \cdots + Z_{NN}i_{LN}}_{V_{N2}} \end{pmatrix} =$$

$$\begin{pmatrix} v_1^k = Z_{12}i_{G1}^k + \underbrace{V_{11} + V_{12}}_{V_1} \\ v_2^k = Z_{22}i_{G1}^k + \underbrace{V_{21} + V_{22}}_{V_2} \\ v_3^k = Z_{32}i_{G1}^k + \underbrace{V_{31} + V_{32}}_{V_3} \\ \vdots \\ v_N^k = Z_{N2}i_{G1}^k + \underbrace{V_{N1} + V_{N2}}_{V_N} \end{pmatrix} = \begin{pmatrix} v_1^k = Z_{12}i_{G1}^k + V_1 \\ v_2^k = Z_{22}i_{G1}^k + V_2 \\ v_3^k = Z_{32}i_{G1}^k + V_3 \\ \vdots \\ v_N^k = Z_{N2}i_{G1}^k + V_4 \end{pmatrix} =$$

$$\begin{bmatrix} Z_{12} \\ Z_{22} \\ Z_{32} \\ \vdots \\ Z_{N2} \end{bmatrix} \times \begin{bmatrix} i_{G1}^k \end{bmatrix} = \begin{bmatrix} v_1^k - V_1 \\ v_2^k - V_2 \\ v_3^k - V_3 \\ \vdots \\ v_N^k - V_N \end{bmatrix}$$

The constant values are shown in black, as they are computed before the iteration process. However, the red terms are updated in the iterations. In the final derived formulation indicated in bold, the Z matrix size is $\boldsymbol{N \times 1}$. Therefore, its complexity is $\boldsymbol{\mathcal{O}(N \times 1)}$ FLOPs in each iteration. When adding an additional P-V node in the grid, for instance at node 4, the SLE of 6.30 is

derived, which requires $\mathcal{O}(N \times 2)$ FLOPs per iteration.

$$\begin{bmatrix} Z_{11} & Z_{12} & \cdots & Z_{1N} \\ Z_{21} & Z_{22} & \cdots & Z_{2N} \\ Z_{31} & Z_{32} & \cdots & Z_{3N} \\ \vdots & \vdots & \ddots & \vdots \\ Z_{N1} & Z_{N2} & \cdots & Z_{NN} \end{bmatrix} \times \begin{bmatrix} i_{L1} \\ i_{L2} + i^k_{G1} \\ i_{L3} \\ i_{L4} + i^k_{G2} \\ \vdots \\ i_{LN} \end{bmatrix} = \begin{bmatrix} v^k_1 \\ v^k_2 \\ v^k_3 \\ v^k_4 \\ \vdots \\ v^k_N \end{bmatrix} \Longrightarrow \tag{6.30}$$

$$\begin{pmatrix} v^k_1 = \underbrace{Z_{11}i_{L1} + Z_{12}i_{L2}}_{V_{11}} + Z_{12}i^k_{G1} + \underbrace{Z_{13}i_{L3}}_{V_{12}} + Z_{14}i^k_{G2} + \underbrace{Z_{14}i_{L4} + \cdots + Z_{1N}i_{LN}}_{V_{13}} \\ v^k_2 = \underbrace{Z_{21}i_{L1} + Z_{22}i_{L2}}_{V_{21}} + Z_{22}i^k_{G1} + \underbrace{Z_{23}i_{L3}}_{V_{22}} + Z_{24}i^k_{G2} + \underbrace{Z_{24}i_{L4} + \cdots + Z_{2N}i_{LN}}_{V_{23}} \\ v^k_3 = \underbrace{Z_{31}i_{L1} + Z_{32}i_{L2}}_{V_{31}} + Z_{32}i^k_{G1} + \underbrace{Z_{33}i_{L3}}_{V_{32}} + Z_{34}i^k_{G2} + \underbrace{Z_{34}i_{L4} + \cdots + Z_{3N}i_{LN}}_{V_{33}} \\ \vdots \\ v^k_N = \underbrace{Z_{N1}i_{L1} + Z_{N2}i_{L2}}_{V_{N1}} + Z_{N2}i^k_{G1} + \underbrace{Z_{N3}i_{L3}}_{V_{N2}} + Z_{N4}i^k_{G2} + \underbrace{Z_{N4}i_{L4} + \cdots + Z_{NN}i_{LN}}_{V_{N3}} \end{pmatrix} =$$

$$\begin{pmatrix} v^k_1 = Z_{12}i^k_{G1} + Z_{14}i^k_{G2} + \underbrace{V_{11} + V_{12} + V_{13}}_{V_1} \\ v^k_2 = Z_{22}i^k_{G1} + Z_{24}i^k_{G2} + \underbrace{V_{21} + V_{22} + V_{23}}_{V_2} \\ v^k_3 = Z_{32}i^k_{G1} + Z_{34}i^k_{G2} + \underbrace{V_{31} + V_{32} + V_{33}}_{V_3} \\ \vdots \\ v^k_N = Z_{N2}i^k_{G1} + Z_{N4}i^k_{G2} + \underbrace{V_{N1} + V_{N2} + V_{N3}}_{V_N} \end{pmatrix} = \begin{pmatrix} v^k_1 = Z_{12}i^k_{G1} + Z_{14}i^k_{G2} + V_1 \\ v^k_2 = Z_{22}i^k_{G1} + Z_{24}i^k_{G2} + V_2 \\ v^k_3 = Z_{32}i^k_{G1} + Z_{34}i^k_{G2} + V_3 \\ \vdots \\ v^k_N = Z_{N2}i^k_{G1} + Z_{N4}i^k_{G2} + V_4 \end{pmatrix} =$$

$$\begin{bmatrix} Z_{12} & Z_{14} \\ Z_{22} & Z_{24} \\ Z_{32} & Z_{34} \\ \vdots & \vdots \\ Z_{N2} & Z_{N4} \end{bmatrix} \times \begin{bmatrix} i^k_{G1} \\ i^k_{G2} \end{bmatrix} = \begin{bmatrix} v^k_1 - V_1 \\ v^k_2 - V_2 \\ v^k_3 - V_3 \\ \vdots \\ v^k_N - V_N \end{bmatrix}$$

Finally, when the number of P-V nodes in the system is M, the SLE of 6.31 is formulated, which requires $\mathcal{O}(N \times M)$ FLOPs in each iteration.

$$\begin{bmatrix} Z_{12} & Z_{14} & \cdots & Z_{1M} \\ Z_{22} & Z_{24} & \cdots & Z_{2M} \\ Z_{32} & Z_{34} & \cdots & Z_{3M} \\ \vdots & \vdots & \ddots & \vdots \\ Z_{N2} & Z_{N4} & \cdots & Z_{NM} \end{bmatrix} \times \begin{bmatrix} i^k_{G1} \\ i^k_{G2} \\ \vdots \\ i^k_{GM} \end{bmatrix} = \begin{bmatrix} v^k_1 - V_1 \\ v^k_2 - V_2 \\ v^k_3 - V_3 \\ \vdots \\ v^k_N - V_N \end{bmatrix} \tag{6.31}$$

The required FLOPs for the proposed method (PM) and the Newton-Raphson technique are tabulated in Table 6.1, per iteration. As indicated, the required

FLOPs, $\mathcal{O}(NM)$, for the PM are significantly less than the required FLOPs, $\mathcal{O}\big((2N-2-M)^3\big)+\mathcal{O}\big((2N-2-M)^2\big)$, for the Newton-Raphson method in each solution iteration.

FLOPs	Method	
	Newton-Raphson	PM
Inversion	$\mathcal{O}\big((2N-2-M)^3\big)$	0
Multiplication	$\mathcal{O}\big((2N-2-M)^2\big)$	$\mathcal{O}(NM)$

TABLE 6.1: Number of FLOPs of the solution as per iteration

- **Convergence Rate**

  The Newton-Raphson and the proposed PF method are iterated multiple times until the predefined tolerance (ϵ) is satisfied. While Newton's method is quadratically convergent, the fixed-point iteration technique converges linearly to the solution [154]. From the convergence rate point of view, the Newton-Raphson method has an advantage over the fixed-point iteration technique. However, the proposed Fixed-Point Iteration PF solution exploits the linearized model of the load and generator, significantly simplifying the SLE as of 6.31, which reduces the solver execution time due to dealing with fewer FLOPs in the process. Additionally, the rate of convergence is enhanced by applying the optimal relaxation factor associated with the P-V nodes [155].

In this context, conducting an exact comparison of the computational burden between the solvers is not feasible due to potential differences in how the PF algorithms have been programmed and implemented, which may not be optimal. Additionally, the computational cost of iterative solvers depends on the required number of iterations to reach a solution. Given the various operating conditions (such as node number, system loading, line parameters, and the number of P-V nodes), as well as the solver's initial set points, the number of required iterations can vary across different problems. Despite the challenges in determining the exact number of required iterations to solve a PF problem, knowing the required FLOPs for each iteration and the solver's convergence rate allows for a rough estimation of the computational burden of the solvers. This estimation serves as an indication of solver speed assessment. In this regard, the MATLAB execution time for the main Newton-Raphson operation functions (i.e., matrix inversion and multiplication), as shown in Fig. (6.5-b), is divided by the execution time for the main operation function (i.e., matrix multiplication) of the proposed PF method, shown in Fig. (6.5-a). The division outcome, as illustrated in Fig. (6.5-c), indicates that the PF method is much faster than the Newton-Raphson approach when the system is large. For instance, in each iteration, the proposed method is approximately 2000 times faster than the Newton-Raphson method when there are 15 P-V nodes in a grid with

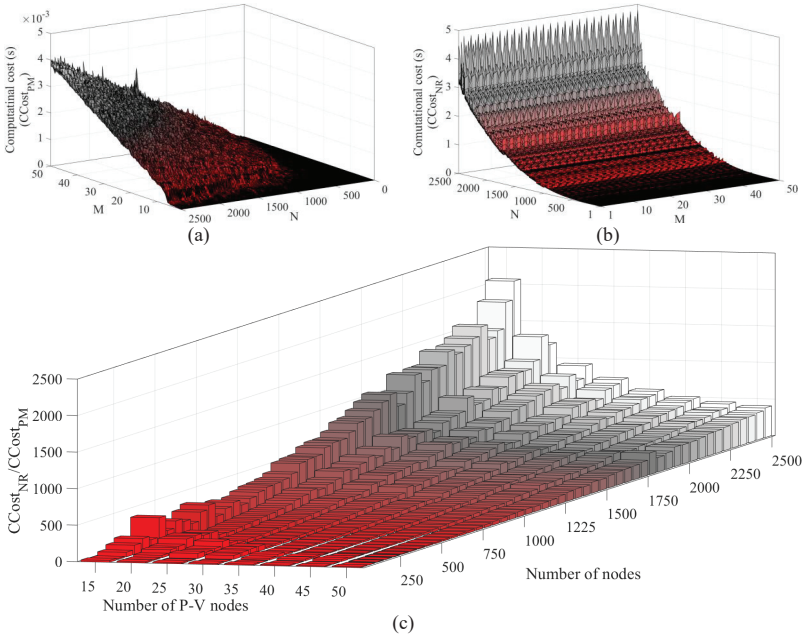

FIGURE 6.5: MATLAB execution time of the required FLOPs for the matrix inversion and multiplication. (a) shows the elapsed time of $[Z]_{N\times M} \times [iG]_{1\times M}$. (b) shows the elapsed time of $[J]^{-1}_{(2N-2N-M)\times(2N-2N-M)} \times [P;Q]_{1\times 2N-2-M}$. (c) shows how many times the PM is faster than NR method per iteration.

2500 nodes. In other words, to match the computational cost of the Newton-Raphson method, the PM has 2000 iteration chances to converge, while Newton-Raphson solves the PF problem in one iteration. Considering that the FPI and Newton approaches are linearly and quadratically convergent, respectively, and the fact that the FPI solution generally converges well for most distribution systems (connected to the dominant bulk power source) with adequate capacity to serve the load [156], the mentioned number of iteration chances is much more than the required number of iterations to solve the PF problem by the PM method. Therefore, the proposed method is faster than the Newton-Raphson method for large grids. It is worth noting that the same outcome has been observed in other fields of study dealing with solving systems of non-linear equations [157] when the number of elements in the Jacobian matrix is large.

6.6 Results

The PF results calculated by the proposed method (PM) are compared with those obtained by DIgSILENT PowerFactory [158] on the benchmark IEEE 33-bus test system and on the "Seebach" distribution grid, a large medium voltage (MV) network (20 kV) operated by Bayernwerk AG [159] in Germany. This MV grid has 555 nodes, of which three nodes include distributed generators operating in P-Q mode. The effectiveness of the proposed linearized generator model is assessed by assuming that the grid has one voltage regulator. It has been shown that this PM is stable in terms of convergence when there are multiple P-V nodes in the system. DIgSILENT PowerFactory has its own interface, which calculates the solution based on the Newton-Raphson method. However, the PM has not been computationally compared with DIgSILENT PowerFactory since it has been implemented in MATLAB. From an accuracy point of view, the obtained PM results track well those calculated by DIgSILENT PowerFactory. In this respect, the considered quantification indices are the maximum percentage error in the voltage magnitude and the maximum error in the voltage phase angle over all nodes. From a computational efficiency perspective, moreover, the computational cost and convergence rate of the PM solver are compared for different relaxation factors.

- **Case A: IEEE 33-Bus Including P-Q Nodes**

  Fig. 6.6 shows the node connections through branches in the IEEE 33-Bus system. Except for node 1, all nodes include a load. The grid parameters for this system are found in **Appendix D**.

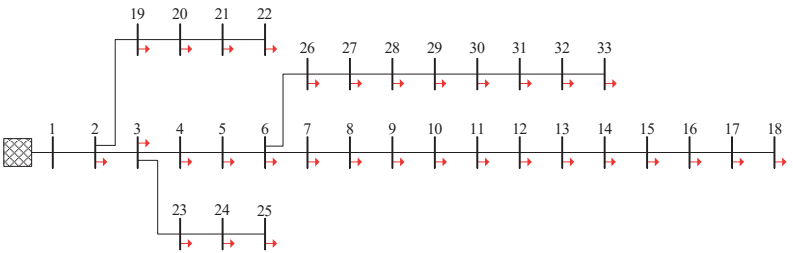

FIGURE 6.6: IEEE 33-bus Test System (including only loads)

Considering the passive system, the obtained PF results (voltage magnitude and voltage angle) by DIgSILENT PowerFactory and the proposed FPI solver, including either only the linear ZI load model (named LPF) or only the proposed nonlinear load model (called NLPF), are shown in Fig. 6.7 and Fig. 6.8. The fitted ZI load coefficients are: $C_Z = -1$, $C_Z^{'} = -1$, $C_I = 2$, and $C_I^{'} = 2$.

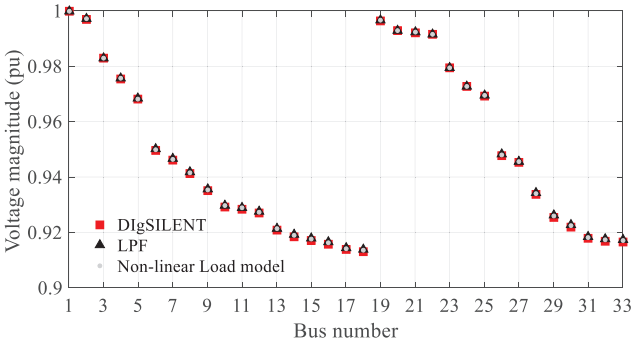

FIGURE 6.7: Node Voltage magnitude

As seen in Fig. 6.7, the solvers obtain the same calculated voltage magnitudes. Although the calculated voltage angles by the non-linear solvers (DIgSILENT PowerFactory and NLPF) are the same, the LPF results (shown in Fig. 6.8) do not exactly match those calculated by the non-linear solvers for the nodes at the end of the feeder.

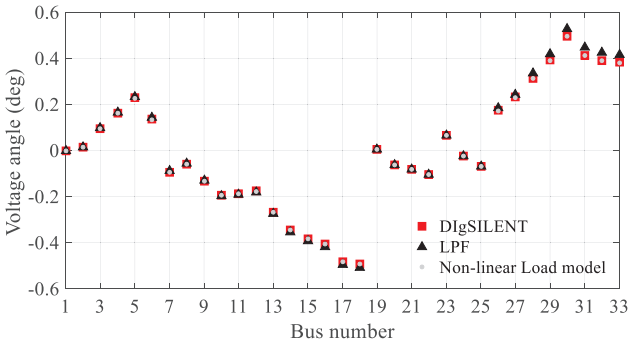

FIGURE 6.8: Node Voltage Angle

Table 6.2 indicates the maximum percentage error (PE) in voltage magnitude and the maximum absolute error (AE) in voltage angle over all nodes.

Method w.r.t DIgSILENT	Voltage magnitude PE (%)	Voltage angle AE (deg)
LPF	0.0799	0.0349
NLPF	0.0542	0.0029

TABLE 6.2: Number of FLOPs of the solution as per iteration

According to the standard EN 50160 (or EN 61000), the voltage deviation should be confined within a range of ±10% of nominal voltage in distribution grids. As the voltage drop in this scenario is about 10%, the proposed method is accurate in such a high voltage drop, as indicated by the tabulated results. The MATLAB execution times for the LPF and LNPF solvers are 2.0269e-04 s and 3.0890e-04 s, respectively, in this case. Considering two additional high load conditions in which the system loading is 150% and 200%, the accuracy of the proposed PF method is assessed here.

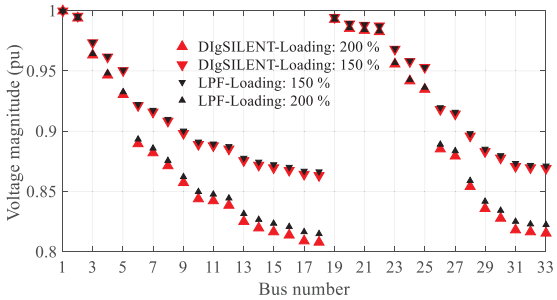

FIGURE 6.9: Node Voltage magnitude

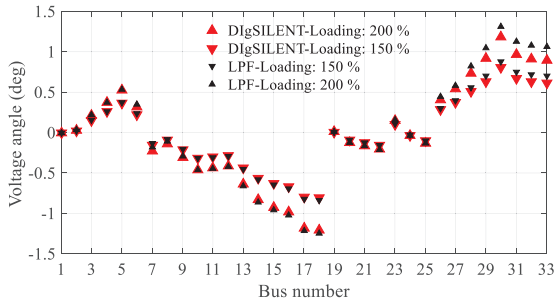

FIGURE 6.10: Node Voltage Angle

The calculated voltage magnitudes and voltage angles by the PF results are shown in Fig. 6.9 and Fig. 6.10, respectively. For 150% and 200% loading conditions, the maximum percentage errors in voltage magnitude are 0.3140% and 0.9051%, while the maximum absolute errors in voltage angle are 0.0874 degrees and 0.17 degrees, respectively. The slack bus voltage is assumed to be 1 pu in this case. However, more accurate PF results are achieved when a higher voltage is set for the slack bus.

- **Case B: IEEE 33-Bus Including P-Q and P-V Nodes**

  In this scenario, the grid is assumed to be operated with both P-Q and P-V nodes. Accordingly, a model of the proposed synchronous generator is added to the end of the main branch at node 18, as shown in Fig. 6.11.

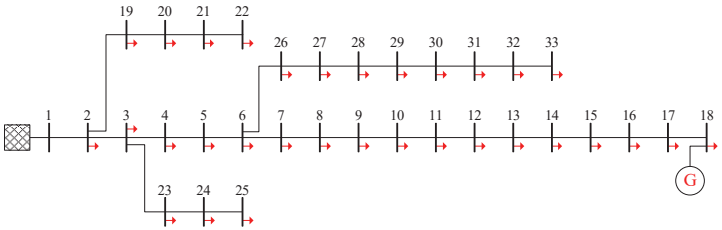

FIGURE 6.11: IEEE 33-bus Test System (including both P-V and P-Q)

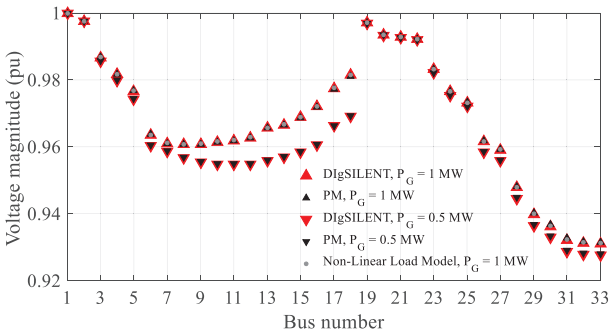

FIGURE 6.12: Node Voltage magnitude

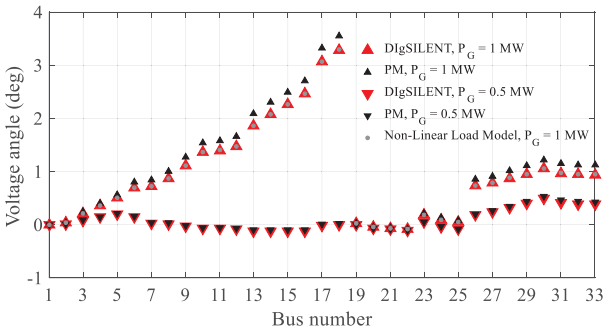

FIGURE 6.13: Node Voltage Angle

The internal voltage of the synchronous machine is set to 0.98 pu. To evaluate the effectiveness of the proposed linearized generator model, the PF results are compared with those calculated by DIgSILENT PowerFactory and the NLPF method. The impact of two different generator powers, 0.5 MW and 1 MW, on the voltage magnitude and voltage angle over all nodes is shown in Fig. 6.12 and Fig. 6.13, respectively. The maximum PE in voltage magnitude and the maximum AE in voltage angle over all nodes, along with the solver's execution times, are summarized in Table 6.3 and Table 6.4, respectively.

Method w.r.t DIgSILENT	Voltage magnitude PE (%)	Voltage angle AE (deg)
PM ($P_{ref=1MW}$)	0.0585	0.2624
NLPF ($P_{ref=1MW}$)	0.0253	0.0133
PM ($P_{ref=0.5MW}$)	0.0494	0.0477

TABLE 6.3: Error of voltage magnitude and phase angle

Method	Computational Time (s)
PM ($P_{ref=1MW}$)	2.0269e-04
NLPF ($P_{ref=1MW}$)	3.0890e0-04
PM ($P_{ref=0.5MW}$)	1.8184e-04

TABLE 6.4: Solver Execution Time

According to the tabulated results, the proposed methods are comparable with DIgSILENT PowerFactory. Nevertheless, at the expense of more execution time, the use of the non-linear load model yields more accurate results than exploiting the linear load model. In another scenario, considering the internal voltage of 0.95 pu, the proposed linear PF results are compared with DIgSILENT PowerFactory in Table 6.5 when the synchronous reactances are set to 1 pu and 1.7 pu.

Synchronous reactance	Voltage magnitude PE (%)	Voltage angle AE (deg)
$X = 1$ pu	0.0636	0.3572
$X = 1.7$ pu	0.0867	0.3566

TABLE 6.5: Error of voltage magnitude and phase angle

All in all, the obtained results indicate that the proposed linear model of the synchronous generator is accurate enough to be used as the P-V node in the PF calculations. Apart from accuracy, the convergence rate of the proposed method is adjusted by the relaxation factor (γ), as explained in Subsection 6.3. In this respect,

the relaxation factor that yields the minimum number of required iterations is selected over 5000 Monte Carlo simulations, varying γ with steps of 0.01 from 0.2 to 1.9 for each trial.

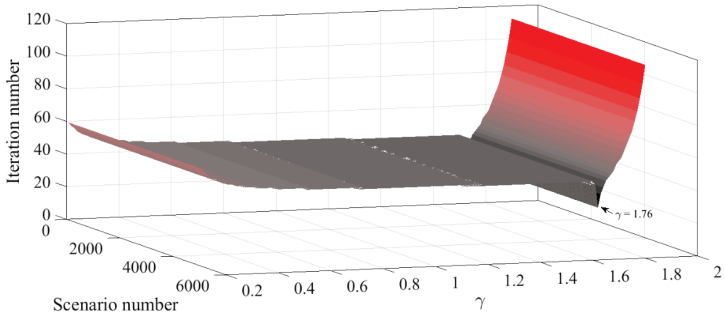

FIGURE 6.14: gamma

The internal voltage and the active power set point of the generator are 0.98 pu and 1 MW, respectively, for all the trials. As shown in Fig. 6.14, the optimum γ is found to be 1.76, which yields the minimum number of required iterations, specifically 27, in all scenarios where loads are randomly varied. To visually illustrate how γ affects the PF convergence rate, a specific problem is solved using different relaxation factors.

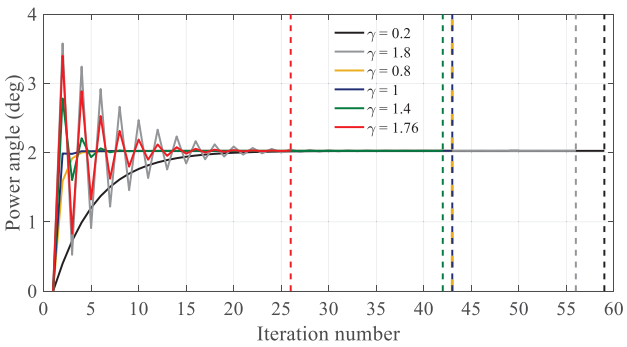

FIGURE 6.15: Power angle variation for different relaxation factors

Fig. 6.15 and Fig. 6.16, respectively, show the impact of the relaxation factor on the power angle and on the generator's active power. In this context, the power angle changes to ensure that the generator supplies the reference set value of 1 MW to the system.

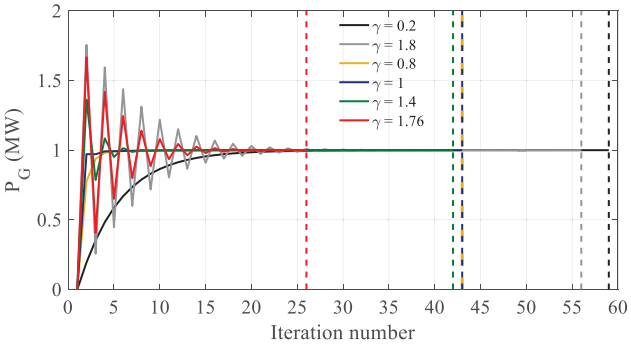

FIGURE 6.16: Generator active power variation for different relaxation factors

As shown in the figures, the solver converges to the solution with and without oscillations under over- and under-relaxation modes, respectively. However, compared to the chosen relaxation factors, the value $\gamma = 1.76$ yields the minimum number of iterations required to satisfy the target. It is worth noting that depending on the installation point and the number of installed generators in the system, the number of required iterations may vary. To illustrate this, the same generator is gradually added to all the grid nodes starting from node 1 to node 33, and the number of iterations required to solve the problem is counted.

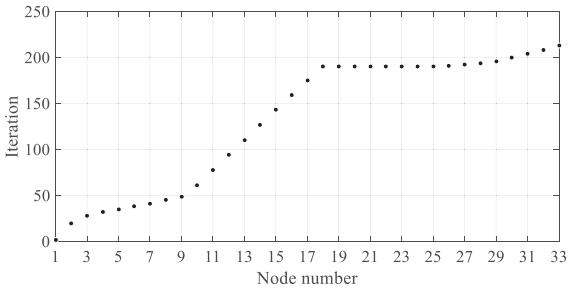

FIGURE 6.17: GenLocations

Fig. 6.17 shows that the lowest number of iterations (two iterations) is obtained when a generator is installed on node 1, where the electrical distance is short. However, the number of iterations sharply increases from 2 to 190 iterations by gradually adding other generators from node 1 to node 18 as the electrical distance of the newly added generators increases. The iteration number does not significantly change when other generators are installed from node 19 to node 33.

These tests demonstrate that the proposed PF method is robust when there is more than one generator in the grid.

- **Case C: "Seebach" Distribution Grid**

  The performance of the PM for a large distribution grid is assessed in this section. PF calculations by the PM and DIgSILENT solvers have been performed for the "Seebach" grid, as depicted in Fig. 6.18, operated by Bayernwerk Netz GmbH.

FIGURE 6.18: "Seebach" MV Network

As this network includes both radial and mesh feeders, the capability of the PM in solving systems with complicated structures is also demonstrated in this case. Different operating conditions are considered here:

1. **Passive System**: it is assumed that only passive loads are energized in this scenario. The PF results, including the voltage magnitude and the voltage angle for the radial section consisting of 10 nodes, are shown in Fig. 6.19 and Fig. 6.20, respectively. There is a sharp voltage drop from node 542 to node 544, as the first three line segments (L533-536, L536-539, and L539-542) have considerably smaller lengths than the other lines. Due to the absence of DGs in the passive system, the voltage magnitude does not exceed the substation voltage (1 pu). The maximum percentage error in voltage magnitude and

the maximum absolute error in voltage angle over all nodes with respect to DIgSILENT are 3.7065e-05% and 1.8745e-06 deg, respectively. The PM solves the PF problem without iteration in a single shot, as there is no P-V node in the network. The solving execution time is 9.7494e-04 s for the PM.

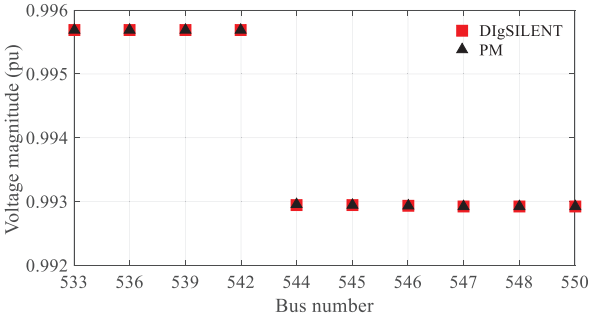

FIGURE 6.19: Node Voltage magnitude

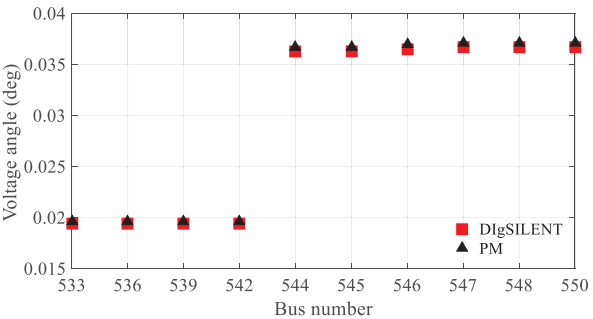

FIGURE 6.20: Node Voltage Angle

2. **Active System**: in this scenario, it is assumed that three DGs operating in P-Q mode are connected to node 343, node 424, and node 503. The installation points of these DGs are shown in Fig. 6.21. The injected power by the DGs leads to bidirectional flowing power and consequently voltage rise in the network. As an example, the impact of the DG connected to node 343 on the voltage magnitude and the voltage angle of the grid section where nodes are radially connected is shown in Fig. 6.22 and Fig. 6.23, respectively. As can be seen, the voltage magnitude of the two nodes at the end of the section has increased more than the others. Considering the DIgSILENT PF results as the reference, the maximum percentage error in voltage magnitude and the

maximum absolute error in voltage angle over all nodes are 9.4360e-05% and 4.7331e-04 deg, respectively.

FIGURE 6.21: "Seebach" MV Network Including DGs Operating in P-Q Mode

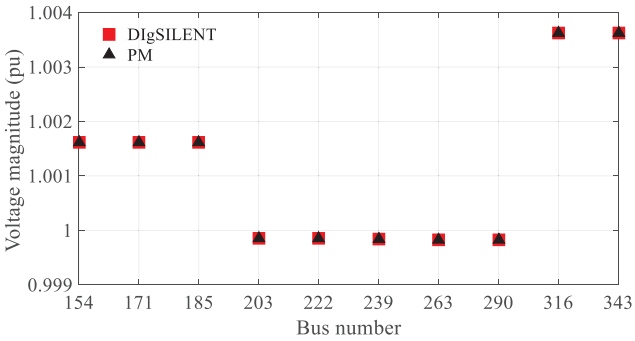

FIGURE 6.22: Node Voltage magnitude

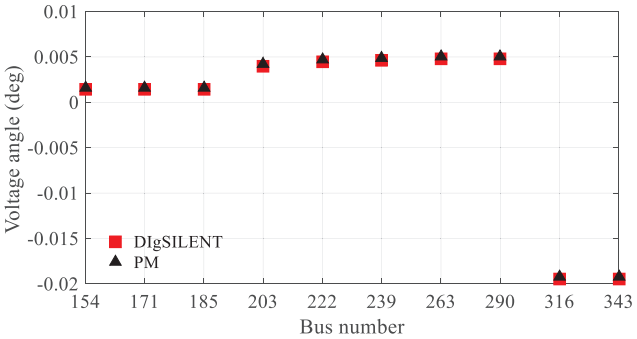

FIGURE 6.23: Node Voltage Angle

Since the DGs are modeled as the negative load in this case, no iteration is required to meet the solution. The solver takes 9.7214e-04 s to solve this problem.

3. **Operating Node 153 in P-V Mode**: in addition to the passive and negative loads, node 153 is assumed to be operated in P-V mode in this scenario.

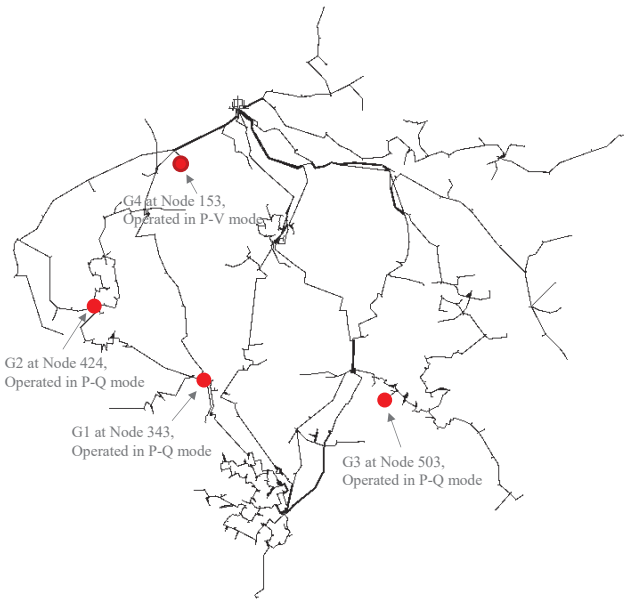

FIGURE 6.24: Bus 153 as a P-V node in"Seebach" MV Network

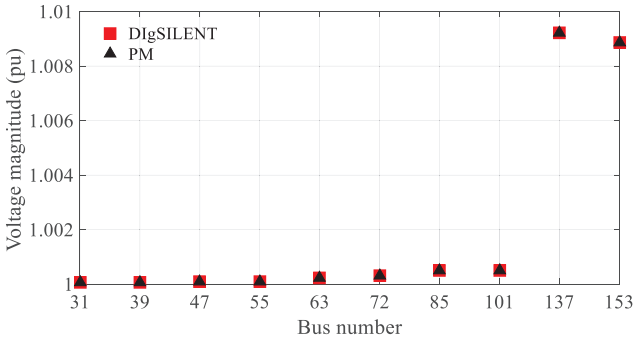

FIGURE 6.25: Node Voltage magnitude

This P-V node is illustrated in Fig. 6.24. The reference voltage and power working points are considered to be 0.98 pu and 10 MW, respectively. To demonstrate how the voltage is controlled at this node, the calculated voltage magnitude and the voltage angle for a grid section consisting of 10 nodes that are radially connected are shown in Fig. 6.25 and Fig. 6.26, respectively.

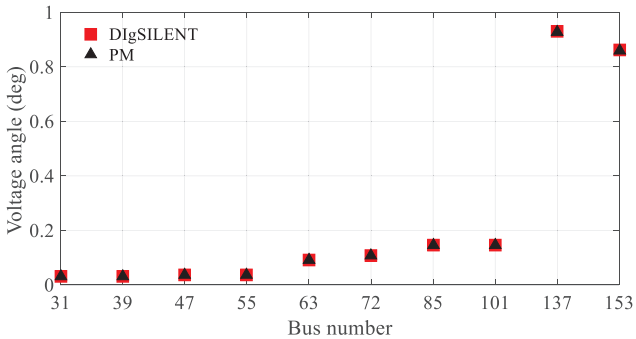

FIGURE 6.26: Node Voltage Angle

The maximum percentage error in voltage magnitude and the maximum absolute error in voltage angle over all nodes are 6.8265e-04% and 0.0046 deg, respectively. Due to the presence of the P-V node, the solver requires some iterations to converge to the solution. MATLAB took 9.8374e-04 s to solve this problem using the PM.

4. **Operating Node 554 in P-V Mode**: instead of node 153, node 554 is assumed to operate as the P-V node in this scenario. The P-V node is shown in Fig. 6.27.

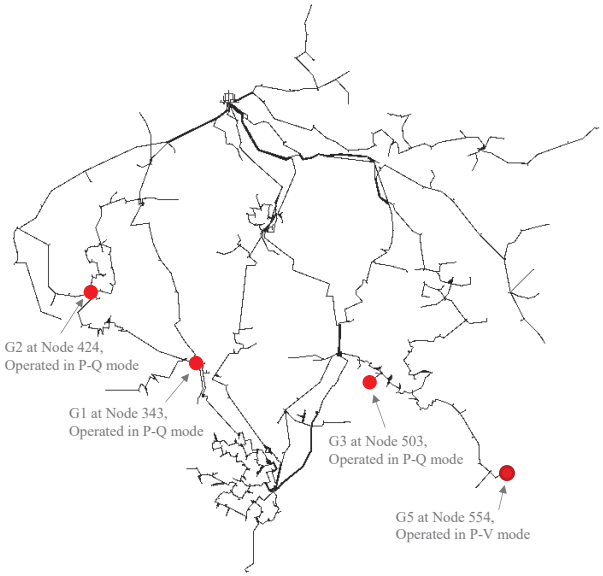

FIGURE 6.27: Bus 554 as a P-V node in"Seebach" MV Network

For the radially connected 10 nodes, including the P-V node, the voltage profiles, including the voltage magnitude and the phase angle, are shown in Fig. 6.28 and Fig. 6.29, respectively.

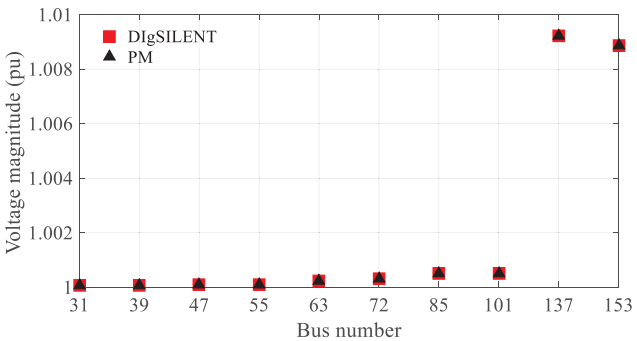

FIGURE 6.28: Node Voltage magnitude

The maximum percentage error in voltage magnitude and the maximum absolute error in voltage angle over all nodes are 0.0041% and 0.0291 deg, respectively, with respect to DIgSILENT. The solver takes 0.0011 s to reach the

solution for this problem.

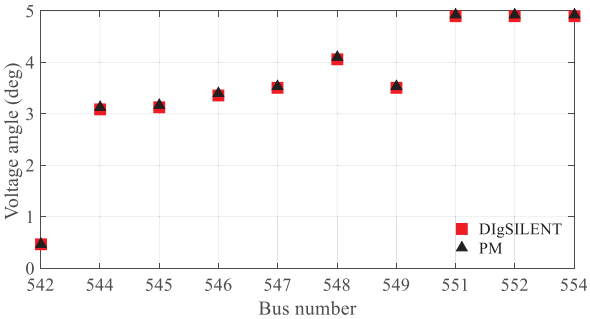

FIGURE 6.29: Node Voltage Angle

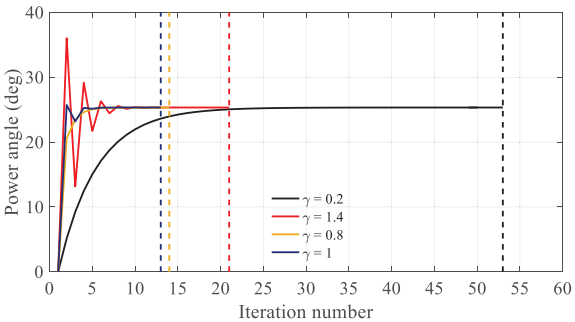

FIGURE 6.30: Power angle variation for different relaxation factors

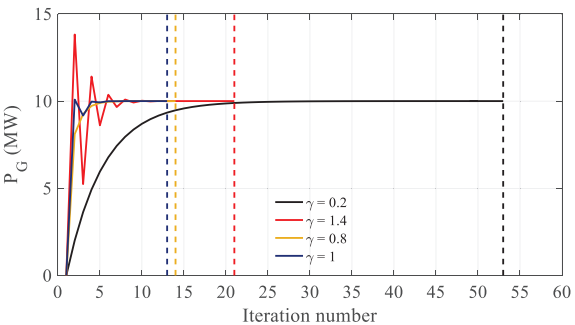

FIGURE 6.31: active power variation for different relaxation factors

To illustrate the impact of the relaxation factor (γ) on the rate of convergence, Fig. 6.31 and Fig. 6.30 depict how the power angle and, accordingly, the generator power vary for different γ. As observed, the solver reaches the solution more quickly when $\gamma = 1$. However, as explained earlier, under over-relaxation and under-relaxation modes, the solver approaches the solution with and without oscillations, respectively. Nevertheless, as shown in Fig. 6.32 and Fig. 6.33, the solver becomes unstable when $\gamma = 1.8$.

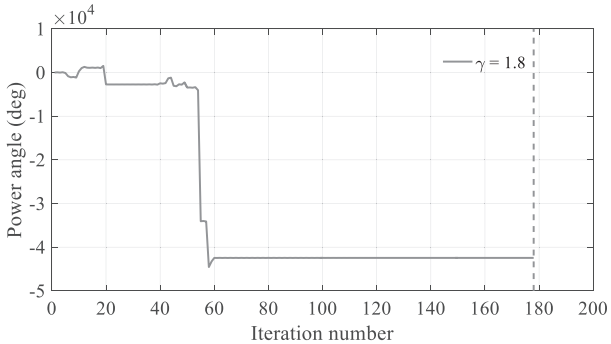

FIGURE 6.32: Power angle variation for relaxation factor of 1.8

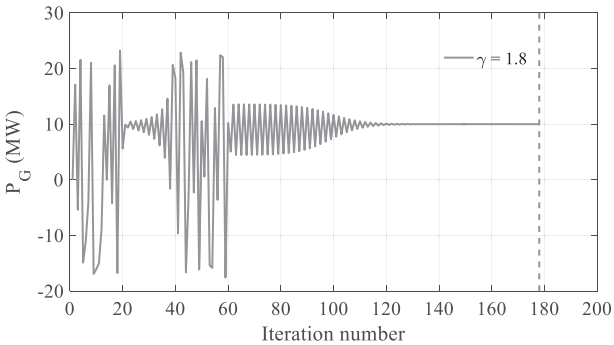

FIGURE 6.33: Active power variation for relaxation factor of 1.8.

6.7 Conclusion

In this chapter, a novel model-based PF approach for distribution systems has been introduced. The backbone of the solver is based on the fixed-point iteration algorithm. This solution integrates a linear current injection model for loads and generators, representing the P-Q and P-V nodes, respectively. The linear load current injection model is an already developed ZI load model, leading to a SLE that can be solved without iteration when there are only P-Q nodes in the network. The linear generator current injection model is derived by applying the partial derivative rule to the synchronous generator active power formula. In this way, the generator power angle is relaxed using a relaxation factor, which can influence the rate of convergence. To maximize this rate, it has been demonstrated how the optimum relaxation factor is obtained through Monte Carlo simulations. Additionally, the proposed solution requires significantly fewer FLOPs per iteration compared to the classical Newton-Raphson method. However, the results section reveals that the PF flow results are comparable to those calculated by DIgSILENT PowerFactory, which utilizes the Newton-Raphson method.

Chapter 7

Conclusion and Future Work

7.1 Conclusion

System monitoring is the most essential task in the automation of complex power systems (ACS). In this context, monitoring the distribution systems based on the state estimation concept is the main focus of this dissertation. In Chapter 1, it has been explained that the integration of a large number of active elements, including distributed generation (PV and wind farms), battery storage systems, and prosumers, imposes network contingencies. To address this issue, the system operator should be able to oversee the system behavior with an appropriate time granularity. Considering the lack of measurement units in distribution systems, the described state estimation concept in Chapter 2 can provide system operators with an accurate estimation of whole system states (e.g., voltage magnitude and phase angle) so that the right decision can be made confidently to apply suitable control strategies for the safe operation of the power network. To meet this goal, a new data-driven distribution system state estimation technique is introduced in Chapter 3. As a data-driven method, the proposed estimation approach exploits an ANN modeled as a state estimator. The ANN-based estimator, derived by applying the Bayesian regularization learning technique to the training data, is a mathematical model that does not involve the time-consuming calculations of the Jacobian matrix and the gain matrix inverse, as in model-based WLS algorithms. Thus, the proposed estimator is tremendously fast and executes in a few milliseconds without convergence issues. To obtain a fast monitoring system capturing the system states, the proposed ANN-based estimator is coupled with PMUs, since the reporting rate of these modern monitoring devices is above 1 Hz. Consequently, by adjusting the reporting rate of the ANN-based estimator to a few seconds, the proposed monitoring system can rapidly capture the system states (ideally once per second). In this context, moreover, the computational complexity of the proposed ANN-based estimator has been compared with linear- and nonlinear-model-based DSSE problems in Chapter

4 in terms of FLOPs and the elapsed time. As a result, it has been found that the computational burden of the proposed estimator is less than that of model-based DSSE problems. Therefore, it can be used in ADMS systems to satisfy the requirements of real-time applications. To make this solution scalable, two distributed architectures, parallel and multi-area, are described in Chapter 5. In both architectures, the estimation accuracy is enhanced, and the computational burden is distributed over small problems. Last but not least, a linear fast power flow method for distribution grids is proposed in Chapter 6, which is used to produce the training data for the proposed ANN-based estimator. In this method, the linear current injection model of P-Q and P-V nodes is integrated into the fixed-point iteration technique. When the power system is passive or includes active components operated in P-Q mode, the power flow solution meets the solution without iteration. However, iteration is needed when there are P-V nodes in the network. In this case, nevertheless, the rate of convergence is increased by applying the optimal relaxation factor. Moreover, it has been shown that the proposed method is faster than the classical Newton method for large distribution grids. Thus, both the proposed state estimation and the linear power flow approach are potential fast solutions that can be used in distribution automation and operational functions.

7.2 Future Work

The proposed ANN-based estimator maps synchrophasor measurements to node voltages in polar coordinate. In addition to synchrophasor measurements, active and reactive power flows can be considered in the input set, as demonstrated in some scenarios in this dissertation. It is also suggested to incorporate other available measurements, such as meteorological data, in the input dataset to further improve estimation accuracy. Although the proposed estimator provides state estimations with good accuracy, training the estimator to map measurements into system states for all probable scenarios, which are infinite, is not feasible. Therefore, it is recommended to consider solutions based on the system's worst-case conditions, as highlighted in the system observability assessment. This concern becomes more critical in systems involving switches. If the number of switches is limited, it is possible to generate the required training for all scenarios based on different combinations of the switches' statuses. However, in the case of multiple switches in the grid, numerous scenarios correspond to different switches' statuses. With n switches in the system, there are 2^n different network typologies yields, accordingly, 2^n different problems. Then, generating the 2^n training datasets may not be feasible when there is a large number of switches in the grid. In such cases, it is recommended to develop a solution that can determine which switches have the dominant impact on the system states and accordingly eliminate scenarios where changing

the switch status does not significantly affect the states. To generate training data considering more switches, the power flow technique should quickly calculate the solution. While the proposed power flow approach uses an optimal relaxation factor to increase the rate of convergence, obtaining this factor through the Monte Carlo approach in this work may be time-consuming, especially with a large number of switches. To address this issue, further research should be conducted to derive a closed-form solution for obtaining the optimal relaxation factor instead of relying on the Monte Carlo method.

Appendix A

Forward and Backward Substitution FLOPs

The number of counted FLOPs in forward and backward substitution steps is represented here:

- **Forward Substitution**
  If A is a lower triangular matrix with non-zero diagonal elements, the system of equations $Ax = b$ is written as:

$$\begin{bmatrix} a_{11} & 0 & \dots & 0 \\ a_{21} & a_{22} & \dots & 0 \\ \vdots & \vdots & \ddots & \vdots \\ a_{m1} & a_{m2} & \dots & a_{mm} \end{bmatrix} \begin{bmatrix} x_1 \\ x_2 \\ \vdots \\ x_m \end{bmatrix} = \begin{bmatrix} b_1 \\ b_2 \\ \vdots \\ b_m \end{bmatrix}$$

  The solutions can be represented as:

$$\begin{aligned} x_1 &= \tfrac{b_1}{a_{11}} \\ x_2 &= \tfrac{(b_2 - a_{21}x_1)}{a_{22}} \\ &\vdots \\ x_m &= \tfrac{(b_m - a_{m1}x_1 - a_{m2}x_2 - \ldots - a_{m,m-1}x_{m-1})}{a_{mm}} \end{aligned}$$

  As can be observed, x_1 requires only one FLOP, which is a single division. x_2 needs three FLOPs, involving 1 multiplication, 1 division, and 1 subtraction. Similarly, x_3 requires five FLOPs, comprising 2 multiplications, 1 division, and 2 subtractions. Following this pattern, computing x_m require $(2m - 1)$ FLOPs. Therefore,

the total number of FLOPs required for forward substitution is:

$$\mathcal{O}_{ForwardStep} = 1 + 3 + 5 + \ldots + (2m - 1) = m^2$$

- **Backward Substitution**
  Instead of the lower triangular matrix, the matrix A is a upper triangular in this step:

$$\begin{bmatrix} a_{11} & \ldots & a_{1,m-1} & a_{1m} \\ \vdots & \ddots & \vdots & \vdots \\ 0 & \ldots & a_{m-1,m-1} & a_{m-1,m} \\ 0 & 0 & \ldots & a_{mm} \end{bmatrix} \begin{bmatrix} x_1 \\ \vdots \\ x_{m-1} \\ x_m \end{bmatrix} = \begin{bmatrix} b_1 \\ \vdots \\ b_{m-1} \\ b_m \end{bmatrix}$$

  The solutions can be represented as:

$$x_m = \frac{b_m}{a_{mm}}$$

$$x_{m-1} = \frac{(b_{m-1} - a_{m-1,m} x_m)}{a_{m-1,m-1}}$$

$$x_{m-2} = \frac{(b_{m-2} - a_{m-2,m} x_m - a_{m-2,m-1} x_{m-1})}{a_{m-2,m-2}}$$

$$\vdots$$

$$x_1 = \frac{(b_1 - a_{12} x_2 - a_{13} x_3 - \ldots - a_{1,m} x_m)}{a_{11}}$$

  Thus, the overall FLOPs required for backward substitution are the same as for forward substitution:

$$\mathcal{O}_{BackwardStep} = \mathcal{O}_{ForwardStep} = m^2$$

Appendix B

Relaxation Method

The relaxation method is an iterative solution for solving the system of linear equations $Ax = b$. This approach generalizes the Gauss-Seidel method by introducing a relaxation factor $\gamma > 0$. By determining the optimal value for γ, the convergence rate of the solution x^k is enhanced by adjusting the size of the correction:

$$x_i^{k+1} = x_i^k + \frac{\gamma}{A_{ii}} \left(b_i - \sum_{j=1}^{i-1} A_{ii} x_j^{k+1} - \sum_{j=i}^{n} A_{ii} x_j^k \right) \tag{B.1}$$

Where $1 \leq i \leq n$

This method is known as the successive relaxation (SR) method, where the system reaches the solution either with oscillations under over-relaxation mode or without oscillations in under-relaxation mode:

- $0 \leq \gamma \leq 1 \rightarrow under - relaxation$
- $\gamma = 1 \rightarrow Gauss - Seidel$
- $\gamma \geq 1 \rightarrow over - relaxation$

Formula B.1 is employed to relax the power angle (6.10) in this dissertation. To relax the load equivalent current model (6.12), another form of B.1 is utilized:

$$x_i^{k+1} = (1 - \gamma) x_i^k + \frac{\gamma}{A_{ii}} \left(b_i - \sum_{j=1}^{i-1} A_{ii} x_j^{k+1} - \sum_{j=i}^{n} A_{ii} x_j^k \right) \tag{B.2}$$

Appendix C

Jacobian Submatrices and Power Mismatch Formulation

- **Jacobian Submatrices [155]**:

$$
\begin{aligned}
J_{jk}^{P\theta} &= \frac{\partial P_j(v)}{\partial \theta_k} = |V_j||V_k|\big(G_{jk}\sin(\theta_j-\theta_k) - B_{jk}\cos(\theta_j-\theta_k)\big)\\
J_{jj}^{P\theta} &= \frac{\partial P_j(v)}{\partial \theta_j} = -Qj(v) - B_{jj}|V_j|^2\\
J_{jk}^{Q\theta} &= \frac{\partial Q_j(v)}{\partial \theta_k} = -|V_j||V_k|\big(G_{jk}\cos(\theta_j-\theta_k) + B_{jk}\sin(\theta_j-\theta_k)\big)\\
J_{jj}^{Q\theta} &= \frac{\partial Q_j(v)}{\partial \theta_k} = Pj(v) - G_{jj}|V_j|^2\\
J_{jk}^{PV} &= \frac{\partial P_j(v)}{\partial |V_k|} = |V_j|\big(G_{jk}\cos(\theta_j-\theta_k) + B_{jk}\sin(\theta_j-\theta_k)\big)\\
J_{jj}^{PV} &= \frac{\partial P_j(v)}{\partial |V_j|} = \frac{P_j(v)}{|V_j|} + G_{jj}|V_j|\\
J_{jk}^{QV} &= \frac{\partial Q_j(v)}{\partial |V_k|} = |V_j|\big(G_{jk}\sin(\theta_j-\theta_k) - B_{jk}\cos(\theta_j-\theta_k)\big)\\
J_{jj}^{QV} &= \frac{\partial Q_j(v)}{\partial |V_j|} = \frac{Q_j(v)}{|V_j|} - B_{jj}|V_j|
\end{aligned}
$$

- **Power Mismatch Formulation [155]**:

$$
\begin{bmatrix}
P_2(v) - P_2\\
\vdots\\
P_N(v) - P_N\\
---------\\
Q_{N_G+1}(v) - Q_{N_G+1}\\
\vdots\\
Q_N(v) - Q_N
\end{bmatrix} =
$$

$$\begin{bmatrix} \sum_{j=1}^{N} |V_2||V_j|\big(G_{2j}\cos(\theta_2-\theta_j)+B_{2j}\sin(\theta_2-\theta_j)\big)-P_2 \\ \vdots \\ \sum_{j=1}^{N} |V_N||V_j|\big(G_{Nj}\cos(\theta_N-\theta_j)+B_{Nj}\sin(\theta_N-\theta_j)\big)-P_N \\ -------------------------------- \\ \sum_{j=1}^{N} |V_{N_G}+1||V_j|\big(G_{N_g+1,j}\sin(\theta_{N_G+1}-\theta_j)+B_{N_g+1,j}\sin(\theta_{N_G+1}-\theta_j)\big)-Q_{N_G+1} \\ \vdots \\ \sum_{j=1}^{N} |V_N||V_j|\big(G_{Nj}\sin(\theta_N-\theta_j)+B_{Nj}\sin(\theta_N-\theta_j)\big)-Q_N \end{bmatrix}$$

Appendix D

IEEE 33 Grid Parameters

Line Data					Load Data		
Line No.	From Bus	To Bus	$R(\Omega)$	$X(\Omega)$	Bus No.	P (kW)	Q (kVAR)
1	0	1	0	0	1	0	0
2	1	2	0.0922	0.0470	2	100	60
3	2	3	0.4930	0.2511	3	90	40
4	3	4	0.3660	0.1864	4	120	80
5	4	5	0.3811	0.1941	5	60	30
6	5	6	0.8190	0.7070	6	60	20
7	6	7	0.1872	0.6188	7	200	100
8	7	8	0.7114	0.2351	8	200	100
9	8	9	1.0300	0.7400	9	60	20
10	9	10	1.0440	0.7400	10	60	20
11	10	11	0.1966	0.0650	11	45	30
12	11	12	0.3744	0.1238	12	60	35
13	12	13	1.4680	1.1550	13	60	35
14	13	14	0.5416	0.7129	14	120	80
15	14	15	0.5910	0.5260	15	60	10
16	15	16	0.7463	0.5450	16	60	20
17	16	17	1.2890	1.7210	17	60	20
18	17	18	0.7320	0.5740	18	90	40
19	2	19	0.1640	0.1565	19	90	40
20	19	20	1.5042	1.3554	20	90	40
21	20	21	0.4095	0.4784	21	90	40
22	21	22	0.7089	0.9373	22	90	40
23	3	23	0.4512	0.3083	23	90	50
24	23	24	0.8980	0.7091	24	420	200
25	24	25	0.8960	0.7011	25	420	200
26	6	26	0.2030	0.1034	26	60	25
27	26	27	0.2842	0.1447	27	60	25
28	27	28	1.0590	0.9337	28	60	20
29	28	29	0.8042	0.7006	29	120	70
30	29	30	0.5075	0.2585	30	200	600
31	30	31	0.9744	0.9630	31	150	70
32	31	32	0.3105	0.3619	32	210	100
33	32	33	0.3410	0.5302	33	60	40

List of Abbreviations

ACS	**a**utomation of **c**omplex power **s**ystems
ADMS	**a**dvanced **d**istribution **m**anagement **s**ystem
AI	**a**rtificial **i**ntelligence
AMI	**a**dvanced **m**etering **i**nfrastructure
ANN	**a**rtificial **n**eural **n**etwork
CI	**c**onfidence **i**nterval
CI	**c**onfiguration **i**dentification
CIM	**c**urrent **i**njection **m**ethod
CL	**c**onfidence **l**evel
CFD/C	**c**urrent-based **f**ast-**d**ecoupled
CNN	**c**onvolutional **n**eural **n**etwork
CPU	**c**entral **p**rocessing **u**nit
DA	**d**istributed **a**utomation
DC	**d**irect-**c**urrent
DDDSSE	**d**ata-**d**riven **d**istribution **s**ystem **s**tate **e**stimation
DERs	**d**istributed **e**nergy **r**esources
DG	**d**istributed **g**eneration
DL	**d**eep **l**earning
DLPF	**d**ecoupled **l**inearized **p**ower **f**low
DMS	**d**istribution **mo**anagement **s**ystem
DSOs	**d**istribution **s**ystem **o**perators
DSSE	**d**istribution **s**ystem **s**tate **e**stimation
ECM	**e**quivalent-**c**urrent-**m**easurements
emf	**e**ectro**mo**tive **f**orce
EMS	**e**nergy **mo**anagement **s**ystem
EVs	**e**lectrical **v**ehicles
FCN	**f**ully **c**onnected **n**etwork
FLOPs	**f**loating-**p**oint **op**erations
FPI	fixed-**p**oint **i**teration
GPS	**g**lobal **p**ositioning **s**ystem
IED	**i**ntelligent **e**lectronic **d**evice
IVS	**i**uput **v**ariable **s**election
KVL	**k**irchhoff **v**oltage **l**aw
MASE	**m**ulti-**a**rea **s**tate **e**stimation
MSE	**m**eans **s**quare **e**rror
NARX	**n**onlinear **a**uto-**r**egressive **e**Xogenous
NLPF	**n**on-**l**inear **p**ower **f**low
PDF	**p**robability **d**ensity **f**unction
PDP	**p**arallel **d**istributed **p**rocessing

PF	**p**ower **f**low
PM	**p**roposed **m**ethod
PMUs	**p**hasor **m**easurement **u**nits
PNN	**p**robabilistic **n**eural **n**etwork
PV	**p**hotov**o**ltaic
QP	**q**uadratic **p**rogramming
RESs	**r**enewable **e**nergy **s**ources
RTU	**r**emote **t**erminal **u**nit
SCADA	**s**upervisory **a**nd **c**ontrol **d**ata **a**cquisition
SD	**s**tandard **d**eviation
SE	**s**tate **e**stimation
SLE	**s**ystem of **l**inear **e**quations
SM	**s**mart **m**eter
SR	**s**uccessive **r**elaxation
TI	**t**opology **i**dentification
TSOs	**t**ransmisson **s**ystem **o**perators
TSSE	**t**ransmission **s**ystem **s**tate **e**stimation
UCNN	**u**nshared **c**onvolutional **n**eural **n**etwork
WLS	**w**eighted **l**east **s**quares

List of Figures

List of Tables

Bibliography

[1] Valérie Masson-Delmotte et al. "Global warming of 1.5 C". In: *An IPCC Special Report on the impacts of global warming of* 1 (2018), pp. 1–9.

[2] D Gielen et al. "Global renewables outlook: Energy transformation 2050". In: *Int. Renew. Energy Agency, Abu Dhabi, United Arab Emirates, Tech. Rep* (2020).

[3] Phil Grünewald. "The grid edge revolution Innovative drivers towards net-zero energy Cooperation". In: *White Paper* (2019).

[4] Per Hallberg et al. "Active distribution system management a key tool for the smooth integration of distributed generation". In: *Eurelectric TF Active System Management* 2.13 (2013).

[5] Henryk Markiewicz and Antoni Klajn. "Voltage disturbances standard en 50160-voltage characteristics in public distribution systems". In: *Wroclaw University of Technology* 21 (2004), pp. 215–224.

[6] IEC-International Electrotechnical Commission et al. "IEC 61000". In: (2015).

[7] Anggoro Primadianto and Chan-Nan Lu. "A review on distribution system state estimation". In: *IEEE Transactions on Power Systems* 32.5 (2016), pp. 3875–3883.

[8] Kaveh Dehghanpour et al. "A survey on state estimation techniques and challenges in smart distribution systems". In: *IEEE Transactions on Smart Grid* 10.2 (2018), pp. 2312–2322.

[9] Ali Abur and Antonio Gomez Exposito. *Power system state estimation: theory and implementation*. CRC press, 2004.

[10] Andrea Bernieri et al. "Neural networks and pseudo-measurements for real-time monitoring of distribution systems". In: *IEEE transactions on instrumentation and measurement* 45.2 (1996), pp. 645–650.

[11] Yan Chen, Maria G Fadda, and Andrea Benigni. "Decentralized state estimation for distribution systems using artificial neural network". In: *2018 IEEE International Instrumentation and Measurement Technology Conference (I2MTC)*. IEEE. 2018, pp. 1–6.

[12] Behzad Zargar et al. "Multiarea Parallel Data-Driven Three-Phase Distribution System State Estimation Using Synchrophasor Measurements". In: *IEEE Transactions on Instrumentation and Measurement* 69.9 (2020), pp. 6186–6202.

[13] Georgia E Asimakopoulou and Nikos D Hatziargyriou. "Evaluation of economic benefits of DER aggregation". In: *IEEE Transactions on Sustainable Energy* 9.2 (2017), pp. 499–510.

[14] Behzad Zargar et al. "Power Quality Improvement in Distribution Grids via Real-Time Smart Exploitation of Electric Vehicles". In: *Energies* 14.12 (2021), p. 3533.

[15] Andrea Angioni et al. "Real-time monitoring of distribution system based on state estimation". In: *IEEE Transactions on Instrumentation and Measurement* 65.10 (2016), pp. 2234–2243.

[16] George N Korres. "A robust method for equality constrained state estimation". In: *IEEE Transactions on Power Systems* 17.2 (2002), pp. 305–314.

[17] Catalina Gomez-Quiles, Antonio de la Villa Jaen, and Antonio Gomez-Exposito. "A factorized approach to WLS state estimation". In: *IEEE Transactions on Power Systems* 26.3 (2011), pp. 1724–1732.

[18] Styliani Sarri et al. "Performance assessment of linear state estimators using synchrophasor measurements". In: *IEEE Transactions on Instrumentation and Measurement* 65.3 (2016), pp. 535–548.

[19] Mohammad Farajollahi, Alireza Shahsavari, and Hamed Mohsenian-Rad. "Linear distribution system state estimation using synchrophasor data and pseudo-measurement". In: *2019 International Conference on Smart Grid Synchronized Measurements and Analytics (SGSMA)*. IEEE. 2019, pp. 1–6.

[20] Shaobu Wang et al. "Assessing Gaussian assumption of PMU measurement error using field data". In: *IEEE Transactions on Power Delivery* 33.6 (2017), pp. 3233–3236.

[21] Junbo Zhao and Lamine Mili. "A framework for robust hybrid state estimation with unknown measurement noise statistics". In: *IEEE Transactions on Industrial Informatics* 14.5 (2017), pp. 1866–1875.

[22] Behzad Zargar et al. "Linear Iterative Power Flow Approach Based on the Current Injection Model of Load and Generator". In: *IEEE Access* 9 (2020), pp. 11543–11562.

[23] Antonio Gómez-Expósito et al. "State estimation in distribution systems". In: *Reference Module in Materials Science and Materials Engineering*. Elsevier, 2022. ISBN: 978-0-12-803581-8. DOI: https://doi.org/10.1016/B978-0-12-821204-2.00014-3. URL: https://www.sciencedirect.com/science/article/pii/B9780128212042000143.

[24] Catalina Gómez-Quiles et al. "Compensated Load Flow Solutions for Distribution System State Estimation". In: *Energies* 13.12 (2020), p. 3100.

[25] Andre L Langner and Ali Abur. "Formulation of three-phase state estimation problem using a virtual reference". In: *IEEE Transactions on Power Systems* 36.1 (2020), pp. 214–223.

[26] Fred C Schweppe and J Wildes. "Power system static-state estimation, Part I: Exact model". In: *IEEE Transactions on Power Apparatus and systems* 1 (1970), pp. 120–125.

[27] I Roytelman and SM Shahidehpour. "State estimation for electric power distribution systems in quasi real-time conditions". In: *IEEE Transactions on Power Delivery* 8.4 (1993), pp. 2009–2015.

[28] Mesut E Baran and Arthur W Kelley. "State estimation for real-time monitoring of distribution systems". In: *IEEE Transactions on Power systems* 9.3 (1994), pp. 1601–1609.

[29] CN Lu, JH Teng, and W-HE Liu. "Distribution system state estimation". In: *IEEE Transactions on Power systems* 10.1 (1995), pp. 229–240.

[30] Mesut E Baran and Arthur W Kelley. "A branch-current-based state estimation method for distribution systems". In: *IEEE transactions on power systems* 10.1 (1995), pp. 483–491.

[31] Ke Li. "State estimation for power distribution system and measurement impacts". In: *IEEE Transactions on Power Systems* 11.2 (1996), pp. 911–916.

[32] Atish K Ghosh et al. "Distribution circuit state estimation using a probabilistic approach". In: *IEEE Transactions on Power Systems* 12.1 (1997), pp. 45–51.

[33] Felix F Wu. "Power system state estimation: a survey". In: *International Journal of Electrical Power & Energy Systems* 12.2 (1990), pp. 80–87.

[34] Urban Kuhar, Gregor Kosec, and Aleš Švigelj. "State Estimation". In: *Observability of Power-Distribution Systems*. Springer, 2020, pp. 11–43.

[35] Alcir Monticelli. *State estimation in electric power systems: a generalized approach*. Springer Science & Business Media, 2012.

[36] Mauro Prais and Anjan Bose. "A topology processor that tracks network modifications". In: *IEEE transactions on Power Systems* 3.3 (1988), pp. 992–998.

[37] Amrita Ghosal and Mauro Conti. "Key management systems for smart grid advanced metering infrastructure: A survey". In: *IEEE Communications Surveys & Tutorials* 21.3 (2019), pp. 2831–2848.

[38] Nan Duan et al. "Smart meters enabling voltage monitoring and control: The last-mile voltage stability issue". In: *IEEE Transactions on Industrial Informatics* 18.1 (2021), pp. 677–687.

[39] Mihai Sănduleac et al. "High reporting rate smart metering data for enhanced grid monitoring and services for energy communities". In: *IEEE Transactions on Industrial Informatics* 18.6 (2021), pp. 4039–4048.

[40] Arun G Phadke and James S Thorp. *Synchronized phasor measurements and their applications*. Vol. 1. Springer, 2008.

[41] Antonello Monti, Carlo Muscas, and Ferdinanda Ponci. *Phasor measurement units and wide area monitoring systems*. Academic Press, 2016.

[42] Alexandra Von Meier et al. "Precision micro-synchrophasors for distribution systems: A summary of applications". In: *IEEE Transactions on Smart Grid* 8.6 (2017), pp. 2926–2936.

[43] Ian Kosen et al. "UPS: Unified PMU-data storage system to enhance T+ D PMU data usability". In: *IEEE Transactions on Smart Grid* 11.1 (2019), pp. 739–748.

[44] Andrea Angioni et al. "A low cost PMU to monitor distribution grids". In: *2017 IEEE International Workshop on Applied Measurements for Power Systems (AMPS)*. IEEE. 2017, pp. 1–6.

[45] Andrea Angioni et al. "Impact of pseudo-measurements from new power profiles on state estimation in low-voltage grids". In: *IEEE Transactions on Instrumentation and Measurement* 65.1 (2015), pp. 70–77.

[46] Whei-Min Lin and Jen-Hao Teng. "State estimation for distribution systems with zero-injection constraints". In: *Proceedings of Power Industry Computer Applications Conference*. IEEE. 1995, pp. 523–529.

[47] Youman Deng, Ying He, and Boming Zhang. "A branch-estimation-based state estimation method for radial distribution systems". In: *IEEE Transactions on power delivery* 17.4 (2002), pp. 1057–1062.

[48] PM De Oliveira-De Jesus and Andrés A Rojas Quintana. "Distribution system state estimation model using a reduced quasi-symmetric impedance matrix". In: *IEEE Transactions on Power Systems* 30.6 (2014), pp. 2856–2866.

[49] Daniel A Haughton and Gerald Thomas Heydt. "A linear state estimation formulation for smart distribution systems". In: *IEEE Transactions on Power Systems* 28.2 (2012), pp. 1187–1195.

[50] Whei-Min Lin, Jen-Hao Teng, and Shi-Jaw Chen. "A highly efficient algorithm in treating current measurements for the branch-current-based distribution state estimation". In: *IEEE Transactions on Power Delivery* 16.3 (2001), pp. 433–439.

[51] Marco Pau, Paolo Attilio Pegoraro, and Sara Sulis. "Efficient branch-current-based distribution system state estimation including synchronized measurements". In: *IEEE Transactions on Instrumentation and Measurement* 62.9 (2013), pp. 2419–2429.

[52] Mesut E Baran, Jaesung Jung, and Thomas E McDermott. "Including voltage measurements in branch current state estimation for distribution systems". In: *2009 IEEE Power & Energy Society General Meeting*. IEEE. 2009, pp. 1–5.

[53] J-H Teng. "Using voltage measurements to improve the results of branch-current-based state estimators for distribution systems". In: *IEE Proceedings-Generation, Transmission and Distribution* 149.6 (2002), pp. 667–672.

[54] Marco Pau, Paolo Attilio Pegoraro, and Sara Sulis. "Performance of three-phase WLS distribution system state estimation approaches". In: *2015 IEEE International Workshop on Applied Measurements for Power Systems (AMPS)*. IEEE. 2015, pp. 138–143.

[55] David Gerbec et al. "Allocation of the load profiles to consumers using probabilistic neural networks". In: *IEEE Transactions on Power Systems* 20.2 (2005), pp. 548–555.

[56] Efthymios Manitsas et al. "Distribution system state estimation using an artificial neural network approach for pseudo measurement modeling". In: *IEEE Transactions on power systems* 27.4 (2012), pp. 1888–1896.

[57] Vladimiro Miranda et al. "Reconstructing missing data in state estimation with autoencoders". In: *IEEE Transactions on power systems* 27.2 (2011), pp. 604–611.

[58] Jianzhong Wu, Yan He, and Nick Jenkins. "A robust state estimator for medium voltage distribution networks". In: *IEEE Transactions on Power Systems* 28.2 (2012), pp. 1008–1016.

[59] Barry P Hayes, Jorn K Gruber, and Milan Prodanovic. "A closed-loop state estimation tool for MV network monitoring and operation". In: *IEEE Transactions on Smart Grid* 6.4 (2014), pp. 2116–2125.

[60] Kaveh Dehghanpour et al. "A game-theoretic data-driven approach for pseudo-measurement generation in distribution system state estimation". In: *IEEE Transactions on Smart Grid* 10.6 (2019), pp. 5942–5951.

[61] Sajjad Khan et al. "Electricity load forecasting for each day of week using deep CNN". In: *Workshops of the International Conference on Advanced Information Networking and Applications*. Springer. 2019, pp. 1107–1119.

[62] Xishuang Dong, Lijun Qian, and Lei Huang. "Short-term load forecasting in smart grid: A combined CNN and K-means clustering approach". In: *2017 IEEE international conference on big data and smart computing (BigComp)*. IEEE. 2017, pp. 119–125.

[63] Maryam Imani and Hassan Ghassemian. "Sequence to image transform based convolutional neural network for load forecasting". In: *2019 27th Iranian Conference on Electrical Engineering (ICEE)*. IEEE. 2019, pp. 1362–1366.

[64] Ni Ding et al. "Neural network-based model design for short-term load forecast in distribution systems". In: *IEEE transactions on power systems* 31.1 (2015), pp. 72–81.

[65] Yi Wang et al. "An ensemble forecasting method for the aggregated load with subprofiles". In: *IEEE Transactions on Smart Grid* 9.4 (2018), pp. 3906–3908.

[66] Zhuoling Li et al. "Deep learning based densely connected network for load forecasting". In: *IEEE Transactions on Power Systems* 36.4 (2020), pp. 2829–2840.

[67] Mohsen Ferdowsi et al. "Measurement Selection for Data-Driven Monitoring of Distribution Systems". In: *IEEE Systems Journal* 13.4 (2019), pp. 4260–4268.

[68] Bernd Brinkmann and Michael Negnevitsky. "A probabilistic approach to observability of distribution networks". In: *IEEE Transactions on power systems* 32.2 (2016), pp. 1169–1178.

[69] H Salehfar and R Zhao. "A neural network preestimation filter for bad-data detection and identification in power system state estimation". In: *Electric power systems research* 34.2 (1995), pp. 127–134.

[70] Yunhui Wu, Amamihe Onwuachumba, and Mohamad Musavi. "Bad data detection and identification using neural network-based reduced model state estimator". In: *2013 IEEE Green Technologies Conference (GreenTech)*. IEEE. 2013, pp. 183–189.

[71] Tabia Ahmad and Nilanian Senroy. "A data driven denoising framework for error corrupted synchrophasor data". In: *2018 20th National Power Systems Conference (NPSC)*. IEEE. 2018, pp. 1–6.

[72] Tabia Ahmad and Nilanjan Senroy. "Statistical characterization of PMU error for robust WAMS based analytics". In: *IEEE Transactions on Power Systems* 35.2 (2019), pp. 920–928.

[73] Yang Weng et al. "Robust data-driven state estimation for smart grid". In: *IEEE Transactions on Smart Grid* 8.4 (2016), pp. 1956–1967.

[74] Ahmed S Zamzam, Xiao Fu, and Nicholas D Sidiropoulos. "Data-driven learning-based optimization for distribution system state estimation". In: *IEEE Transactions on Power Systems* 34.6 (2019), pp. 4796–4805.

[75] Mohsen Ferdowsi et al. "A scalable data-driven monitoring approach for distribution systems". In: *IEEE Transactions on Instrumentation and Measurement* 64.5 (2015), pp. 1292–1305.

[76] Jiawei Zhang et al. "Topology identification and line parameter estimation for non-PMU distribution network: A numerical method". In: *IEEE Transactions on Smart Grid* 11.5 (2020), pp. 4440–4453.

[77] Behrouz Azimian et al. "State and Topology Estimation for Unobservable Distribution Systems Using Deep Neural Networks". In: *IEEE Transactions on Instrumentation and Measurement* 71 (2022), pp. 1–14.

[78] Alireza Akrami, Meysam Doostizadeh, and Farrokh Aminifar. "Optimal reconfiguration of distribution network using μ PMU measurements: a data-driven

stochastic robust optimization". In: *IEEE Transactions on Smart Grid* 11.1 (2019), pp. 420–428.

[79] North American SynchroPhasor Initiative et al. "PMUs and synchrophasor data flows in North America". In: *Smartgrid. Gov* (2014), pp. 1–5.

[80] Daniele Carta, Andrea Benigni, and Carlo Muscas. "Model order reduction for PMU-based state estimation in distribution grids". In: *IEEE Systems Journal* 12.3 (2017), pp. 2711–2720.

[81] Paulo M De Oliveira-De Jesus et al. "PMU-based system state estimation for multigrounded distribution systems". In: *IEEE Transactions on Power Systems* 36.2 (2020), pp. 1071–1081.

[82] Hamed Mohsenian-Rad, Emma Stewart, and Ed Cortez. "Distribution synchrophasors: Pairing big data with analytics to create actionable information". In: *IEEE Power and Energy Magazine* 16.3 (2018), pp. 26–34.

[83] Alireza Akrami, Salman Asif, and Hamed Mohsenian-Rad. "Sparse tracking state estimation for low-observable power distribution systems using D-PMUs". In: *IEEE Transactions on Power Systems* 37.1 (2021), pp. 551–564.

[84] Heloisa H Müller, Carlos A Castro, and Daniel Dotta. "Allocation of PMU channels at substations for topology processing and state estimation". In: *IET Generation, Transmission & Distribution* 14.11 (2020), pp. 2034–2045.

[85] Carlo Muscas et al. "Uncertainty of voltage profile in PMU-based distribution system state estimation". In: *IEEE Transactions on Instrumentation and Measurement* 65.5 (2015), pp. 988–998.

[86] Paolo Attilio Pegoraro et al. "PMU-based distribution system state estimation with adaptive accuracy exploiting local decision metrics and IoT paradigm". In: *IEEE Transactions on Instrumentation and Measurement* 66.4 (2017), pp. 704–714.

[87] Ramtin Khalili and Ali Abur. "PMU-based decoupled state estimation for unsymmetrical power systems". In: *IEEE Transactions on Power Systems* 36.6 (2021), pp. 5359–5368.

[88] MJMMJ Mukaka. "Statistics corner: a guide to appropriate use of correlation in medical research". In: *Malawi Med J* 24.3 (2012), pp. 69–71.

[89] Thomas G. Dietterich. *Adaptive computation and machine learning*. 2016.

[90] F Burden, D Winkler, and DJ Livingstone. *Artificial neural networks: methods and applications*. 2009.

[91] *Why Tanh Generally Performs Better Than Sigmoi*. URL: `https://towardsdatascience.com/why-data-should-be-normalized-before-training-a-neural-network-c626b7f66c7d`. (accessed: 05.2017).

[92] Tomasz Szandała. "Review and comparison of commonly used activation functions for deep neural networks". In: *Bio-inspired neurocomputing*. Springer, 2021, pp. 203–224.

[93] Christopher M Bishop et al. *Neural networks for pattern recognition*. Oxford university press, 1995.

[94] Jie Shao et al. "Is normalization indispensable for training deep neural network?" In: *Advances in Neural Information Processing Systems* 33 (2020), pp. 13434–13444.

[95] Hanen Borchani et al. "A survey on multi-output regression". In: *Wiley Interdisciplinary Reviews: Data Mining and Knowledge Discovery* 5.5 (2015), pp. 216–233.

[96] Sami Repo et al. "The IDE4L project: Defining, designing, and demonstrating the ideal grid for all". In: *IEEE Power and Energy Magazine* 15.3 (2017), pp. 41–51.

[97] CW Hansen and AS Debs. "Power system state estimation using three-phase models". In: *IEEE transactions on power systems* 10.2 (1995), pp. 818–824.

[98] *IEEE PES AMPS DSAS Test Feeder Working Group*. URL: `https://site.ieee.org/pes-testfeeders/resources/`. (accessed: 05.2017).

[99] Kristin H Jarman. *Beyond basic statistics: Tips, tricks, and techniques every data analyst should know*. John Wiley & Sons, 2015.

[100] Marco Pau et al. "Distributed State Estimation for Multi-Feeder Distribution Grids". In: *IEEE Open Journal of Instrumentation and Measurement* 1 (2022), pp. 1–12.

[101] Marta Vanin et al. "A framework for constrained static state estimation in unbalanced distribution networks". In: *2022 17th International Conference on Probabilistic Methods Applied to Power Systems (PMAPS)*. IEEE. 2022, pp. 1–11.

[102] Yang Weng, Rohit Negi, and Marija D Ilić. "Probabilistic joint state estimation for operational planning". In: *IEEE Transactions on Smart Grid* 10.1 (2017), pp. 601–612.

[103] Jiawei Zhang, Peng Wang, and Ning Zhang. "Distribution network admittance matrix estimation with linear regression". In: *IEEE Transactions on Power Systems* 36.5 (2021), pp. 4896–4899.

[104] Ying Zhang and Jianhui Wang. "Towards highly efficient state estimation with nonlinear measurements in distribution systems". In: *IEEE Transactions on Power Systems* 35.3 (2020), pp. 2471–2474.

[105] Marco Pau et al. "An efficient and accurate solution for distribution system state estimation with multiarea architecture". In: *IEEE Transactions on Instrumentation and Measurement* 66.5 (2017), pp. 910–919.

[106] Fan Zhang and Carol S Cheng. "A modified Newton method for radial distribution system power flow analysis". In: *IEEE Transactions on Power Systems* 12.1 (1997), pp. 389–397.

[107] David A Patterson and John L Hennessy. *Computer Organization and Design MIPS Edition: The*. 2013.

[108] Alan Clements. "Computer Organization and Architecture: Themes and Variations, 2014". In: *Cengage Learning, Stamford, CT, Excerpts* ().

[109] Raphael Hunger. *Floating Point Operations in Matrix-Vector Calculus*. URL: `https://mediatum.ub.tum.de/doc/625604/625604`.

[110] Ryan Tibshirani. *Flops for basic operations*. URL: `https://www.stat.cmu.edu/~ryantibs/convexopt-S15/scribes/09-num-lin-alg-scribed.pdf`.

[111] NH Beebe. "Accurate hyperbolic tangent computation". In: *Dept. Math., Center Sci. Comput., Univ. Utah, Salt Lake City, UT, USA* (1991).

[112] Alycen Wiacek, Eduardo González, and Muyinatu A Lediju Bell. "CohereNet: A deep learning architecture for ultrasound spatial correlation estimation and coherence-based beamforming". In: *IEEE transactions on ultrasonics, ferroelectrics, and frequency control* 67.12 (2020), pp. 2574–2583.

[113] Antonio Gomez-Exposito et al. "A multilevel state estimation paradigm for smart grids". In: *Proceedings of the IEEE* 99.6 (2011), pp. 952–976.

[114] Leonard L Grigsby. *Power system stability and control*. CRC press, 2007.

[115] Th Van Cutsem, Jean-Luc Horward, and M Ribbens-Pavella. "A two-level static state estimator for electric power systems". In: *IEEE transactions on power apparatus and systems* 8 (1981), pp. 3722–3732.

[116] Djalma M Falcao, Felix F Wu, and Liam Murphy. "Parallel and distributed state estimation". In: *IEEE Transactions on Power Systems* 10.2 (1995), pp. 724–730.

[117] Liang Zhao and Ali Abur. "Multi area state estimation using synchronized phasor measurements". In: *IEEE Transactions on Power Systems* 20.2 (2005), pp. 611–617.

[118] Antonio J Conejo, Sebastin de la Torre, and Miguel Canas. "An optimization approach to multiarea state estimation". In: *IEEE Transactions on Power Systems* 22.1 (2007), pp. 213–221.

[119] Carlo Muscas et al. "Multiarea distribution system state estimation". In: *IEEE Transactions on Instrumentation and Measurement* 64.5 (2015), pp. 1140–1148.

[120] Leticia De Alvaro Garcia and Sébastien Grenard. "Scalable distribution state estimation approach for distribution management systems". In: *2011 2nd IEEE PES International Conference and Exhibition on Innovative Smart Grid Technologies*. IEEE. 2011, pp. 1–6.

[121] Nazia Nusrat, Malcolm Irving, and Gareth Taylor. "Development of distributed state estimation methods to enable smart distribution management systems". In: *2011 IEEE International Symposium on Industrial Electronics*. IEEE. 2011, pp. 1691–1696.

[122] Carlo Muscas et al. "Two-step procedures for wide-area distribution system state estimation". In: *2014 IEEE International Instrumentation and Measurement Technology Conference (I2MTC) Proceedings*. IEEE. 2014, pp. 1517–1522.

[123] Ahmed H Abdelaziz et al. "Uncertainty propagation through deep neural networks". In: *Interspeech 2015*. 2015.

[124] Ian Goodfellow, Yoshua Bengio, and Aaron Courville. *Deep Learning*. `http://www.deeplearningbook.org`. MIT Press, 2016.

[125] José Luis Picard et al. "Electric Distribution System Planning Methodology Considering Distributed Energy Resources: A Contribution towards Real Smart Grid Deployment". In: *Energies* 14.7 (2021), p. 1924.

[126] Antonio Cataliotti et al. "An innovative measurement approach for load flow analysis in MV smart grids". In: *IEEE Transactions on Smart Grid* 7.2 (2015), pp. 889–896.

[127] Antonio Cataliotti et al. "An improved load flow method for MV networks based on LV load measurements and estimations". In: *IEEE Transactions on Instrumentation and Measurement* 68.2 (2018), pp. 430–438.

[128] Giovanni Artale et al. "Real-Time Power Flow Monitoring and Control System for Microgrids Integration in Islanded Scenarios". In: *IEEE Transactions on Industry Applications* 55.6 (2019), pp. 7186–7197.

[129] William F Tinney and Clifford E Hart. "Power flow solution by Newton's method". In: *IEEE Transactions on Power Apparatus and systems* 11 (1967), pp. 1449–1460.

[130] Dariush Shirmohammadi et al. "A compensation-based power flow method for weakly meshed distribution and transmission networks". In: *IEEE Transactions on power systems* 3.2 (1988), pp. 753–762.

[131] Yuntao Ju et al. "An extension of FBS three-phase power flow for handling PV nodes in active distribution networks". In: *IEEE Transactions on Smart Grid* 5.4 (2014), pp. 1547–1555.

[132] Paulo AN Garcia et al. "Improvements in the representation of PV buses on three-phase distribution power flow". In: *IEEE Transactions on Power Delivery* 19.2 (2004), pp. 894–896.

[133] Florian Dörfler and Francesco Bullo. "Novel insights into lossless AC and DC power flow". In: *2013 IEEE Power & Energy Society General Meeting*. IEEE. 2013, pp. 1–5.

[134] Yuxiao Liu et al. "Data-driven power flow linearization: A regression approach". In: *IEEE Transactions on Smart Grid* 10.3 (2018), pp. 2569–2580.

[135] Yi Tan et al. "Linearizing power flow model: A hybrid physical model-driven and data-driven approach". In: *IEEE Transactions on Power Systems* 35.3 (2020), pp. 2475–2478.

[136] Luis Böttcher et al. “Solving AC power flow with graph neural networks under realistic constraints”. In: *arXiv preprint arXiv:2204.07000* (2022).

[137] Brian Stott, Jorge Jardim, and Ongun Alsaç. “DC power flow revisited”. In: *IEEE Transactions on Power Systems* 24.3 (2009), pp. 1290–1300.

[138] Alejandro Garces. “A linear three-phase load flow for power distribution systems”. In: *IEEE Transactions on Power Systems* 31.1 (2015), pp. 827–828.

[139] Hamed Ahmadi, José R Martı, and Alexandra von Meier. “A linear power flow formulation for three-phase distribution systems”. In: *IEEE Transactions on Power Systems* 31.6 (2016), pp. 5012–5021.

[140] Seyed Masoud Fatemi et al. “Introducing a novel DC power flow method with reactive power considerations”. In: *IEEE Transactions on Power Systems* 30.6 (2014), pp. 3012–3023.

[141] Jingwei Yang et al. “A state-independent linear power flow model with accurate estimation of voltage magnitude”. In: *IEEE Transactions on Power Systems* 32.5 (2016), pp. 3607–3617.

[142] Saverio Bolognani and Florian Dörfler. “Fast power system analysis via implicit linearization of the power flow manifold”. In: *2015 53rd Annual Allerton Conference on Communication, Control, and Computing (Allerton)*. IEEE. 2015, pp. 402–409.

[143] Saverio Bolognani and Sandro Zampieri. “On the existence and linear approximation of the power flow solution in power distribution networks”. In: *IEEE Transactions on Power Systems* 31.1 (2015), pp. 163–172.

[144] Haoyu Yuan et al. “Novel linearized power flow and linearized OPF models for active distribution networks with application in distribution LMP”. In: *IEEE Transactions on Smart Grid* 9.1 (2016), pp. 438–448.

[145] José R Martí, Hamed Ahmadi, and Lincol Bashualdo. “Linear power-flow formulation based on a voltage-dependent load model”. In: *IEEE Transactions on Power Delivery* 28.3 (2013), pp. 1682–1690.

[146] Daniel K Molzahn, Ian A Hiskens, et al. “A survey of relaxations and approximations of the power flow equations”. In: *Foundations and Trends® in Electric Energy Systems* 4.1-2 (2019), pp. 1–221.

[147] Guillaume Denis et al. “The Migrate project: the challenges of operating a transmission grid with only inverter-based generation. A grid-forming control improvement with transient current-limiting control”. In: *IET Renewable Power Generation* 12.5 (2018), pp. 523–529.

[148] Yuntao Ju et al. “General three-phase linear power flow for active distribution networks with good adaptability under a polar coordinate system”. In: *IEEE Access* 6 (2018), pp. 34043–34050.

[149] Hongwei Li et al. "A three-phase unbalanced linear power flow solution with PV bus and ZIP load". In: *IEEE Access* 7 (2019), pp. 138879–138889.

[150] Ilhan Kocar et al. "Multiphase load-flow solution for large-scale distribution systems using MANA". In: *IEEE Transactions on Power Delivery* 29.2 (2013), pp. 908–915.

[151] Jan Machowski et al. *Power system dynamics: stability and control*. John Wiley & Sons, 2020.

[152] CK Koc and Guanrong Chen. "Authors' reply [Computational complexity of matrix inversion]". In: *IEEE Transactions on Aerospace and Electronic Systems* 30.4 (1994), p. 1115.

[153] WH Press et al. "Numerical Recipes in C: The Art of Scientific Computing, 87–93 Cambridge University Press". In: *New York, NY* (1992).

[154] Uri M Ascher. *Numerical methods for evolutionary differential equations*. SIAM, 2008.

[155] Arthur R Bergen. *Power systems analysis*. Pearson Education India, 2009.

[156] Roger C Dugan and D Montenegro. "Reference guide: The open distribution system simulator". In: *EPRI* (2013).

[157] Luiz FK Possani and Rafael de P Soares. "Numerical and computational aspects of cosmo-based activity coefficient models". In: *Brazilian Journal of Chemical Engineering* 36 (2019), pp. 587–598.

[158] "User Manual: DIgSILENT PowerFactory". In: *DIgSILENT GmbH* (2018).

[159] Bayernwerk AG. URL: `https://www.bayernwerk.de/de.html`.

Curriculum Vitae

2017–2023	Research Assistant and Doctoral Candidate Institute for Automation of Complex Power Systems (ACS) RWTH Aachen University, Germany
22.11.2023	Doctoral Examination for Dr.-Ing.
2012–2015	Studies of Electrical Engineering, Information Technology and Computer Engineering RWTH Aachen University, Germany
July 2015	Master of Science
2004–2009	Studies of Electrical Power Engineering Islamic Azad University-Najafabad Branch, Iran
July 2009	Bachelor of Science
22.05.1986	born in Esfahan, Iran

E.ON ERC Band 1
Streblow, R.
Thermal Sensation and Comfort Model for Inhomogeneous Indoor Environments
1. Auflage 2011
ISBN 978-3-942789-00-4

E.ON ERC Band 2
Naderi, A.
Multi-phase, multi-species reactive transport modeling as a tool for system analysis in geological carbon dioxide storage
1. Auflage 2011
ISBN 978-3-942789-01-1

E.ON ERC Band 3
Westner, G.
Four Essays related to Energy Economic Aspects of Combined Heat and Power Generation
1. Auflage 2012
ISBN 978-3-942789-02-8

E.ON ERC Band 4
Lohwasser, R.
Impact of Carbon Capture and Storage (CCS) on the European Electricity Market
1. Auflage 2012
ISBN 978-3-942789-03-5

E.ON ERC Band 5
Dick, C.
Multi-Resonant Converters as Photovoltaic Module-Integrated Maximum Power Point Tracker
1. Auflage 2012
ISBN 978-3-942789-04-2

E.ON ERC Band 6
Lenke, R.
A Contribution to the Design of Isolated DC-DC Converters for Utility Applications
1. Auflage 2012
ISBN 978-3-942789-05-9

E.ON ERC Band 7
Brännström, F.
Einsatz hybrider RANS-LES-Turbulenzmodelle in der Fahrzeugklimatisierung
1. Auflage 2012
ISBN 978-3-942789-06-6

E.ON ERC Band 8
Bragard, M.
The Integrated Emitter Turn-Off Thyristor - An Innovative MOS-Gated High-Power Device
1. Auflage 2012
ISBN 978-3-942789-07-3

E.ON ERC Band 9
Hoh, A.
Exergiebasierte Bewertung gebäudetechnischer Anlagen
1. Auflage 2013
ISBN 978-3-942789-08-0

E.ON ERC Band 10
Köllensperger, P.
The Internally Commutated Thyristor - Concept, Design and Application
1. Auflage 2013
ISBN 978-3-942789-09-7

E.ON ERC Band 11
Achtnicht, M.
Essays on Consumer Choices Relevant to Climate Change: Stated Preference Evidence from Germany
1. Auflage 2013
ISBN 978-3-942789-10-3

E.ON ERC Band 12
Panašková, J.
Olfaktorische Bewertung von Emissionen aus Bauprodukten
1. Auflage 2013
ISBN 978-3-942789-11-0

E.ON ERC Band 13
Vogt, C.
Optimization of Geothermal Energy Reservoir Modeling using Advanced Numerical Tools for Stochastic Parameter Estimation and Quantifying Uncertainties
1. Auflage 2013
ISBN 978-3-942789-12-7

E.ON ERC Band 14
Benigni, A.
Latency exploitation for parallelization of power systems simulation
1. Auflage 2013
ISBN 978-3-942789-13-4

E.ON ERC Band 15
Butschen, T.
Dual-ICT – A Clever Way to Unite Conduction and Switching Optimized Properties in a Single Wafer
1. Auflage 2013
ISBN 978-3-942789-14-1

E.ON ERC Band 16
Li, W.
Fault Detection and Protection inMedium Voltage DC Shipboard Power Systems
1. Auflage 2013
ISBN 978-3-942789-15-8

E.ON ERC Band 17
Shen, J.
Modeling Methodologies for Analysis and Synthesis of Controls and Modulation Schemes for High-Power Converters with Low Pulse Ratios
1. Auflage 2014
ISBN 978-3-942789-16-5

E.ON ERC Band 18
Flieger, B.
Innenraummodellierung einer Fahrzeugkabine in der Programmiersprache Modelica
1. Auflage 2014
ISBN 978-3-942789-17-2

E.ON ERC Band 19
Liu, J.
Measurement System and Technique for Future Active Distribution Grids
1. Auflage 2014
ISBN 978-3-942789-18-9

E.ON ERC Band 20
Kandzia, C.
Experimentelle Untersuchung der Strömungsstrukturen in einer Mischlüftung
1. Auflage 2014
ISBN 978-3-942789-19-6

E.ON ERC Band 21
Thomas, S.
A Medium-Voltage Multi-Level DC/DC Converter with High Voltage Transformation Ratio
1. Auflage 2014
ISBN 978-3-942789-20-2

E.ON ERC Band 22
Tang, J.
Probabilistic Analysis and Stability Assessment for Power Systems with Integration of Wind Generation and Synchrophasor Measurement
1. Auflage 2014
ISBN 978-3-942789-21-9

E.ON ERC Band 23
Sorda, G.
The Diffusion of Selected Renewable Energy Technologies: Modeling, Economic Impacts, and Policy Implications
1. Auflage 2014
ISBN 978-3-942789-22-6

E.ON ERC Band 24
Rosen, C.
Design considerations and functional analysis of local reserve energy markets for distributed generation
1. Auflage 2014
ISBN 978-3-942789-23-3

E.ON ERC Band 25
Ni, F.
Applications of Arbitrary Polynomial Chaos in Electrical Systems
1. Auflage 2015
ISBN 978-3-942789-24-0

E.ON ERC Band 26
Michelsen, C. C.
The *Energiewende* in the German Residential Sector: Empirical Essays on Homeowners' Choices of Space Heating Technologies
1. Auflage 2015
ISBN 978-3-942789-25-7

E.ON ERC Band 27
Rohlfs, W.
Decision-Making under Multi-Dimensional Price Uncertainty for Long-Lived Energy Investments
1. Auflage 2015
ISBN 978-3-942789-26-4

E.ON ERC Band 28
Wang, J.
Design of Novel Control algorithms of Power Converters for Distributed Generation
1. Auflage 2015
ISBN 978-3-942789-27-1

E.ON ERC Band 29
Helmedag, A.
System-Level Multi-Physics Power Hardware in the Loop Testing for Wind Energy Converters
1. Auflage 2015
ISBN 978-3-942789-28-8

E.ON ERC Band 30
Togawa, K.
Stochastics-based Methods Enabling Testing of Grid-related Algorithms through Simulation
1. Auflage 2015
ISBN 978-3-942789-29-5

E.ON ERC Band 31
Huchtemann, K.
Supply Temperature Control Concepts in Heat Pump Heating Systems
1. Auflage 2015
ISBN 978-3-942789-30-1

E.ON ERC Band 32
Molitor, C.
Residential City Districts as Flexibility Resource: Analysis, Simulation, and Decentralized Coordination Algorithms
1. Auflage 2015
ISBN 978-3-942789-31-8

E.ON ERC Band 33
Sunak, Y.
Spatial Perspectives on the Economics of Renewable Energy Technologies
1. Auflage 2015
ISBN 978-3-942789-32-5

E.ON ERC Band 34
Cupelli, M.
Advanced Control Methods for Robust Stability of MVDC Systems
1. Auflage 2015
ISBN 978-3-942789-33-2

E.ON ERC Band 35
Chen, K.
Active Thermal Management for Residential Air Source Heat Pump Systems
1. Auflage 2015
ISBN 978-3-942789-34-9

E.ON ERC Band 36
Pâques, G.
Development of SiC GTO Thyristors with Etched Junction Termination
1. Auflage 2016
ISBN 978-3-942789-35-6

E.ON ERC Band 37
Garnier, E.
Distributed Energy Resources and Virtual Power Plants: Economics of Investment and Operation
1. Auflage 2016
ISBN 978-3-942789-37-0

E.ON ERC Band 38
Calì, D.
Occupants' Behavior and its Impact upon the Energy Performance of Buildings
1. Auflage 2016
ISBN 978-3-942789-36-3

E.ON ERC Band 39
Isermann, T.
A Multi-Agent-based Component Control and Energy Management System for Electric Vehicles
1. Auflage 2016
ISBN 978-3-942789-38-7

E.ON ERC Band 40
Wu, X.
New Approaches to Dynamic Equivalent of Active Distribution Network for Transient Analysis
1. Auflage 2016
ISBN 978-3-942789-39-4

E.ON ERC Band 41
Garbuzova-Schiftler, M.
The Growing ESCO Market for Energy Efficiency in Russia: A Business and Risk Analysis
1. Auflage 2016
ISBN 978-3-942789-40-0

E.ON ERC Band 42
Huber, M.
Agentenbasierte Gebäudeautomation für raumlufttechnische Anlagen
1. Auflage 2016
ISBN 978-3-942789-41-7

E.ON ERC Band 43
Soltau, N.
High-Power Medium-Voltage DC-DC Converters: Design, Control and Demonstration
1. Auflage 2017
ISBN 978-3-942789-42-4

E.ON ERC Band 44
Stieneker, M.
Analysis of Medium-Voltage Direct-Current Collector Grids in Offshore Wind Parks
1. Auflage 2017
ISBN 978-3-942789-43-1

E.ON ERC Band 45
Bader, A.
Entwicklung eines Verfahrens zur Strompreisvorhersage im kurzfristigen Intraday-Handelszeitraum
1. Auflage 2017
ISBN 978-3-942789-44-8

E.ON ERC Band 46
Chen, T.
Upscaling Permeability for Fractured Porous Rocks and Modeling Anisotropic Flow and Heat Transport
1. Auflage 2017
ISBN 978-3-942789-45-5

E.ON ERC Band 47
Ferdowsi, M.
Data-Driven Approaches for Monitoring of Distribution Grids
1. Auflage 2017
ISBN 978-3-942789-46-2

E.ON ERC Band 48
Kopmann, N.
Betriebsverhalten freier Heizflächen unter zeitlich variablen Randbedingungen
1. Auflage 2017
ISBN 978-3-942789-47-9

E.ON ERC Band 49
Fütterer, J.
Tuning of PID Controllers within Building Energy Systems
1. Auflage 2017
ISBN 978-3-942789-48-6

E.ON ERC Band 50
Adler, F.
A Digital Hardware Platform for Distributed Real-Time Simulation of Power Electronic Systems
1. Auflage 2017
ISBN 978-3-942789-49-3

E.ON ERC Band 51
Harb, H.
Predictive Demand Side Management Strategies for Residential Building Energy Systems
1. Auflage 2017
ISBN 978-3-942789-50-9

E.ON ERC Band 52
Jahangiri, P.
Applications of Paraffin-Water Dispersions in Energy Distribution Systems
1. Auflage 2017
ISBN 978-3-942789-51-6

E.ON ERC Band 53
Adolph, M.
Identification of Characteristic User Behavior with a Simple User Interface in the Context of Space Heating
1. Auflage 2018
ISBN 978-3-942789-52-3

E.ON ERC Band 54
Galassi, V.
Experimental evidence of private energy consumer and prosumer preferences in the sustainable energy transition
1. Auflage 2017
ISBN 978-3-942789-53-0

E.ON ERC Band 55
Sangi, R.
Development of Exergy-based Control Strategies for Building Energy Systems
1. Auflage 2018
ISBN 978-3-942789-54-7

E.ON ERC Band 56
Stinner, S.
Quantifying and Aggregating the Flexibility of Building Energy Systems
1. Auflage 2018
ISBN 978-3-942789-55-4

E.ON ERC Band 57
Fuchs, M.
Graph Framework for Automated Urban Energy System Modeling
1. Auflage 2018
ISBN 978-3-942789-56-1

E.ON ERC Band 58
Osterhage, T.
Messdatengestützte Analyse und Interpretation sanierungsbedingter Effizienzsteigerungen im Wohnungsbau
1. Auflage 2018
ISBN 978-3-942789-57-8

E.ON ERC Band 59
Frieling, J.
Quantifying the Role of Energy in Aggregate Production Functions for Industrialized Countries
1. Auflage 2018
ISBN 978-3-942789-58-5

E.ON ERC Band 60
Lauster, M.
Parametrierbare Gebäudemodelle für dynamische Energiebedarfsrechnungen von Stadtquartieren
1. Auflage 2018
ISBN 978-3-942789-59-2

E.ON ERC Band 61
Zhu, L.
Modeling, Control and Hardware in the Loop in Medium Voltage DC Shipboard Power Systems
1. Auflage 2018
ISBN 978-3-942789-60-8

E.ON ERC Band 62
Feron, B.
An optimality assessment methodology for Home Energy Management System approaches based on uncertainty analysis
1. Auflage 2018
ISBN 978-3-942789-61-5

E.ON ERC Band 63
Diekerhof, M.
Distributed Optimization for the Exploitation of Multi-Energy Flexibility under Uncertainty in City Districts
1. Auflage 2018
ISBN 978-3-942789-62-2

E.ON ERC Band 64
Wolisz, H.
Transient Thermal Comfort Constraints for Model Predictive Heating Control
1. Auflage 2018
ISBN 978-3-942789-63-9

E.ON ERC Band 65
Pickartz, S.
Virtualization as an Enabler for Dynamic Resource Allocation in HPC
1. Auflage 2019
ISBN 978-3-942789-64-6

E.ON ERC Band 66
Khayyamim, S.
Centralized-decentralized Energy Management in Railway System
1. Auflage 2019
ISBN 978-3-942789-65-3

E.ON ERC Band 67
Schlösser, T.
Methodology for Holistic Evaluation of Building Energy Systems under Dynamic Boundary Conditions
1. Auflage 2019
ISBN 978-3-942789-66-0

E.ON ERC Band 68
Cui, S.
Modular Multilevel DC-DC Converters Interconnecting High-Voltage and Medium-Voltage DC Grids
1. Auflage 2019
ISBN 978-3-942789-67-7

E.ON ERC Band 69
Hu, J.
Modulation and Dynamic Control of Intelligent Dual-Active-Bridge Converter Based Substations for Flexible DC Grids
1. Auflage 2019
ISBN 978-3-942789-68-4

E.ON ERC Band 70
Schiefelbein, J.
Optimized Placement of Thermo-Electric Energy Systems in City Districts under Uncertainty
1. Auflage 2019
ISBN 978-3-942789-69-1

E.ON ERC Band 71
Ferdinand, R.
Grid Operation of HVDC-Connected Offshore Wind Farms: Power Quality and Switching Strategies
1. Auflage 2019
ISBN 978-3-942789-70-7

E.ON ERC Band 72
Musa, A.
Advanced Control Strategies for Stability Enhancement of Future Hybrid AC/DC Networks
1. Auflage 2019
ISBN 978-3-942789-71-4

E.ON ERC Band 73
Angioni, A.
Uncertainty modeling for analysis and design of monitoring systems for dynamic electrical distribution grids
1. Auflage 2019
ISBN 978-3-942789-72-1

E.ON ERC Band 74
Möhlenkamp, M.
Thermischer Komfort bei Quellluftströmungen
1. Auflage 2019
ISBN 978-3-942789-73-8

E.ON ERC Band 75
Voss, J.
Multi-Megawatt Three-Phase Dual-Active Bridge DC-DC Converter
1. Auflage 2019
ISBN 978-3-942789-74-5

E.ON ERC Band 76
Siddique, H.
The Three-Phase Dual-Active Bridge Converter Family: Modeling, Analysis, Optimization and Comparison of Two-Level and Three-Level Converter Variants
1. Auflage 2019
ISBN 978-3-942789-75-2

E.ON ERC Band 77
Heesen, F.
An Interdisciplinary Analysis of Heat Energy Consumption in Energy-Efficient Homes: Essays on Economic, Technical and Behavioral Aspects
1. Auflage 2019
ISBN 978-3-942789-76-9

E.ON ERC Band 78
Möller, R.
Untersuchung der Durchschlagspannung von Mineral-, Silikonölen und synthetischen Estern bei mittelfrequenten Spannungen
1. Auflage 2020
ISBN 978-3-942789-77-6

E.ON ERC Band 79
Höfer, T.
Transition Towards a Renewable Energy Infrastructure: Spatial Interdependencies and Stakeholder Preferences
1. Auflage 2020
ISBN 978-3-942789-78-3

E.ON ERC Band 80
Freitag, H.
Investigation of the Internal Flow Behavior in Active Chilled Beams
1. Auflage 2020
ISBN 978-3-942789-79-0

E.ON ERC Band 81
Razik, L.
High-Performance Computing Methods in Large-Scale Power System Simulation
1. Auflage 2020
ISBN 978-3-942789-80-6

E.ON ERC Band 82
Mirz, M.
A Dynamic Phasor Real-Time Simulation Based Digital Twin for Power Systems
1. Auflage 2020
ISBN 978-3-942789-81-3

E.ON ERC Band 83
Schmitz, H.
Energy Consumption Behavior of Private Households: Heterogeneity, Prosuming, and Rebound
1. Auflage 2020
ISBN 978-3-942789-82-0

E.ON ERC Band 84
Cupelli, L.
Data-driven Methods for Voltage Control in Distribution Networks: A Bottom-Up Approach
1. Auflage 2020
ISBN 978-3-942789-83-7

E.ON ERC Band 85
Happ, S.
A Scalable Simulation Method for Cyber-Physical Power Systems
1. Auflage 2020
ISBN 978-3-942789-84-4

E.ON ERC Band 86
Rewitz, K.
Modellierung des thermischen Komforts in Kabinen-innenräumen
1. Auflage 2021
ISBN 978-3-948234-00-3

E.ON ERC Band 87
Wesseling, M.
Probabilistische Bewertung von Entrauchungsanlagen
1. Auflage 2021
ISBN 978-3-948234-01-0

E.ON ERC Band 88
Stoyanova, I.
Cooperative Energy Management and Cross-Domain Optimization for Electro-Thermal Devices at City-District and City-Level
1. Auflage 2021
ISBN 978-3-948234-02-7

E.ON ERC Band 89
Tran, T.
Advanced hierarchical control structure for Virtual Oscillator-based distributed generation in multi-bus microgrids under different grid dynamics and disturbances
1. Auflage 2021
ISBN 978-3-948234-03-4

E.ON ERC Band 90
Yang, Z.
On the Stability of Three-Phase Grid-Tied Photovoltaic Inverter Systems
1. Auflage 2021
ISBN 978-3-948234-04-1

E.ON ERC Band 91
Wang, T.
Fault Detection and Isolation in DC Distribution Grids
1. Auflage 2021
ISBN 978-3-948234-05-8

E.ON ERC Band 92
Beushausen, S.
A GaN-Based Switched-Mode Gate-Drive Unit for Medium-Voltage IGBTs
1. Auflage 2021
ISBN 978-3-948234-06-5

E.ON ERC Band 93
Schumacher, M.
Design and Assessment of Grid-driven Distributed Cogeneration
1. Auflage 2021
ISBN 978-3-948234-07-2

E.ON ERC Band 94
Joebges, P.
Distributed Real-Time Simulation of Modular Bidirectional DC-DC Converters for Control-Hardware-in-the-Loop
1. Auflage 2021
ISBN 978-3-948234-08-9

E.ON ERC Band 95
Averous, R.
Analysis of the Application of a Grid Emulator to Conduct Grid Compliance Tests for Multi-Megawatt Wind Turbines A Contribution towards Ground Testing of Wind Turbines
1. Auflage 2021
ISBN 978-3-948234-09-6

E.ON ERC Band 96
Virdag, A.
Design, Implementation and Analysis of DC Circuit-breaker for Low-Voltage DC Grids with Counter-current Injection Principle
1. Auflage 2021
ISBN 978-3-948234-10-2

E.ON ERC Band 97
Dähling, S.
Cloud-based Multi-Agent Systems for Flexibility Management in Future Distribution Grids
1. Auflage 2021
ISBN 978-3-948234-11-9

E.ON ERC Band 98
Qawasmi, A.
Fault Current Interruption Analysis and Development of a Power Semiconductor Switch for a Medium-Voltage DC Hybrid Circuit Breaker
1. Auflage 2021
ISBN 978-3-948234-12-6

E.ON ERC Band 99
Nolting, L.
Die Versorgungssicherheit mit Elektrizität im Kontext von Liberalisierung und Energiewende
1. Auflage 2021
ISBN 978-3-948234-13-3

E.ON ERC Band 100
Mathis, P.
Heat Transfer Enhancement in Natural Convective Channel Flows by Vortex Streets
1. Auflage 2022
ISBN 978-3-948234-14-0

E.ON ERC Band 101
Wolff, S.
Stated Preferences Concerning Private Passenger and Light-Duty Electric Vehicles in Germany
1. Auflage 2022
ISBN 978-3-948234-15-7

E.ON ERC Band 102
Hackbarth, A.
Private Households' Preferences for Alternative Fuel Vehicles in Germany – An Empirically Founded Analysis of Adoption Decisions, Willingness-to-Pay, and Policy Scenarios
1. Auflage 2022
ISBN 978-3-948234-16-4

E.ON ERC Band 103
Ge, L.
Performance Enhancement of Switched Reluctance Machines for High-speed Backup Generators: Design, Measurement and Control
1. Auflage 2022
ISBN 978-3-948234-17-1

E.ON ERC Band 104
Atasoy, T.
Strategic and Behavioral Responses of Consumers and Producers to Energy and Environmental Policies
1. Auflage 2022
ISBN 978-3-948234-18-8

E.ON ERC Band 105
Remmen, P.
Automated Calibration of Non-Residential Urban Building Energy Modeling
1. Auflage 2022
ISBN 978-3-948234-19-5

E.ON ERC Band 106
Schild, T.
Systematische Entwicklung strukturierter Steuerungs-algorithmen für die Gebäude- und Anlagentechnik
1. Auflage 2022
ISBN 978-3-948234-20-1

E.ON ERC Band 107
Sidik, Y.
Modeling, Control, and Dynamic Stability Analysis of Two-Stage DC Collector Grids in Offshore Wind Park Clusters
1. Auflage 2022
ISBN 978-3-948234-21-8

E.ON ERC Band 108
Sadu, A.
Towards resilient design of distribution grid automation system: An evaluation of its reliability against random failures and susceptibility to targeted attacks
1. Auflage 2022
ISBN 978-3-948234-22-5

E.ON ERC Band 109
Hinz, A.
Electrical Propulsion Systems for Civil Transportation Aircraft
1. Auflage 2022
ISBN 978-3-948234-23-2

E.ON ERC Band 110
Mehrfeld, P.
Evaluation of Heat Pump Systems Under Dynamic Operating Conditions
1. Auflage 2022
ISBN 978-3-948234-24-9

E.ON ERC Band 111
Teichrib, J.
A Hybrid Semiconductor Device for Medium-Voltage DC-DC Converters - The Combination of Thyris-tor and Transistor Technologies
1. Auflage 2022
ISBN 978-3-948234-25-6

E.ON ERC Band 112
Frehn, A.
Under voltage ride through tests on nacelle test benches equipped with a power hardware in the loop setup
1. Auflage 2023
ISBN 978-3-948234-26-3

E.ON ERC Band 113
Bode, G.
Generation of Training Data for Fault Detection and Diagnosis Algorithms Using Fault Simulation and Parameter Uncertainty
1. Auflage 2023
ISBN 978-3-948234-27-0

E.ON ERC Band 114
Vering, C.
Optimale Auslegung von Wärmepumpensystemen für Bestandsgebäude
1. Auflage 2023
ISBN 978-3-948234-28-7

E.ON ERC Band 115
Bogdanović, M.
Towards model partitioning automation of distributed real-time power systems simulations of distribution networks
1. Auflage 2023
ISBN 978-3-948234-29-4

E.ON ERC Band 116
Hering, D.
Optimization of district heating networks using mixed integer quadratically constrained programs
1. Auflage 2023
ISBN 978-3-948234-30-0

E.ON ERC Band 117
De Din, E.
Multi-Timescale Framework for the Voltage Control of Active Distribution Grids
1. Auflage 2023
ISBN 978-3-948234-31-7

E.ON ERC Band 118
Specht, J.
The Energy Supplier 2.0 – Activating Private Households' Flexibility Potential for Value Creation and Services Supply
1. Auflage 2023
ISBN 978-3-948234-32-4

E.ON ERC Band 119
Teichmann, J.
Auswirkungen der Hydraulik auf das Betriebsverhalten von raumlufttechnischen Anlagen
1. Auflage 2023
ISBN 978-3-948234-33-1

E.ON ERC Band 120
Haghgoo, M.
Semantic Interoperability as a Service for the Smart Energy System
1. Auflage 2023
ISBN 978-3-948234-34-8

E.ON ERC Band 121
Roy, G.
Automation Architectures for hybrid ac-dc grid
1. Auflage 2023
ISBN 978-3-948234-35-5

E.ON ERC Band 122
Mork, M.
Model Predictive Control of
Building Energy Systems
1. Auflage 2023
ISBN 978-3-948234-36-2

This dissertation introduces an innovative data-driven monitoring approach designed for distribution systems, playing a crucial role in facilitating the integration of eco-friendly energy sources. Focused on grids that incorporate renewable sources and end consumers, the study proposes a distribution system state estimation method utilizing artificial neural networks (ANNs) and synchrophasor measurements.

Noteworthy contributions include the application of ANNs for mapping synchrophasor measurements to system states and the development of three-phase ANN-based estimators for unbalanced grids.

Computational efficiency is demonstrated through quantitative comparisons with model-based methods, highlighting the superiority of the proposed data-driven technique. The research also distributes the computational burden, employing parallel and multi-area architectures to enhance speed during the training phase and accuracy during the estimation phase.

An iterative linear power flow (PF) method is proposed to generate training data for ANN-based estimators. This method integrates linear current injection models for both P-Q and P-V nodes. For cases with only P-Q nodes, the PF is solved in a single shot, while for those involving P-V nodes, it is iteratively solved. The convergence rate of the solver is controlled by utilizing a relaxation factor.

ISBN 978-3-948234-37-9

Thinking the Future
Zukunft denken